

NASA Contractor Report 3655

257079

Experimental Study of the Separating Confluent Boundary-Layer

Volume I - Summary

J. A. Braden, R. R. Whipkey,
G. S. Jones, and D. E. Lilley

CONTRACT NAS1-16028
JUNE 1983



25th Anniversary
1958-1983

NASA

NASA Contractor Report 3655

Experimental Study of the Separating Confluent Boundary-Layer

Volume I - Summary

J. A. Braden, R. R. Whipkey,
G. S. Jones, and D. E. Lilley
Lockheed-Georgia Company
A Division of Lockheed Corporation
Marietta, Georgia

Prepared for
Langley Research Center
under Contract NAS1-16028



National Aeronautics
and Space Administration

**Scientific and Technical
Information Branch**

1983

FOREWORD

This document is submitted in accordance with the requirements of NASA Contract NASI-16028, "Experimental Studies of the Separating Confluent Boundary-Layer." H. L. Morgan is the NASA-Langley Contract Monitor and J. A. Braden is the Lockheed-Georgia Project Manager.

The technical descriptions and results from this experimental study are presented in two volumes; The present document, Volume I, summarizes the test program and provides limited test results and comparative analysis. The bulk of the data, comprised of laser-velocimeter measurements and airfoil surface pressures, is contained in Volume II (NASA CR-166018) in tabulated and plotted formats.

SUMMARY

An experimental program is described which employs a 2-D laser-velocimeter as basic test instrumentation to study the development and separation characteristics of the confluent boundary-layer on a 2-D airfoil. The airfoil used is a NASA GAW-1 (General Aviation) section equipped with a 29 percent chord single-slotted trailing-edge flap and a 15 percent chord leading-edge slat. Inclusive of the single-element airfoil configuration, twenty-five different combinations of slat and/or flap deflections and angles-of-attack are represented in the study matrix. Laser-velocimeter (LV) measurements have been acquired on the airfoil upper- and lower-surfaces to allow evaluation of initial conditions and subsequent behavior of the confluent boundary-layer as it approaches and undergoes separation. The quantities measured by the laser-velocimeter system include velocity profiles, turbulence intensities and Reynolds shear stresses. These quantities are presented in both tabulated and graphical-display formats in the companion data report and its supplements, Volume II (NASA CR-166018). In Volume I, a complete description of the test program is presented and comparisons are drawn with results from more conventional test instrumentation such as pitot-static probes and single-element hot-wires. Skin friction and other boundary-layer parameters, derived from the LV-measurements, are shown to compare favorably with data from Preston-tubes and theoretical calculations from the NASA Multiple-Airfoil Program. Conclusions drawn from this extensive experimental study indicate that the laser-velocimeter, when used on a production basis, provides a reliable means of rapidly providing high-

quality data for on-going theoretical modeling efforts.

TABLE OF CONTENTS

	Page
FORWORD	iii
SUMMARY	v
FIGURE INDEX	ix
1.0 INTRODUCTION	1
2.0 LIST OF SYMBOLS	6
3.0 EXPERIMENTAL PROGRAM	9
3.1 APPRAOCH SUMMARY	9
3.2 TEST MODEL	10
3.3 TEST INSTRUMENTATION	11
3.3.1 LV-System	11
3.3.2 Surface-Pressures	12
3.3.3 Conventional Instrumentation	13
3.4 TEST FACILITY	16
3.4.1 Model Installation	16
3.4.2 Two-Dimensional Characteristics	17
3.4.3 Wall-Effect Considerations	20
3.5 TEST CONDITIONS	21
3.6 TEST CONFIGURATIONS.	23
3.6.1 Matrix Selection	23
3.6.2 LV-Data Axes	26
3.7 DATA REDUCTION	27
3.7.1 Conventional Instrumentation.	27
3.7.2 LV-Data Reduction	28
3.8 DATA ACCURACY	30

3.8.1	Conventional Instrumentation	30
3.8.2	LV-Error Analysis	31
4.0	RESULTS AND DISCUSSION	34
4.1	PRESSURE TESTS	34
4.1.1	COMPARATIVE RESULTS	34
4.1.2	LV-MATRIX PRESSURE DATA	37
4.2	LV-PROFILES	38
4.3	CONVENTIONAL INSTRUMENTATION COMPARISONS	40
4.3.1	Velocity Profiles	41
4.3.2	Turbulence Profiles	42
4.3.3	Skin Friction Measurements	49
4.4	COMPARATIVE BOUNDARY-LAYER AND WAKE PARAMETERS . . .	52
4.4.1	Comparison of Theoretical Boundary- Layer Parameters	52
4.4.2	Law-of-the-Wake Comparisons	53
4.4.3	Velocity Distributions in the Wake	55
5.0	CONCLUSIONS	57
6.0	REFERENCES	62

LIST OF FIGURES

	<u>Page</u>
1. Regions Exhibiting Confluent Boundary-Layer Flow on a High-Lift Airfoil	70
2. Approach to Confluent Boundary-Layer Experimental Study . .	71
3. Geometric Arrangement of a GAW-1 High-Lift Airfoil for the Separating Confluent Boundary-Layer Test Program . . .	72
4. GAW-1 Leading-Edge Slat Design	73
5. Experimental Set-Up for GAW-1 Airfoil in ERF Wind Tunnel. .	74
6(a) Details of Traversing Pitot-Static and Hot-Wire Probes . .	78
6(b) Pitot-Static and Single-Element Hot Wire Probe Installation	79
7. GAW-1 Model Installation in 10x30-Inch ERF Wind Tunnel . .	80
8. Definition of Geometric Parameters on GAW-1 High-Lift Airfoil	81
9. ERF Flow Two-Dimensionality Without Sidewall Blowing. . . .	82
10. Sidewall Blowing Scheme for GAW-1 Confluent Boundary-Layer Study	83
11. Application of Rapid-Traversal LV-Analog System for Flow Two-Dimensionality Evaluation	84
12(a) Oil-Flow Photograph of Single-Element Airfoil Upper-Surface with Free Transition, $\alpha = 6^\circ$	85
12(b) Oil-Flow Photograph of Single-Element Airfoil Lower-Surface with Free Transition, $\alpha = 6^\circ$	86
13. Spatial Orientation of "Off-Surface" Surveys for Wakes and Freestream Entry Flows	88
14. Block Diagram of Pitot-Static and Hot-Wire Data Reduction Systems	89
15. Block Diagram of Laser Velocimeter Data Reduction System. .	90
16. Comparisons of GAW-1 Airfoil Performance	91
17. Variation of Maximum Lift Coefficient With Reynolds Number, GAW-1 Single-Element Airfoil ($M_o \approx 0.15$).	92
18. Comparison of GAW-1 Airfoil Surface Pressure Distributions, $\delta_f = 0^\circ$, $\alpha \approx 0^\circ$	93

LIST OF FIGURES

	<u>Page</u>
19. Comparison of GAW-1 Airfoil Surface Pressure Distributions, $\delta_f = 0^\circ$, $\alpha \approx 6^\circ$	94
20. Comparison of GAW-1 Airfoil Surface Pressure Distributions, $\delta_f = 0^\circ$, $\alpha \approx 15^\circ$	95
21. Comparison of GAW-1 Airfoil Surface Pressure Distributions, $\delta_f = 30^\circ$, $\alpha \approx 4^\circ$	96
22. Comparison of GAW-1 Airfoil Surface Pressure Distributions, $\delta_f = 30^\circ$, $\alpha \approx 10^\circ$	97
23. Comparison of GAW-1 Airfoil Surface Pressure Distributions, $\delta_f = 40^\circ$, $\alpha \approx 0^\circ$	98
24. Comparison of GAW-1 Airfoil Surface Pressure Distributions, $\delta_f = 40^\circ$, $\alpha \approx 5^\circ$	99
25. Variation of Lift Coefficient with Angle-of-Attack, Configuration A	100
26. Variation of Lift Coefficient with Angle of Attack, Configuration B	101
27. Variation of Lift Coefficient with Angle-of-Attack, Configuration C	102
28. Variation of Lift Coefficient with Angle-of-Attack, Configurations D, E, F	103
29. GAW-1 Airfoil Configuration for LV-Surveys - Pressure Distribution, Configuration A-4	104
30. GAW-1 Airfoil Configuration for LV-Surveys - Pressure Distribution, Configuration B-3	105
31. GAW-1 Airfoil Configuration for LV-Surveys - Pressure Distribution, Configuration C-2	106
32. GAW-1 Airfoil Configuration for LV-Surveys - Pressure Distribution, Configuration D-2	107
33. GAW-1 Airfoil Configuration for LV-Surveys - Pressure Distribution, Configuration E-3	108
34. GAW-1 Airfoil Configuration for LV-Surveys - Pressure Distribution, Configuration F-2	109
35. Velocity Profile Composite Plot, $\alpha = 16^\circ$; Configuration A-5	110
36. Velocity Profile Composite Plot, $\alpha = 12^\circ$; Configuration B-3	111

LIST OF FIGURES

	<u>Page</u>
37. Velocity Profile Composite Plot, $\alpha = 10^\circ$; Configuration C-3	112
38. Velocity Profile Composite Plot, $\alpha = 24^\circ$; Configuration D-3	113
39. Velocity Profile Composite Plot, $\alpha = 16^\circ$; Configuration E-3	114
40. Velocity Profile Composite Plot, $\alpha = 14^\circ$; Configuration F-3	115
41(a) Shear Stress Composite Plot, $\alpha = 16^\circ$; Configuration E-3	116
41(b) Streamwise Turbulence Component, u' , $\alpha = 16^\circ$; Configuration E-3	117
41(c) Normal Turbulence Component, v' , $\alpha = 16^\circ$; Configuration E-3	118
42. Typical Plot Format for Individual Profiles	120
43(a) Enlargement of Leading-Edge Slat Flow-Field, $\alpha = 16^\circ$	121
43(b) Enlargement of Trailing-Edge Slot Flow-Field, $\alpha = 16^\circ$	122
43(c) Enlargement of Leading-Edge Slat Flow Field Exhibiting Unstable Flow, $\alpha = 24^\circ$	123
44(a) Composite Plot of Streamwise Velocity Component, U/U_o , $\alpha = 6^\circ$	124
44(b) Composite Plot of Normal Velocity Component, V/U_o , $\alpha = 6^\circ$	125
45(a) Comparison of LV-, Single-Element Hot-Wire and Pressure-Probe Velocity Profiles, $\alpha = 4^\circ$, $X/C = 0.60$, Main Element	126
45(b) Comparison of LV-, Single-Element Hot-Wire and Pressure-Probe Velocity Profiles; $\alpha = 4^\circ$, $X/C = 0.90$, Main-Element	127
46(a) Comparison of LV- and Hot-Wire Mean and Turbulence Profiles In Boundary-Layer, $X/C = 0.70$, Main	128
46(b) Comparison of LV- and Hot-Wire Mean and Turbulence Profiles In Boundary-Layer, $X/C = 0.80$, Main	129
46(c) Comparison of LV and Hot-Wire Mean and Turbulence Profiles In Wake, $X/C = 1.10$, Wake	130
46(d) Histogram Comparison of LV- and Hot-Wire Measurement Techniques for Large Mean Velocity With Isotropic Turbulence	131

LIST OF FIGURES

	<u>Page</u>
46(e) Effect of LV- u' and v' on Simulated Hot-Wire Signal, GAW-1, $X/C = 0.60$	132
46(f) Uniform Grid Test Arrangement In ERF Wind-Tunnel	133
46(g) Effect of Spatial Resolution On Hot-Wire Measurements; Uniform Grid Test	134
46(h) Log Linear Plot of RMS Spectra For Two Different Length Hot-Wires @ $X/M = 14$ Behind Grid	135
46(i) Effect of Spatial Resolution Corrections on GAW-1 Airfoil Turbulence Data	136
47. Comparison of LV-Derived Skin-Friction Value with Preston-Tube Measurement	137
48. Skin-Friction Evaluations on Configuration B-1, Upper-Surfaces	138
49. Skin-Friction Measurement on Configuration C-1, Upper-Surfaces	139
50. Skin-Friction Evaluations on Configuration F-3, Upper-Surfaces	140
51(a) Comparison of LV-Derived Ordinary Boundary-Layer Parameters with Calculated; Upper-Surface, Configuration B-4	141
51(b) Comparison of LV-Derived Ordinary Boundary-Layer Parameters with Calculated; Upper-Surface, Configuration C-4	142
51(c) Comparison of Boundary-Layer Parameters Within the Main- Element Confluent Region of Configuration F-1	143
52(a) Comparison of "Law-of-the-Wake" Calculations with LV-Measured Velocity Profiles, GAW-1 Airfoil	144
52(b) Comparison of "Law-of-the-Wake" Calculations with LV-Measured Velocity Profiles, GAW-1 Airfoil	145
53. Comparison of Typical Wake Profile to Velocity Distribution Computation	146
54(a) Velocity Distribution in the Wake, Configurations C-4 and C-5	147
54(b) Velocity Distribution in the Wake, Configurations C-4 and C-5	148

LIST OF TABLES

	Page
I.(a) GAW-1 Airfoil Coordinates	67
I.(b) 29% C Fowler Flap Configuration	68
II. 15 Percent Chord Leading-Edge Slat Coordinates	69
III. GAW-1 Chordwise Surface-Pressure Port Locations - Main-Element and Flap Surfaces	76
IV. GAW-1 Chordwise Surface-Pressure Port Locations - Slat Surfaces	77
V. Configuration Matrix Selected for Detailed LV-Flow- Surveys	87
VI. Typical LV-Data Tabulation	119

1.0 INTRODUCTION

Airfoil sections, in either single- or multi-element form, currently present little significant design problems in subsonic, attached flow-fields although in the latter, confluent boundary-layer calculations are still a problem. Theoretical progress on airfoil design and analysis techniques is nominally at the point where the prediction of flow-separation onset and the interactive influence of the separated surfaces and wakes are of major concern. While notable progress is being made on predictive techniques for single airfoils experiencing flow separation, similar progress is not in evidence for the multi-element configuration approaching and undergoing stall. A basic deterrent in the latter case has been the lack of a suitable data base around which the theoretical models of trailing-edge flap boundary-layers and wakes undergoing separation can be developed and validated. The development of a suitable data base is the subject matter addressed by the present report emphasizing the high-lift airfoil. However, in consideration of the status and data needs of related theoretical methods under current study, such data as described herein has general application to the turbulence modeling and code validation efforts associated with the more advanced theoretical techniques for airfoil performance predictions.

For the single-element case, two theoretical approaches are currently being pursued to extend analysis procedures into the complex flow regimes which exhibit a significant degree of separation. One approach is based on solving the potential equations with viscous

corrections supplied by a solution of the inverse integral boundary-layer equations; that is, the boundary-layer equations are solved with displacement thickness given and with the pressure gradient to be determined. These approaches are being actively pursued by a number of investigators. An overall review of the methodologies is presented in Reference 1, with additional detail provided in References 2-7. A second approach presently demonstrating promising results involves the development of an analytical model of the separated flow zone up to and beyond stall for the single airfoil; an iterative procedure is used to define the shape and limits of the separated region. References 8 through 10 provide details of the method along with typical experimental comparisons. As a result of these on-going efforts, it is clear that reliable solutions are now available for a wide range of single-element configurations at various Mach numbers and for both laminar and turbulent boundary-layers.

Another approach to airfoil theoreticl development emphasizes the single-element case but is not restricted to such. This is the solution of the full Navier-Stokes equations with some turbulence model assumption used for closure of the equations. Attempts to solve these rather formidable equations have received widespread documentation in the literature and it is only recently that the results have become encouraging. Some of the most promising work appears to be that of Tassa with excellent results having been demonstrated for single-element airfoils in attached flows (Reference 11) and for static and dynamic stall conditions (References 12 and 13).

Corresponding theoretical advances for multi-element airfoils (i.e., flapped and slatted high-lift configurations) are being made despite the extreme complexity of the flow interactions associated with the confluent boundary-layer (boundary-layer which arises on downstream elements as a result of more forward-located slots in leading- or trailing-edge devices). Work on a comprehensive analytical model of the confluent boundary layer has been dominated by the earlier analytical and experimental work of Goradia (Reference 14) whereby integral techniques were used to define the make-up and development of this flow-field. In its present form, this model is subject to known limitations. Major restrictions are the absence of confluent boundary layer separation criteria and the exclusion of forward-element flow-separation in setting up initial conditions for the downstream development of the boundary-layer and wake. For this methodology to be pursued further, a basic requirement is the acquisition of an adequate data base with which such restrictions can be removed.

In view of the complex nature of the confluent boundary-layer flow, it may be that a solution of Navier-Stokes is ultimately dictated. However, the solution is complicated by the need to construct computational grids (the pacing item for this development) that are compatible with the multi-element surface and meet stringent requirements for smoothness and grid clustering. Promising grid approaches have been published by Thomas (Reference 15) and an application of his approach to the multi-element airfoil is underway. An acceptable grid-generation method should be available in the near future and with such, solutions could be available for the multi-element case. Eval-

uation of the solutions will then be required to prove-out the calculation methods and, in particular, the flow-turbulence models. High quality, experimental data will also be a necessity for making such evaluations.

Until the higher-order theories noted in the foregoing become more mature, the integral techniques will provide a meaningful approach to confluent boundary-layer analysis. Therefore, a common need for stimulating progress on the integral method, as well as for establishing the background for validating the advanced methods, is a reliable experimental data base. Necessary parameters in such an experimental program should include the definition of the boundary-layer in terms of velocity profile, Reynolds shear stress and flow-turbulence. The acquisition of such data on the high-lift airfoil, in particular, would require careful flow measurements within highly restrictive areas such as small slots and flap-cove-regions to define boundary-layer initial conditions ahead of the slot exit. The difficulty of doing this with conventional, intrusive instrumentation is well known and has recently been circumvented by the substantial advances made in laser-velocimeter (LV) development. The potential value of the LV-system for becoming the accepted standard of general wind-tunnel measurements has been brought into prominence by the very rapid progress made at Lockheed-Georgia (References 16 through 19), NASA (References 20 and 21) and elsewhere on advanced instrumentation techniques.

With the foregoing technical background, Lockheed-Georgia has

undertaken a contractual effort, sponsored by the NASA (Langley), to extend and further develop an experimental data base for the separating confluent boundary-layer. The primary test-instrumentation is a two-dimensional laser-velocimeter system utilized in this instance on a production basis. The low-speed experimental work is structured around the NASA (General Aviation) GAW-1 airfoil, which is a well-behaved turbulent airfoil, tested in a variety of single and multi-element configurations. Surface-pressures and corresponding LV-boundary-layer profiles in terms of velocities (u,v) , turbulence intensities (u',v') and Reynolds shear stresses $(\frac{\bar{u}'\bar{v}'}{U_e^2})$ are presented. Comparisons are given between LV-derived flow parameters and those obtained from more conventional instruments such as pitot-static probes, Preston tubes, and hot-wire anemometry.

Volume I summarizes the scope of the experimental effort and provides sample cases exemplifying the basic measurements and comparative studies. The bulk of the test results is in Volume II which contains pressure and LV data in both tabulated and plotted forms.

2.0 LIST OF SYMBOLS

C_l	section lift coefficient, $L/q C$
$C_{l_{max}}$	maximum section lift coefficient
C_p	pressure coefficient, P/q
C	chord length, in.
C_f	skin friction coefficient,
C_{l_α}	section lift-curve slope
h, H	height, inches
L	section lift, pounds
g/c or G	gap-to-chord ratio
OH/C	overhang-to-chord ratio
P	pressure, psf or psi
q_∞ or q_e	freestream dynamic pressure, psf
M_∞	freestream Mach number

R_N	Reynolds number based on airfoil basic chord length
t/c	airfoil thickness-to-chord ratio
U or U_e	freestream velocity, fps
U_{max}	velocity at edge of boundary-layer, fps
u, v	cartesian velocity components, fps
u', v'	turbulent velocity components, fps
\bar{u}, \bar{v}	mean velocity components, fps
x, y, z	cartesian coordinates, inches
α	angle-of-attack, degrees
ρ	mass density, slugs/cu. ft.
θ	boundary-layer momentum thickness, inches
δ	boundary-layer height, inches
δ^*	boundary-layer displacement thickness, inches

δ_f	flap deflection, degrees
δ_s	slat deflection, degrees
τ	shearing stress at wall, psf
ν	kinematic viscosity, ft^2/sec

Subscripts

max	maximum
min	minimum
∞, e	freestream condition
U, L	upper- or lower-surface, respectively
S	with reference to slat
M	with reference to main-element
F	with reference to flap
W	with reference to Wake
R	resultant, normally with respect to vector summation of velocity components

3.0 EXPERIMENTAL PROGRAM

3.1 Approach Summary

The primary objective in this high-lift experimental study, in contrast to the usual slot (or gap) geometry optimization process, has been to generate typical initial conditions on surfaces upstream of the slot which would introduce characteristic development and eventual breakdown of the confluent boundary-layer on downstream surfaces. Figure 1 shows typical confluent regions of interest for a three-element airfoil such as the GAW-1 under study. As preliminary to the actual boundary-layer survey work, a number of preparatory steps were needed to assure an orderly progression in accomplishing this overall task. Figure 2 shows the sequencing of these steps where the selection of the configuration matrix for the detailed LV-surveys and the development of the LV-data processing software were essential elements. These steps, along with the necessary test-facility modifications and model development, will be discussed in detail in the following paragraphs.

As noted on figure 2, the NASA-Lockheed Multiple-Airfoil Program (MAP) was employed during the study as the basis for theoretical comparisons of airfoil performance or boundary-layer behavior, for providing general test guidelines and for the appropriate airfoil geometric properties necessary to set up the LV-traversing programs. The original MAP-program, providing both inviscid and viscous airfoil computations, is described in Reference 14; certain modifications and

extensions by NASA are contained in the current version of this basic program.

3.2 Test-Model

The experimental flow surveys were conducted on a 17-percent thick NASA GAW-1 (General Aviation) airfoil which could represent a 9-inch chord single-element configuration as well as a flapped and/or slatted section (figure 3). The 10-inch spans of main-element and the 29-percent chord Fowler-type flap were both constructed of aluminum while the slat was of steel to maintain rigidity in the tunnel installation. Tables I(a) and (b) provide ordinates for the main-element and flap. For practical fabrication purposes, the long, thin cusp of the main-element cove region was cut off at the 94 percent chord position in lieu of the 98 percent (design) station. This left a small step (0.020 inches) on the top-surface at $x/c = 0.94$ when the flap was nested. In its nested position, the flap leading-edge also produces a slight discontinuity in the main-element under-surface (see Table I(b)).

As a general aviation airfoil, the GAW-1 would not normally employ a slat. For purposes of the present study, an "add-on", 15 percent chord leading-edge device was provided in order to generate a confluent boundary-layer on the main-element upper-surface. As indicated in figure 4, the nose and upper-surface shapes of the slat were the same as that of the basic airfoil with the slat under-surface contour generated using elliptical geometry. Thus, the slat did not

represent a deployable device inasmuch as the basic airfoil leading-edge remained in its original (no slat) form. Table II provides the ordinates for the slat design.

3.3 Test Instrumentation

3.3.1 Laser-Velocimeter System

The LV system was developed at Gelac (Reference 16) and utilizes a 4-watt Argon laser normally operating at 1.5 to 2.0 watts on all color lines. The system is typically operated in the backscatter mode at a focal length of 30 inches. A 6-inch receiving lens provides an optical aperture of f5 and is positioned off-axis 10-15 degrees in combinations of left, right, up or down. The geometry of the model dictates which combination position is required to allow measurements close to the surface without blocking the receiving optics. The velocity components are measured at the orthogonal intersection of the dual green (488 nm) and dual blue (514.5 nm) beams. The measuring volume at this intersection is approximately 0.005 inch in diameter.

The laser and optics packages are mounted on a mutually orthogonal 3-axes positioner allowing ± 12 inches of travel in each axis and a positioning resolution of 0.001 inches. The positioner is computer-controlled to provide automatic LV-surveys of the flow field at any relative surface angle and any selected increments of traverse.

Smoke particles are used for the seeding medium and are injected

into the tunnel downstream of the test section. This arrangement uses the complete wind tunnel circuit as an impactor to remove the larger seeding particles and provide a more monodispersed particle size at the measurement point near the model. Figure 5 provides a photograph of the laser plus controlling equipment as employed in the present experimental study in the Lockheed Experimental Research Facility (ERF) wind tunnel.

An innovation to the basic LV digital-system was extensively employed to minimize acquisition and data processing times during the tests. This device is the analog real-time velocity system which allows on-line velocities to be monitored and instantly plotted while rapidly scanning areas around the model. This capability has been obtained by the incorporation of a real-time analogy division module within the basic LV-system. The modification provides a D.C. analog of velocity which is used with an x-y recorder to plot velocity versus position for "quick-look" flow-field surveys. As specific points of interest are identified, the more time-consuming digital measurements of turbulence intensity and Reynolds shear stresses may then be acquired in the normal manner. For the present study, this system was employed not only in the course of developing pertinent boundary-layer information but it was also found to be extremely useful in "trimming" the wall-blowing augmentation system as well as for assuring flow two-dimensionality through spanwise flow surveys.

3.3.2 Surface-Pressures

A single-row of surface-pressure taps was installed on the centerline of each of the three airfoil elements. Tables III and IV show the chordwise positions of the 0.049 inch pressure leads on the main airfoil-element and flap, (Table III), and the slat (Table IV).

3.3.3 Conventional Instrumentation

Conventional instrumentation studies were undertaken as an accessory to the primary experimental program to provide comparative boundary-layer or wake data to that acquired by the LV. The alternate instruments selected for these studies were:

- o Pitot-static probes
- o Preston tubes
- o Single-element hot-wire

Another type of instrument considered was a "glue-on" skin-friction gage. However, excessive sensitivity to temperature effects produced unreliable calibration charts and the use of this device was subsequently deleted from the program. In the conventional instrumentation comparisons, the traversing pitot-static probe provided comparative velocity profiles, the Preston tubes gave skin-friction measurements and the hot-wire probe provided velocity profiles (unseparated flow) and turbulence data. While the LV-system does not produce surface-friction measurements directly such can be deduced from

close-to-surface LV-measurements of velocity profiles via the "Clauser-plot" approach wherein the measured profile can be superposed and matched with lines of constant skin friction coefficient when plotted in the form U/U_{\max} vs $\frac{yU_e}{\nu}$ (Reference 22). In acquiring the comparative data, measurements by the alternate instrumentation were confined to regions characterized by low pressure gradients as well as relatively unrestricted areas of the model, such as the upper-surface of the main-element or wake, to avoid the need for more high specialized instrumentation. It should also be noted that the alternate instrumentation studies were generally performed independently of the LV-measurements with some exceptions to be noted. In such comparative studies, a more desirable approach would have been to acquire the conventional instrument measurements simultaneously with the corresponding LV-results to circumvent possible differences in tunnel operating conditions or model configuration. The approach taken in the primary study, however, saved considerable testing-time and served to demonstrate the consistency in which model, test-facility and instrumentation could be repeatedly combined to evaluate discrete points in the flow-field.

The pressure probe assembly consisted of a 0.020-inch diameter total-head tube flattened to 0.010-inch and a separate 0.032-inch diameter static tube as portrayed in figure 6. The static port was displaced laterally by 0.50 inches from the total-head tube. Both probes were malleable and could be adjusted to lay flat on the model surface in which case, the total-head tube provided essentially the same information as a Preston tube. Initial comparisons of the

static-probe surface measurements to those determined by the surface-pressure taps showed insignificant differences indicating that the probe could be used for skin-friction derivations.

The basic hot-wire probe utilized a single-element 5-micron wire mounted in a universal holder, figure 6(a). The wire was unplated which left an active length of 0.150 inches corresponding to a length/diameter ratio of 12000. Constant temperature operation was used at an overheat ratio of 1:1.8. Frequency response of the hot-wire was 0 to 20 KHz.

As will be discussed in some detail in Section 4.3, a supplementary test was performed in the interest of developing added insight into basic differences existing between hot-wire and LV-turbulence measurements. This study, conducted under a closely-controlled test environment, included variations in the physical dimensions of the basic hot-wire described here. Additional detail on the alternate hot-wires will be given in the referenced section.

The probe positioner (see figure 5) consisted of a stepper-motor controlled traverse mechanism which was automated by a mini-computer. The positioner has a resolution of 0.0001 inches and was mounted to the tunnel in such a manner as to permit the selection of the traversing angle relative to the model surface or wake. The total-head pressure tube was also used as a fouling contact against the model surface to provide a reference point for accurately defining

the relative probe position. Occasional problems arose with this system in that the probe would "float" slightly above the airfoil surface and introduce a small but definable error in the probe position information.

3.4 Test Facility

The tests were conducted in the Lockheed-Georgia Experimental Research Facility (ERF) which is fully-instrumented for and dedicated to LV-oriented projects (see figure 5). The ERF is a closed-return, low-speed wind tunnel powered by a 40 horsepower vari-drive unit attached to a centrifugal blower. For two-dimensional airfoil studies, the test section size is 10-inch wide by 30-inch high (56-inch long) with a maximum speed of about 180 fps. The turbulence level as determined by a hot-wire is about 0.1 percent. An optical glass sidewall provides LV-viewing access to the entire model periphery as well as the test-section entry and model wake. Speed control is maintained by monitoring a set of calibrated Piezzio-rings installed upstream of the test section. Fully-automated, conventional support equipment provides on-line tabulated and plotted pressure data.

3.4.1 Model Installation

For wind-tunnel installation, figure 7 shows the three-elements of the airfoil cantilevered from a sidewall turntable opposite the optical viewing window of the laser-velocimeter. An in-contour

pivot-pin, attached at the glass sidewall, mated with the airfoil 50 percent chord point and gave added support to the installation. For accurate positioning of the flap, as well as for providing additional support without LV-interference, a single flap bracket was installed one-inch off of the centerline toward the sidewall turntable. This bracket contained a matrix of pinned positioning holes for rapidly locating the flap to a pre-selected range of gap sizes, over-hang positions and flap angles, figure 8. Similarly for additional slat support, a thin steel bracket was installed at the slat-optical glass juncture (figure 7). This support could be varied in position if excessive interference with LV-viewing was incurred. At the span extremities, rubber seals were employed between the model and wall (or glass) to prevent end-flow into the juncture regions.

Repeated tests with and without the bracketry installed showed little influence of this hardware on model centerline pressure data. Additionally, LV-flow-surveys indicated that local boundary-layer velocity profiles were not significantly affected by the flap bracket as long as the surveys were made at about 20 percent of span away from the bracket position. The leading-edge slat support member at the wall juncture was also found to have little influence on airfoil data due to the presence of the blowing augmentation injected at the sidewalls.

3.4.2 Two-Dimensional Characteristics

Tunnel check-outs and calibration surveys confirmed the essential

two-dimensional character of the flow within the ERF for normal testing of airfoils spanning the 10-inch test-section. By "normal", it is meant that conventional testing is routinely carried out up to and including airfoil stall ($C_{l_{max}}$). In the lower angle-of-attack or pre-separation stage, the major concern is with the model/wall juncture where a rapid boundary-layer build-up is possible. This could promote premature flow separation and possibly influence airfoil stall performance. As is well known, this effect can be suppressed by wall-blowing or suction at a rate tailored to the particular span-loading which is to be preserved up to near-wall positions. At airfoil stall and beyond, where massive flow separation is present, the surface-flow within the separated zone tends to become three-dimensional in character, gravitating toward the span extremities where it leaves the wall/airfoil trailing-edge system as a vortex pair. Although not entirely eliminated by suction or blowing, the spanwise extent of the vortex influence can be reduced by the several wall-flow augmentation schemes noted.

In a generalized study of the separating confluent boundary-layer, it would be anticipated that post-stall testing of the airfoil would be probable if conditions leading to flap-surface separation are to be represented. For a flapped airfoil designed for trailing-edge separation, such as the GAW-1, surface separation could be initiated and become quite extensive on the main-element before the flap surface-flow would undergo separation as well. The evaluation of the separating flow on the flap (or confluent boundary-layer) could therefore possibly be in the post-stall angle-of-attack range.

For the foregoing reasons, it was believed that some wall augmentation system should be employed in the present study although the 2-D flow qualities in the ERF were known to be reliable up to wing stall conditions. Figure 9 portrays earlier results from pressure-tests of an 11-inch chord, GAW-1 type, flapped airfoil in the ERF-facility; sidewall augmentation was not employed in this instance. These tests were conducted with a large-span airfoil carried through the tunnel walls and initially positioned at the model centerline. Progressive lateral movement of the model provided local surface-pressure data in the interval between the tunnel centerline and the sidewalls. As noted in figure 9, there is a slight drop-off in integrated lift as the wall is approached due to the thickening of the boundary-layer within the juncture region. At modest post-stall angles-of-attack, the loading is essentially constant over a substantial portion of the span.

While the ERF is equipped with sidewall suction with slots positioned just upstream of the model, it was found that local blowing at the wall provided a more positive control of the spanwise loading when considering the full range of anticipated test conditions. For the additional reason of compatibility with full-peripheral LV-viewing of the model surface, as well as for the outer-flow region, the sidewall blowing scheme indicated in figure 10 was employed in the study. The blowing ports, arranged around the model sub-surface on the main-element were individually controlled through separate plenums. Although there were no blowing ports installed in the

flap-surface, due to interference with pressure-port leads, the cove-region port was directed at the flap/wall juncture (see figure 10) to provide some flow-control in the sidewall region. By use of the LV rapid-scan analog system, the spanwise variations in close-to-surface velocity components could be quickly adjusted for achieving constant span-loading at any chordwise position or angle-of-attack. Figure 11 depicts an LV-analog trace, with and without wall blowing, which exemplifies the usage of the system and the blowing effectiveness. Extensive test check-outs provided pre-selected blowing rates and distributions which could enhance the quality of the two-dimensional flow distribution as a function of airfoil configuration, angle-of-attack, and tunnel speed.

3.4.3 Wall-Effect Considerations.

The experimental data presented in the present report (Volume I) and in the corresponding data report (Volume II) represent the pressure and boundary-layer parameters as measured without correction for relatively small wall constraint effects in the ERF. While the surface-pressure and integrated lift data can be readily corrected for such effects, it would not be possible to treat the boundary-layer parameters in a like manner. As will be shown in Section 4.1.1, pressure distribution comparisons between the present GAW-1 airfoil data and that of a larger tunnel (Reference 23) are in reasonable agreement through stall when accounting for significant differences in test Reynolds numbers. Similar experimental agreement is shown in the same section with the theoretical predictions for the attached-flow

cases. From this it has been concluded that the present data is reasonably representative of the GAW-1 aerodynamic performance at the specified test Reynolds number and that unusual tunnel-induced effects did not produce uncharacteristic boundary-layer behavior in the LV-measurements.

3.5 Test Conditions

3.5.1 Wind-Tunnel Conditions

The nominal freestream dynamic pressure for the ERF-testing of flapped configurations was 20 psf which yielded a test Reynolds number of 0.62×10^6 based on the 9-inch airfoil (basic) chord. An exception to this was early trial tests, including LV-surveys, with the single-element airfoil which were performed at $q \approx 30$ psf ($R_{NC} = 0.76 \times 10^6$). Extensive preliminary testing on the flapped cases at tunnel speeds higher than $q = 20$ psf indicated that there could be instances, such as pronounced surface-separation or for regions characterized by high-speed, curvilinear flows (leading edge flow), where LV-data rates could be temporarily lowered from what appeared to be a reduced level of seeding-particle entrainment. At the lower tunnel speed representing 20 psf, this effect was not pronounced and uniform LV-data rates were generally observed. For this reason, the lower tunnel speed was selected for the majority of the tests.

3.5.2 Transition

Flow visualization studies using an oil-based titanium-dioxide solution showed that transition occurred naturally at about 5 percent chord on the GAW-1 top surface at all angles-of-attack of interest in the LV-studies (see figure 12(a)). This observation was subsequently confirmed by examination of the LV-measured boundary-layer profiles on the main-element as well as the skin-friction levels derived from Preston-tube measurements. On the airfoil lower surface, figure 12(b) transition to turbulent flow occurs further aft at $x/c = 0.50$ to 0.65 , but always ahead of the flap cove entry located at $x/c = 0.68$. Therefore, the initial conditions at the slot entry represented a fully turbulent boundary-layer flow condition.

As a result of the preliminary transition studies, it was concluded that boundary-layer transition would occur naturally on the upper surface at 5 percent chord (or less) and ahead of the cove entry on the lower surface under the selected test conditions. To avoid possible unwarranted boundary-layer disturbances, the decision was made to conduct all of the tests without artificial "trips." Exceptions to this were those configurations using the leading-edge slat. Transition was fixed at 10 percent slat chord by the application of 0.0065 Ballantini glass spheres. This step was taken in recognition of the relatively low chord Reynolds number of the slat and as a consequence of oil-flow studies which showed some possibility of incomplete natural transition and possible laminar separation for some slat positions.

3.6 Test Configurations

Prior to selecting a configuration matrix, preliminary investigations were undertaken to assess the types and regions of flow-breakdown on the GAW-1 in its various high-lift modes and the sensitivity of this flow behavior to control by slot-geometry variations. These preliminary studies made extensive use of the LV-analog system, surface pressure measurements and oil-flow techniques; theoretical back-up utilized the NASA Multiple Airfoil Program (MAP).

3.6.1 Matrix Selection

Although the single-element airfoil (identified as CASE A) exhibits no confluent region, it was felt that the multi-element flow characteristics would be largely an outgrowth of those exhibited by the basic airfoil. Tests of the single-element case showed, as anticipated, transition occurring on the upper-surface at about 5 percent chord and a trailing-edge (turbulent) stall commencing at 4-6 degrees angle-of-attack and moving forward with increasing angle-of-attack. This basic flow pattern was highly consistent well beyond the lift-curve break ($C_{l_{MAX}}$) with or without artificial boundary-layer "trips."

With the two-element case (main-plus trailing-edge flap), tests at the lower flap deflections (20°, 30°) showed highly consistent

flow-breakdown patterns which remained essentially unchanged over a wide range of slot geometries although the lift performance did reflect such changes. As in the single-element case, flow separation was initiated at the trailing-edge of the main-element at $\alpha \approx 4^\circ\text{--}6^\circ$ producing an extensive, turbulent wake overlaying the flap confluent region. The primary flow feature observed on the airfoil undersurface was the vortical flow pattern at the cove entry (see figure 1) which appeared to remain stationary and relatively stable for all configurations. A conclusion from these studies was that there was little additional information to be gained by performing detailed flow-surveys on the 20-degree flap configuration and that the 30-degree flap case (CASE B) provided the essential features of the flow-behavior noted.

At the higher flap deflection of 40 degrees, (CASE C), trailing-edge stall on the main-element was still the predominant flow pattern although slot geometries were found that produced some surface-separation near the flap trailing-edge. Interestingly, in these tests, flap pressures often appeared to evidence extensive surface-separation while the preliminary LV-survey showed a well-attached slot-flow up to or near the flap trailing-edge. The highly turbulent wake from the main-element which produced this effect also showed some evidence of time-dependent or periodic structures in the wake through variations in repeated, time-averaged LV-measurements. The 40-degree flap slot geometries, selected for the detailed LV-studies, encompassed those which generally characterized confluent boundary-layer behavior under both normal and adverse (or

non-optimum) geometric arrangements of the slot since the latter tended to evidence additional surface-separation on the flap.

The leading-edge slat, two-element case (CASES D, E, F) represented an important configuration inasmuch as the extensive length of confluent region (figure 1) and the tendency toward trailing-edge, main-element stall provided the basis for evaluating extensive separation in the confluent region. Over most of the configurations studied, the predominant flow pattern was again main-element, trailing-edge stall with C_{lMAX} occurring at significantly higher angles than the single-element case as would be expected with a leading-edge device. The magnitude of the stall angle ($\alpha \approx 35^\circ$) for near-optimum slot arrangements at high slat angles produced the possibility of excessively high blockage effects within the test-section and, as a consequence, a maximum slat angle of about 42 degrees was selected for detailed LV-coverage. In a further attempt to establish an alternate, separated initial condition to the main-element flow, the slat angle was progressively reduced to increase the upper-surface adverse pressure gradient. While somewhat unconventional in appearance, a slat-angle of 27-degree was identified as that which produced a separated slat wake for interaction with the slat and main-element upper-surface flow-fields. An observation with this configuration was the highly unstable nature of the slat wake which exhibited periodic flow disturbances and, in some instances, periodic flow reversal.

Further consideration of three-element cases showed no additional

flow-separation phenomena that had not been observed earlier on the two-element configurations. Consequently, several typical cases were selected for the detailed flow studies.

As a result of the foregoing preliminary work, the configuration matrix of Table V was established for further study by LV-digital measurements of velocity profiles, turbulence intensities and Reynolds shear stress. A matrix designation number (A-1, A-2, etc.) for each configuration is shown in the table; these are used for identification purposes in the present document as well as in the data report, Volume II.

3.6.2 LV-Data Axes

With the matrix established, an orientation system for both on- and off-surface LV-measurements was used as shown in figure 13. All on-surface profiles were obtained by computer-controlled traverses normal to the local airfoil surface. Since the LV-positioner is aligned in the tunnel axis-system, it was necessary to define a positioner translation angle (i.e., relative to the tunnel axis, see figure 13) at each surface position and angle-of-attack.

For off-surface traverses of upstream and wake-flows, the axis-systems or "trailers" shown in the figure as A, B, and C were employed. Also the "zero" position for x/c -variations on the three-elements were selected as shown. For further identification in tabulated results, the subscripts, S, M, F, W, are used to denote

slot, main, flap or wake profiles, respectively. For profiles located ahead of the main-element or slot, the x/c -values carry a negative sign and are subscripted as M (main) or S (slat). These systems are used throughout the study documentation for rapid identification and recovery of the tabulated boundary-layer or wake data of specific interest.

3.7 Data Reduction

3.7.1 Conventional Instrumentation

To derive comparative data between the LV- and pressure-probe measurements, the two LV-mean velocity components were resolved into a vector which could be compared directly with that from the pressure-probe or hot-wire. Small inconsistencies in the outer-flow conditions, introduced by tunnel operating conditions, required that the local velocity data be non-dimensionalized by the outer-edge velocity; this provided comparative shapes of the profiles as derived from the several instruments.

To obtain turbulence information from the hot-wire, the data were recorded on magnetic tape as a function of time (figure 14). The RMS values were determined from 4096 samples and then divided by the local mean. It was difficult to determine what would constitute a valid comparison with LV-derived turbulence quantities since the LV-data is acquired in terms of u' , v' components and hot-wire in terms of u'

only. It was assumed that the v' -quantity does not play a major role in the analysis and that only u' represents the primary parameters to be evaluated comparatively with the hot-wire results. In this procedure, the hot-wire data were not linearized which could introduce some small nonlinearities in the results. In both of the calibration and data reduction programs the hot-wire was compensated for mean tunnel temperature variations in the calibration form of:

$$\text{Velocity} = \left[\frac{\text{VOLTS}^2 - A}{B} \right]^C \quad (1)$$

where voltage is measured across the bridge while exponent C and constants A and B were optimized for best linearity across the calibration range.

3.7.2 LV-Data Reduction

The LV system is basically a stand-alone system designed to obtain, evaluate, and plot the results. A data reduction scheme has been developed in conjunction with the Vax 11/780 computer system, figure 15. There are three major programs that are used to obtain the final results. LVNEW is the interface program that converts the raw data, recorded on tape by the MAC-16, into forms that can be used by the Vax 11/780. The output data of LVNEW is used by the LASER program

to manipulate the data into a form that can be plotted and printed in NASA-approved formats. This program also calculates the actual translation of the LV traverse system, which is then applied as a simple rotation scheme to obtain data normal to all surfaces. The existing Lockheed-Georgia plotting routines, LV2, LV3 and Plot R, display the information in two forms. The first, LV2, is in an individual format which focuses on details of a single profile, and second, LV-3, a composite plot which gives the overall picture of the flow field. These composites are of velocity vectors, Reynolds shear stress, u -prime (turbulence), v -prime (turbulence), constant velocity lines, (u or v) or any combination.

3.8 Data Accuracy

3.8.1 Conventional Instrumentation

For the conventional instrumentation studies, it is believed that the test results are consistent with the accuracies generally attributed to pressure taps and probes of the types employed when combined with state-of-the-art electronic read-out equipment. With the present pressure probes, only those position corrections normally employed in close-to-surface measurements have been included in the data reduction. Reference 24 is typical of the available literature pertaining to these as well as other data corrections and the basic accuracies customarily associated with such systems.

The accuracy of hot-wire system as opposed to that of the LV has been and continues to be a subject of debate within the industry. In recognition of the complexities involved in such comparisons and in view of the extensive use of the LV on the present program, a substantial effort has been made to attempt clarification of some of the issues on this subject. In the paragraph which follows, a state-of-the-art review of LV-characteristics is summarized. Relative accuracies of the hot-wire in providing boundary-layer measurements are considered in some detail in Section 4.3, Conventional Instrumentation Comparisons.

3.8.2 LV Error Analysis

In view of the unusual adaption of the LV-system to data acquisition on a production basis and in contrast to its normal use as a basic research tool, it is appropriate that some discussion of possible error sources be presented. As with any measurement device, these are two types of errors possible in laser-velocimeter measurements - biasing and random errors. Biasing appears as a systematic error with the same magnitude and in the same direction from one set of data to the next. Random errors are haphazard in nature and can generally be minimized by averaging a given set of data over a large number of repeated measurements. Of the two, biasing is generally the most difficult to detect and eliminate.

The development of the LV system has progressed to the point where the sources of biasing have been identified and techniques for avoiding them incorporated. The sources of biasing in measuring the mean flow velocity are fringe biasing, spatial resolution, particle lag and velocity biasing. Fringe biasing occurs whenever a particle does not traverse enough fringes for a valid measurement. In its simplest terms, a particle traversing the measurement volume at an angle parallel to the fringes will not be detected. This bias significantly affects shear measurements; however, use of a Bragg cell eliminates this problem, as shown in Reference 17. Since a Bragg cell is used in the Lockheed-Georgia facility, this source of biasing is eliminated.

Spatial resolution becomes an important consideration in performing measurements in flows with steep velocity gradients such as flow within a boundary layer. Here the velocity can vary over the measurement volume producing erroneous turbulence intensity measurements. In Reference 25, possible techniques are presented for correcting this bias although such were not used in the present program.

Since it takes a finite amount of time for the seeding particles to react to the flow, particle lag can also be a source of biasing in regions of highly accelerated flows. With the flow velocities attainable with the ERF wind tunnel, this biasing can arise since, for a uniform particle distribution, more high-velocity particles will be detected than low-velocity ones. This biasing has been accounted for in the data reduction programs used in these investigations by employing techniques referred to in Reference 18.

In making turbulence intensity measurements, other sources of bias occur in addition to those mentioned. The first is the noise associated with the photomultiplier tube. This bias is avoided in the present facility by using the methods developed in Reference 19. Basically, this method consists of taking the signal from the photomultiplier tube, splitting it, and processing the two signals by separate electronic packages. The particle passes through twelve fringes in all with the first signal being processed over the first eight fringes and the second signal processed over the last eight fringes. By forming the cross product of the two signals and

averaging, the random photomultiplier tube noise averages out and the true turbulence intensity of the flow results.

A second source of error in the turbulence intensity measurement arises from the digital resolution of the LV processor. This limits the lower limit of turbulence intensity detectable by the present LV system to about 0.1 feet/sec. Finally, if the beams are not parallel, the fringe spacing is not uniform over the measurement volume giving rise to a false turbulence reading. Estimates of this turbulence level indicate that it is about 0.5 feet/second. This combined with the aforementioned 0.1 foot/sec due to digital resolution sets a lower limit of turbulence measurements by the Lv to about 0.6 fps.

4.0 RESULTS AND DISCUSSION

In the present section, test results are discussed first from the standpoint of the surface-pressure measurements (Section 4.1) for which some comparative GAW-1 airfoil results from other sources are presented. In Section 4.2 the LV-measurements are given in terms of velocity profiles, turbulence intensity measurements and shear-stress surveys in composite form. Sample cases of selected profiles are given in plotted and tabulated form to illustrate the formats of the bulk of the test results given in Volume II.

Section 4.3 will discuss results from the conventional instrumentation study which compares the LV-derived measurements with those from total-head and static pressure probes, hot-wires and several approaches to skin friction data. Finally, in Section 4.4, certain boundary-layer and wake parameters, as derived from the present experimental work, are reviewed in terms of their theoretical counterparts from several sources such as the MAP, or "law-of-the-wall" or "law-of-the-wake."

4.1 Pressure-Test Results

4.1.1 Comparative Results

A summary of integrated lift coefficients derived from selected configurations in the ERF-tests are compared in figure 16 to results

from other sources. The theoretical data shown were calculated in the MAP-program using ERF-tested gap and overhang positions as indicated in the tabulation. The WSU-results shown (Reference 23) do not necessarily reflect the same gap geometries as used in the ERF-tests since gap-optimization in the present tests was not an objective. For perspective on these results it may be noted that the referenced experimental work represents force-balance and pressure testing with wall-corrections included. The tests were performed in a 7x10-foot low-speed tunnel equipped with a three-foot span (two-dimensional) test-section insert. The model chord of 2 feet (29 percent flap chord) yielded a tunnel height-to-chord ratio (h/c) of 3.5 and a chord Reynolds number of about 2.2×10^6 ; the transition position was fixed. These parameters may be compared to those corresponding to the ERF-tests of $h/c = 3.33$ and $R_{NC} \approx 0.6 \times 10^6$, transition-free. The substantial difference in test Reynolds number would be expected to produce a significant loss in $C_{l_{MAX}}$ in the ERF-results as well as a progressive loss in flap effectiveness with flap deflection at the lower angles-of-attack. These are the general trends to be noted in the comparisons shown.

For the single-element airfoil, both sets of experimental results are reasonably well predicted by the theoretical C_l at $\alpha = 0$ degrees. Separation onset in both sets of experimental data occur at the airfoil trailing-edge for $\alpha \approx 4-5$ degrees and as anticipated, with a much thicker separated region present in the lower Reynolds number case. The theory would not correlate well at higher angles since a separated-flow model is not included in the present MAP program. The

marked difference in maximum lift for the single-element airfoil appears to be consistent with the trends portrayed in Figure 17 wherein NASA tests (Reference 26) and WSU (Reference 23) results for the single-element GAW-1 airfoil are plotted and extrapolated to the ERF Reynolds number. The effect of artificially fixing the transition on this airfoil has, as shown, very similar results across the Reynolds number range portrayed; that is, an artificial thickening of the trailing-edge separation region at stall angle-of-attack and an uncambering influence such as to reduce $C_{l_{MAX}}$.

With flap deflected, the comparative results of figure 16 show a gradually increasing loss in flap-effectiveness with δ_f ($\alpha = 0^\circ$) for the ERF-tests, with respect to the WSU-results, while both sets of experimental data show a similar degradation relative to the theory; this latter observation reflects the behavior of the confluent boundary-layer as currently modeled in that it does not thicken as rapidly and approach separation as quickly as does that in the experimental data. For 40 degrees of flap angle, the ERF-data indicate that the gap and overhang positions were significantly different from that which would provide optimum lift inasmuch as maximum lift is slightly lower than that for $\delta_f = 30$ degrees.

Corresponding pressure distribution comparisons are shown in figures 18 through 24 which reflect the MAP-program, the Reference 23 data and the ERF-results. Figures 18 through 20 portray single-element comparisons while figures 21 through 24 provide similar data for the 30-degree flapped cases. In the latter figures, the gap

geometry represents that from the ERF-tests and theory and may not conform identically to those employed in the Reference 23 data.

In general, the single-element surface-pressures compare favorably with theory in the lower angle-of-attack range. The trailing-edge separation starts at about 5-6 degrees (figure 19), progresses rapidly forward with angle-of-attack and, at stall (figure 20), has moved to the $x/c \approx 0.55$ position. Except for minor differences, the ERF-pressure distributions also compare favorably with the WSU-results up to stall where the difference in maximum lift is reflected in the surface pressures.

Similar types of surface pressure comparisons are given in figures 21 through 24 for the 30-degree and 40-degree flapped configurations. The major difference between the experimental results and the theory appears to be in the flap aerodynamic loading where the theory, reflecting the current confluent boundary-layer model, tends to overpredict the loading. The WSU-results also show generally higher (negative) pressure levels as would be expected for these higher Reynolds number tests.

4.1.2 LV-Matrix Pressure Data

Corresponding to the LV-survey test matrix of Table V, figures 25 through 28 present the integrated lift data for the selected test configurations A through F. These curves are provided as an indicator of the approach-to-stall condition for each of the basic flap and slat

combinations for which LV-surveys were made and the relative performance of each. Corresponding to these data, selected examples of the individual pressure distributions for each configuration in the LV-survey matrix are detailed in figures 29 through 34. The trends noted in these data are consistent with those observed during the configuration selection process. The complete set of pressure distributions for all LV-survey configurations (A-F) is given in Volume II.

4.2 LV-Profiles

4.2.1 LV-Composite Plots

In the interest of providing an efficient means of identifying the tabulated data associated with a specific configuration, composite velocity profile, plots have been developed as illustrated by the examples of figures 35 through 40. These data formats, in addition to providing a source for data identification, graphically provide an overall view of the airfoil flow-field. Test numbers are given at the top of each figure while the individual profiles are identified by a test run number which can be cross-referenced to the tabulated data of Volume II.

Figure 41 shows examples of corresponding composite plots of shear stress, figure 41(a), and the two turbulence components, u and v (figures 41(b) and 41(c)), respectively. Source data for such

plots are the Volume II tabulated results as illustrated in Table VI corresponding to LV-Run 42 and as called out on figures 41(a) through 41(c). Volume II also contains a complete plotted record of the three LV-measure quantities as illustrated in the example of Figure 42.

As indicated in figure 43, computer graphics can be employed to enlarge significant areas of the flow-field for added visual detail. Figure 43(a) portrays the flow-field in the vicinity of the leading-edge slat while, for the same configuration, the flap-cover area is detailed in figure 43(b). The capability for exploring unusual flow phenomena with LV-studies is highlighted in this latter figure which clearly shows and quantifies the stationary vortex established in the flap-cove area just ahead of the slot-exit. This type of experimental data, generally unavailable through conventional instrumentation studies, addresses an obvious need in current theoretical modeling processes for realistic high-lift system design.

A second unusual case is illustrated by the enlargement shown in Figure 43(c) representing an unconventional slat deflection angle. As noted in an earlier discussion, this configuration was selected for study in an attempt to force flow separation on the slat upper-surface such that the merging of this wake with the slot-flow on the main-element upper-surface could be analyzed. The desired flow-separation was accomplished as illustrated by the reversed flow on the slat-surface. This proved, however, to be a highly unstable flow condition with periodic re-attachment and re-separation occurring. Repeated LV-measurements of the time-averaged velocities

catch such flow changes in various stages of periodic behavior. As seen in the composite velocity profile immediately downstream of the slat, Figure 43(c), one mode of this flow appears to be a strong upward penetration of the separated wake by the slot-flow while a second is the completely separated slat wake overlaying the slot-flow which closely follows the airfoil surface.

Further use of computer-graphics to highlight flow details is illustrated in figure 44 where contours of constant velocity ratio have been constructed for Configuration F-1. Figure 44(a) shows the contours made up of the streamwise component (u) while the normal-to-surface component (v) is represented by figure 44(b).

4.3 Conventional Instrumentation Comparisons

Comparisons have been made between LV-measurements of selected boundary-layer velocity profiles and those obtained from a single-element hot-wire as well as with a pitot-static probe. Turbulence intensity comparisons in the several types of flow-fields may also be made with the LV- and hot-wire data. For skin-friction evaluations, Preston tube measurements may be compared indirectly with LV-measurements of the velocity profiles. These comparisons are considered in more detail in the paragraphs which follow.

As will be noted specifically in the discussions of turbulence-intensity measurements by alternate instrumentation, a separate study was undertaken as believed appropriate to more fully developing basic

differences between hot-wire and LV-measurements. This study, conducted under closely-controlled test conditions, provides data complementary to that acquired under the main-line program and expands on basic conclusions made relative to turbulence measurements. Details of the test set-up and results are included in Section 4.3.2, Turbulence Profiles.

4.3.1 Velocity Profiles

Several examples of mean velocity profiles as obtained from the LV, hot wire and pitot probe are compared in figure 45. A typical boundary-layer comparison, figure 45(a) shows excellent agreement between the three instruments. As noted earlier, in many cases, the hot wire and LV-data represented two independent tunnel runs although the hot wire and pitot probe were always run simultaneously. As will be elaborated on in a subsequent paragraph, simultaneous measurements with the LV and hot wire were found to be possible without incurring wire contamination. Therefore, the hot wire was calibrated against the LV, with periodic accuracy checks, using techniques similar to those of Reference (27).

The second velocity profile shown, figure 45(b), represents data obtained in the confluent boundary-layer region and characterizes the other extreme on the velocity correlations obtained. The discrepancies noted are attributed to small variations in spatial position or, possibly, the influence of the probe on the flow field. The 5-10 per cent variations exhibited by the pressure probe are

probably due to a sensitivity to highly turbulent flow or to the flow angularity relative to the probe axis. The preponderance of the velocity profile comparisons obtained fell between the two extremes portrayed by figure 45, generally varying from excellent to good.

It was noted in the process of acquiring the comparative profile data that positioning accuracy with both the pressure- and the hot wire probes was poor relative to that afforded by the LV-system. Although the probe drive was a high resolution mechanism, probe vibration and blow-back, particularly in highly-turbulent regions, generally prevented the realization of the same levels of accuracy and consistency as could be obtained with the LV system.

4.3.2 Turbulence Profiles

The study of the unsteady flow properties in the boundary-layer of the GAW-1 airfoil was limited to comparative measurements between the LV-system and the hot-wire probe only. Figures 46(a) through 46(c) show examples of the turbulence-intensity measurements as obtained with the two instruments. For the two boundary-layer profiles, figures 46(a) and 46(b), the comparison shows a mismatch on measured turbulence as high as 40 percent as the wall is approached. On the other hand, figure 46(c), representing a wake-station, shows much better agreement for the two instruments. Inasmuch as the differences noted in the boundary-layer comparisons could not be readily explained in the context of the data available, it was apparent that more definitive data from both instruments should be

obtained. This led to a supplementary study which had the following objectives:

- o Examine the basic hot-wire measurement characteristics relative to those of the LV.
- o Study the effects of several sampling techniques on the turbulence correlation.
- o Examine the correlation under more controlled test conditions downstream of a uniform grid with variable geometry hot-wires.

MEASUREMENT CHARACTERISTICS - External factors that can adversely effect hot-wire measurements would include non-linear responses, ambient temperature variations, influence of turbulence levels on the mean, operation near a solid-surface, and time resolution characteristics. These factors are discussed at greater length in Reference (28) and will be implicit to some of the following discussions.

In examining the hot-wire characteristics, it was desirable that LV- and hot-wire data be taken simultaneously. To determine the effects of LV seeding on the hot wire, two cases of clean flow and contaminated flow were studied. The effects of wire contamination were monitored by checking the consistency of the hot wire calibration curves with and without seeding material present in the measured flow

field. In addition, the sensitivity of the wire calibration to the seeding particles was examined via a comparison of the rms spectra. Results from both of these techniques indicated that seeding material impinging on the wire did not adversely affect the hot wire measurement.

To compensate for the non-linear relationship of the wire output voltage to the mean velocity, linearization was performed through post-processing techniques. It was also determined that the distribution of the hot wire rms voltages fell on the near linear portion of the calibration curve thereby making the average rms voltage directly proportional to the average rms velocity. To prevent ambient temperatures from influencing the results, voltages were temperature-compensated using accepted techniques (Reference 29).

As sketched in figure 46(d), the single hot wire measures only a magnitude while the LV-system measures two distinct components of the flow. To vectorially add the mean components of the LV poses no problem when comparing to the mean of the hot wire. However, vectorially adding the averaged u' and v' components would not necessarily produce the magnitude of velocity fluctuation as seen by the hot wire. Further insight in this regard was obtained by forcing the LV-system to display data in a manner similar to that of the hot wire. This was accomplished by summing the instantaneous total mean U and V -components and creating a total fluctuation resultant. This process forces the LV to average the data in the desired manner, which is only possible because the LV acquires both U and V components

simultaneously. Typical results using this technique are shown in figure 46(e). Comparisons in the low level turbulence range (less than 3 percent) should be ignored since the low level electronic noise is normally eliminated by a cross correlation of the two components (see Section 3.8) rather than by the described technique. As noted on the figure, the averaged value of u' compares favorably with the simulated hot wire value in the higher range of turbulence. Therefore, from these considerations, the need for considering the v' -component of the LV in subsequent comparisons was eliminated although the total measured magnitude of turbulence by the LV was still monitored.

SAMPLING TECHNIQUES - Using both fixed and random sampling techniques, hot-wire data were obtained for various sampling periods and rates to determine the influence on the LV/hot-wire comparisons. The LV-system sampling rate could not be varied directly since this is primarily set by the detection properties of the instrument; sampling rate can change, however, as the measurement-volume approaches the surface. The hot wire mean and fluctuating components were monitored by a rms voltmeter in addition to the computer acquisition of these parameters. Since no significant variations were observed in the results from these studies, it was concluded that sampling techniques played little part in the subject comparisons.

UNIFORM GRID TESTS - Because of apparent discrepancies between the hot wire and LV data, a series of tests were undertaken under conditions that eliminate the velocity gradients and surface effects present in

the GAW-1 studies and would approximate the velocity-range under which these earlier results were acquired. A turbulence intensity level (u'/U_{local}) of about 10-15 percent of a mean velocity of about 50-100 fps represented the nominal conditions under which the original data-mismatch was observed. To establish these conditions as well as to provide for an isotropic turbulence test condition, a uniform grid test arrangement or a fully developed pipe flow test was suggested. Since the grid test was more compatible with the original GAW-1 test program, it was selected for continuing the detailed comparisons of LV and hot wires.

The uniform grid test, figure 46(f), used a grid constructed of 0.25 inch tubing spaced 1.0 inch apart, center-to-center, which, based on the data of Reference (30), would give the desired results at $X/M < 10$; "X" is the downstream position behind the grid and "M" is the mesh. Subsequent flow-surveys at various values of X/M showed the flow to be both isotropic and homogeneous across the desired velocity range.

As were noted in the original tests, simultaneous measurements by the LV and the standard hot wire, (free tunnel, grid in place), showed little difference in the mean flow velocities but with discrepancies appearing in measured turbulence level varying with both velocity and turbulence magnitude. Further investigation led to consideration of the effects associated with the active length of the hot wire. Separate hot wires were used to represent this variation: a standard wire, 0.1 inch, and a miniature wire, 0.05 inch. A third wire, which

was etched, was used to represent the same active-length as the miniature element but had the same overall length as that of the standard wire. Comparing turbulence measurements by all three wires to those of the LV, showed unexpected variations with freestream velocity in the hot wire results, whereas, the LV data remained essentially constant with velocity, figure 46(g). These results indicated that the spatial resolution of the hot wires employed in these tests was a significant factor in the boundary layer comparative data. Additionally, the favorable comparison between the etched wire and the miniature wire not only confirmed the repeatability of the data but also showed that the prong effects were minimal.

To further study this finding, spectral data was developed for the hot wires at a fixed mean velocity as shown in figure 46(h). In this figure, RMS spectral data have been normalized such that amplitude is displayed in velocity (fps) which compensates for variations in calibration slopes and voltage magnitudes. As indicated, the large wire measurements begin to deviate (or roll-off) at frequencies of the order of 1500-2000 Hz for the miniature wire. Integrating the difference between these spectra results provide variations in RMS values which correspond in magnitude to those of the discrepancies noted in figure (46g). This would indicate that the standard wire attenuates the perceived perturbation, or in other words, eliminates the small-scale or higher-frequency eddies. Using a length-scale represented by the active portion of the hot wire, a roll off frequency can be predicted for a fixed mean velocity. Calculations of this type showed a theoretical roll-off frequency of about twice the value as

obtained experimentally. This implies that the hot wire results have attenuated eddies whose length scale is on the order of twice the active length of the hot wire.

The implication that the LV is not affected by the spatial resolution of the measurement volume can be explained by examining an individual measurement. Compared to the critical length scale of the hot wire (the sensing length), the LV reconstructs the time history via random measurements of individual particles as they cross four fringes. Therefore, for two-dimensional flow, the critical length scale of the LV is the distance between the four fringes and not the absolute length of the measurement volume itself.

Extrapolating the trends shown in figure 46(g) via a cubic spline curve fit, and plotting the correction, figure 46(i) provides evidence that the discrepancies noted in the GAW-1 turbulence measurements are of the same order of magnitude as the spatial resolution errors derived for the hot wires in the uniform grid tests. This not only confirms the repeatability of the error introduced into the hot wire measurement but also validates the LV data taken on the GAW-1. It is therefore understood that the agreement of the two devices in the wake, and not in the boundary layer of the GAW-1, can be attributed to the differences in length scale of the measured eddies. Careful examination of the wake profile, figure 46(c) shows a slight discrepancy in the area where the boundary layer turbulence has been transported. That is to say, the residual boundary-layer eddies found in the measured portion of the wake have not yet migrated

into larger eddies.

A general conclusion resulting from the supplementary studies is that hot wires can be subject to errors in turbulence measurements due to a sensitivity in spatial resolution. Throughout these studies, the LV provided consistent data without corresponding discrepancies being apparent. Therefore, for the GAW-1 test program, it is believed that the LV system provided more consistent and reliable turbulence data than the hot wire probes.

4.3.3 Skin-Friction Measurements

Among the various ways in which the local surface-frictional force may be evaluated, the Preston-tube seems to be one of the more simple and reliable devices. This requires total-head measurement on the surface plus the surface static pressure at the same point. Under the conventional instrumentation study, the traversing pressure probe total-head tube (flattened 0.010 inch tube height) placed on the airfoil surface, together with an existing static pressure port, provided the two pressure measurements.

As an alternative method, local skin-friction can be evaluated from boundary-layer velocity profiles if such measurements can be carried to the near-surface positions characterizing the "overlap-region" defined by the "law-of-the-wall," (Reference 31). Using LV-acquired data, a typical profile can be plotted in the semi-log form of figure 47 or as a "Clauser-plot." Local

skin-friction levels can be superposed on this plot using the following relationships:

$$\frac{U}{U\tau} = \frac{1}{K} \ln \frac{YU}{\nu} + B \qquad C_f = 2 \left(\frac{U\tau}{U_{MAX}} \right)^2 \quad (2)$$

Letting $(K, B) = 0.41$ and 5.0 , respectively, and revising the logarithmic base gives:

$$\frac{U}{U_{MAX}} = 2.97 \sqrt{C_f} \log \frac{YU_{MAX}}{U} + 1.985 \sqrt{C_f} \log C_f + 2.938 \sqrt{C_f} \quad (3)$$

As noted in figure 47 the LV-derived value of skin-friction coefficient, C_f , is 0.0019-0.0020 by the above method whereas an evaluation by means of a Preston-tube gave a value of 0.0022. A 10 percent error in skin-friction evaluations is a generally accepted accuracy level in conventional test work, particularly where alternate instrumentation is employed.

The foregoing two methods have been used to develop and compare skin-friction levels and trends on the upper-surfaces of several of the study-matrix configurations. These are shown in figures 48 through 50. In some of the LV-runs used to develop these comparisons, the number of data points falling within the overlap region and from which skin-friction levels could be deduced were sparse. This is particularly true for forward chordwise positions where the boundary-layer is thin relative to the 0.005 - 0.010 inch LV-measuring volume. Consequently, most of the "Clauser-Plot" skin-friction evaluations were performed in the chordwise interval $0.6 \leq (x/c) \leq 0.96$. Figure 48 shows a good-to-excellent comparison between the Preston-tube skin-friction results and those from the LV-deductions. The MAP-calculated values of skin friction, also given on this figure, were obtained by using the same pressure-distribution in the main-element upper-surface as was found experimentally and only fair agreement is indicated.

Similar skin-friction comparisons on configurations C-1 ($\delta_f = 40^\circ$) and F-3 ($\delta_f = 40^\circ$, $\delta_s = 42^\circ$) are shown in figures 49 and 50, respectively. Where corresponding LV- and Preston tube measurements were made, the agreement is generally good.

From this phase of the conventional instrumentation study, it would be concluded that the LV-derived profiles can provide a reasonably accurate measure of skin-friction level in regions where the LV-control-volume size does not severely limit access to the

boundary-layer "overlap" region.

4.4 Comparative Boundary-Layer and Wake Parameters

4.4.1 Comparisons of Theoretical Boundary-Layer Parameters

The LV-derived velocity profiles have been processed to derive ordinary turbulent boundary-layer parameters such as θ/c , δ^*/c , and δ/c etc. The trends and magnitudes of such parameters can then be compared to those developed from MAP-calculations. Such comparisons have been restricted to attached flow conditions on the main element upper surface and to those matrix configurations surveyed at the lower angles-of-attack. Additionally, MAP calculations were performed on the basis of slat and main-element surface-pressure distributions closely approximating that determined experimentally for the configuration. Figure 51 shows the results of such comparisons for configurations B-4, C-4 and F-1. The data for the first two configurations represent ordinary turbulent boundary-layer parameters whereas the data for configuration F-1, figure 51(c), represents confluent boundary-layer development on the main-element due to the presence of the leading-edge slat.

The ordinary turbulent boundary-layer parameters shown in figures 51(a) and 51(b) appear to be reasonably well predicted in trend by the MAP although θ/c and δ^*/c are generally over-predicted by the program relative to that measured experimentally. In figure 51(c), good

agreement is shown between the measured and calculated parameters within the currently-modeled confluent boundary-layer region downstream of the slot. As noted, the break in the calculated results represents an interface between the confluent slot-flow core region and the confluent Main Region I as defined in Reference 14 by the integral-method of modeling for this type of boundary-layer.

4.4.2 Law-of-the-Wake Comparisons

As described in Reference 31 and 32, an analytical description of the outer wake layer, or mixing region, of a turbulent boundary-layer can be combined with that of the inner layer such that a single formula can be used to represent the complete velocity profile. From Reference 32 this has the general form of:

$$\frac{K g(II, y/\delta)}{y e} = f(u^+) \quad (4)$$

where:

$$g(II, y/\delta) = 1/K (1 + 6II) (y/\delta)^2 - 1/K (1 + 4II) (y/\delta)^3 \quad (5)$$

and:

$$f(U^+) = U^+ + e^{-A} \left[e^{KU^+} - 1 - KU^+ - \left(\frac{KU^+}{2}\right)^2 - \left(\frac{KU^+}{6}\right)^3 - \left(\frac{KU^+}{24}\right)^4 \right] \quad (6)$$

At the outer-edge of the boundary-layer, $y = \delta$ and the wake parameter II, which is a function of both local pressure gradient and turbulence level, has the value of:

$$g(II, y/\delta) = \frac{K\Delta U^+_{MAX}}{2} \quad (7)$$

With the inner log-law and outer-wake equation combined in this fashion, equation (4) has been used to develop the measured profile comparisons shown on the right side of figures 52(a) and 52(b). In these comparisons, only those profiles representative of an ordinary turbulent boundary-layer under the influence of an adverse pressure gradient (main-element, upper-surface) have been used. On the left side of the figures, comparisons are shown for the outer profile with calculations from equation normalized to the ratio form:

$$\frac{g(II, y/\delta)}{g(II, 1.0)} \quad (8)$$

The fit of the test results to the calculations are sensitive to the proper selection of boundary-layer height, δ , and the "Clauser-Plot" derivation of the skin-friction coefficient. These parameters, as well as the value of the parameter II are tabulated on the figures. From these comparisons along with the previously discussed "law-of-the-wall" results, it would be concluded that the measured velocity profiles are in good agreement with generally-accepted analytical descriptions of the turbulent profile and that the latter offers a valid description of the observed flow-field.

4.4.3 Velocity Distributions in the Wake

In the foregoing, effective use of the measured boundary-layer profiles for evaluating skin-friction via the "law-of-the-wall" was illustrated. Additional correlations may be performed with such profiles relative to the "law-of-the-wake" (Reference 31). Figure 53 defines the calculation procedure for comparing the shape of the measured wake profile to that calculated by the expression shown on the figure (Reference 33). A composite plot representing a number of typical profiles is given in figure 54 wherein figure 54(a) represents the correlation for the inner half-wake and figure 54(b) the outer. Wake profiles represented by these data points are comprised of those trailing the main-element, and laying above the flap, as well as those trailing downstream of the flap. The data scatter at either extremity of the two plots appears to be a consequence of either close proximity to the flap surface (main-element wake, inner half-wake) or close

proximity to the flap trailing-edge where localized wake deformations are clearly shown in the LV-profiles; these would not be expected to closely conform to the wake law. Except for such points, the "law-of-the-wake" is generally satisfied by the LV-measurements.

5.0 CONCLUSIONS

The experimental development of the separating confluent boundary-layer data-base has required extensive use of the Lockheed-Georgia LV-system as basic test instrumentation. It is believed that this system represents, at least, state-of-the-art technology and excellent overall data production capabilities. The experience gained with this specific test-instrument on the subject program has provided valuable perspective on its inherent adaptability and potential as the complete experimental tool and gives focus to on-going LV-development work. It is worthwhile, therefore, that the concluding remarks, summarizing the major findings under the present program, include some reference to those areas where additional LV-development work could prove beneficial to studies of the type reported on herein.

LV-SYSTEM

- o The LV-system employed in the study proved to be fast, and reliable, providing non-intrusive test data unavailable from any other single source. It was found to be ideally suited to the study of high-lift systems where restrictive geometries, widely-varying flow conditions and flow-orientations are the general rule.
- o A "rapid-scan" LV-analog device proved to be an invaluable, time-saving aid to pinpointing significant flow-regions on the

airfoil before more time-consuming LV-digital measurements were attempted.

- o Results to-date indicate that monodispersed oil-based smoke particles of about (1) micron size were adequate for most LV-surveys. Conditions were noted (curvilinear flows, extensive separation) where difficulty was experienced in "seeding" the flow such that a high LV-data rate was maintained for all test conditions.
- o Exceptional cases, evidencing strongly time-dependent flow behavior, were identified by repeated LV-measurements. Such cases highlight the need for conditional-sampling studies in high-lift experimental development work.
- o Areas where additional LV-development work is needed include:
 - o Effects of particle-size on LV-measurements in regions characterized by high-speed, curvilinear flow and extensive surface separation.
 - o New, improved substances for LV-seeding to avoid oil-contamination of models, instrumentation and viewing windows.
 - o Improvement in the current turbulence interaction off-set of ≈ 0.6 fps at the lower turbulence levels.

- o Additional study of the response characteristics of various conventional instruments relative to LV-measurements such that valid comparative data can be extracted from each.

TEST FACILITY/MODEL

- o Preliminary studies of the test-facility indicated that the ERF provided essentially two-dimensional flow which was repeatable through model stall.
- o Basic GAW-1 model performance was found to be generally consistent with earlier documented results when accounting for significant differences in the test Reynolds numbers.
- o The NASA General Aviation airfoil, GAW-1, exhibited very stable aerodynamic performance and repeatable boundary-layer characteristics at the test Reynolds numbers; experimental results were found to be generally consistent with other documented test data.
- o Transition was found to occur naturally on all GAW-1 configurations at $x/c \approx 0.05$ on the upper-surface and ahead of the slot-cove area on the lower surfaces; stall characteristics reflected a turbulent trailing-edge separation on the main-element.

BOUNDARY-LAYER DATA CORRELATIONS

- o From a limited number of correlation studies, velocity profiles acquired by the LV-system were in basic agreement with those obtained from a traversing pitot-static probe.
- o Comparison of measurements taken with the LV-system and standard pitot-static probes over a wide-range of flow conditions indicated the LV to be superior in terms of its non-sensitivity to flow-angularity, reverse flow-fields and the accuracy of spatial positioning.
- o Initial comparisons of LV- and hot-wire turbulence measurements in the GAW-1 boundary-layer showed discrepancies as high as 40 percent whereas corresponding measurements in the airfoil wake gave good agreement.
- o Detailed studies of turbulence measurements by variable-geometry hot wires and the LV under controlled test conditions showed that the hot-wire could be subject to errors in spatial resolution, as a function of turbulent length-scale, and that the LV provided the more reliable and consistent turbulence data.
- o Based upon a limited number of data correlations, the "law-of-the-wall" and "law-of-the-wake" appear to produce valid descriptions of the observed flow-fields.

- o For a given attached-flow configuration and the same pressure distribution, ordinary boundary-layer parameters derived from LV-measured velocity profiles were in essential agreement with those determined theoretically in the NASA Multiple Airfoil Program.
- o For fully-attached flow conditions and for the same pressure distributions on the slat and main-element, confluent boundary-layer parameters derived from the LV-profiles on the main-element upper-surface, compared favorably with those obtained from the Multiple-Airfoil Program.
- o Evaluations via Clauser plots of local surface-friction from LV-measured velocity profiles agreed with Preston-tube measurements within anticipated levels of accuracy.

6.0 REFERENCES

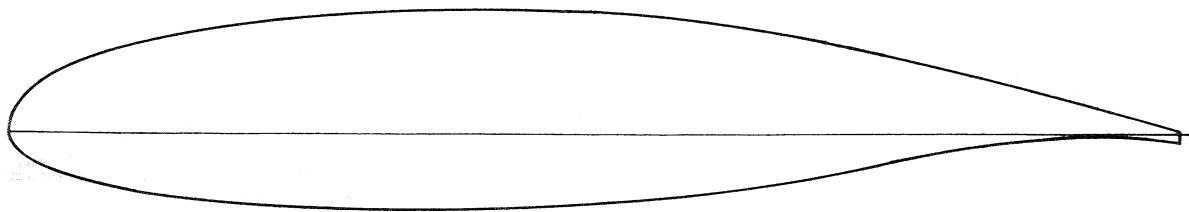
1. Bradshaw, P., Cebeci, T., and Whitelaw, J. H., "Engineering for Turbulent Flow," Academic Press, 1981.
2. Catherall, D., and Mangler, K. W., "The Integration of the Two-Dimensional Boundary Layer Equations Past the Point of Vanishing Skin Friction," J. Fluid Mechanics (1966), Vol. 16, Part 1.
3. Carter, J. E., "Solutions for Laminar Boundary Layers with Separation and Reattachment," AIAA Paper No. 74-583, 1974.
4. Cebeci, T., "Separating Boundary Layer Flow Calculations," J. of Comp. Phy. V. 31, 1979.
5. Horton, H. P., "Comparisons Between Inverse Boundary Layer Calculations and Detailed Measurements in Laminar Separated Flows," The Aeronautical Quarterly, V. 32, Part 3, 1981.
6. Whitfield, D. L., Swafford, T. W., and Jacocks, J. L., "Calculation of Turbulent Boundary Layers with Separation and Viscous-Inviscid Interaction," AIAA Journal, V. 19, No. 10, 1981.
7. Carter, J. E., "Viscous-Inviscid Interaction Analysis of Transonic Turbulent Separated Flow," AIAA Paper 81-1241, 1981.

8. Maskew, B., and Dvorak, F. A., "Investigation of Separation Models for the Prediction of CLMAX," 33rd Annual National Forum of the American Helicopter Society, Paper No. 77.33-01, Washington, D.C., 1977.
9. Henderson, M. I., "A Solution of the 2-D Separated Wake Modeling Problem and Its Use to Predict CLMAX of Arbitrary Airfoil Sections," AIAA 16th Aerospace Sciences Meeting, Paper No. 78-156, Huntsville, Alabama, Jan. 16-18, 1978.
10. Gilmer, B. R., and Bristow, D. R., "Analysis of Stalled Airfoils by Simultaneous Perturbations to Viscous and Inviscid Equations," AIAA 14th Fluid and Plasma Dynamics Conference, Paper No. 81-1239, Palo Alto, CA, June 1981.
11. Tassa, Y., "Computation of Flow 8621," Stanford Conference on Complex Turbulent Flows, 1981.
12. Tassa, Y. and Sankar, N. L., "Dynamic Stall of an Oscillating Airfoil in Turbulent Flow Using Time Dependent Navier-Stokes Solver," IUTAM Symposium on Unsteady Turbulent Shear Flow, 1981.
13. Tassa, Y. and Sankar, N. L., "Dynamic Stall of NACA 0012 Airfoil in Turbulent Flow-Numerical Study," AIAA Paper 81-1289, June 1981.

14. Stevens, W. A., Goradia, S.H. and Braden, J. A., "Mathematical Model for Two-Dimensional Multi-Component Airfoils in Viscous Flow," NASA CR-1843, 1971.
15. Thomas, P. D., and Middlecoff, J. F., "Direct Control of the Grid Point Distribution in Meshes Generated by Elliptic Equations," AIAA Journal, Vol. 18, No. 6, 1980.
16. Whiffen, M. C., and Meadows, D. M., "Two Axis, Single Particle Laser Velocimeter System for Turbulence Spectral Analysis." Proceedings of the Second International Workshop on Laser Velocimetry, Volume I, H.D. Thompson and W.H. Stevenson, eds., Eng. Exp. Stn. Bull. No. 144, Purdue Univ., 1974, pp. 1-15.
17. Whiffen, M. C., "Polar Response of an LV Measurement Volume," Minnesota Symposium on Laser Anemometry, University of Minnesota, Oct. 22-24, 1975.
18. Morris, P.J. and Whiffen, M. C., "The Characteristics and Applications of a Two-Axis Laser Velocimeter," Proceedings of the Lockheed-Georgia Viscous Flow Symposium, pp. 197-237, June 1976.
19. Lau, J. C. and Whiffen, M. C., "A Note on Turbulence Measurements with a Laser Velocimeter," Journal of Fluid Mechanics, Vol. 102, pp. 353-366, 1981.
20. "Flow visualization and Laser Velocimetry for Wind Tunnels," NASA Conference Publication 2243, compilation of papers presented at NASA-Langley Research Center Workshop, March 25-26, 1982.

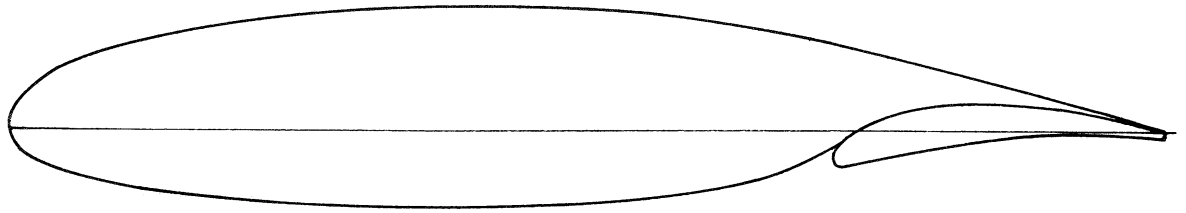
21. Orloff, K. L. and Olson, L. E., "High-Resolution LDA Measurements of Reynolds Stress in Boundary Layers and Wakes." A Collection of Technical Papers - AIAA 11th Aerodynamic Testing Conference, Mar. 1980, pp. 363-374. (Available as AIAA-80-0436.)
22. Clauser, F. H., "Turbulent Boundary-Layers in Adverse Pressure Gradients," Journal Aero. Sci., Vol. 21, No. 2, Feb. 1954.
23. Wentz, W. H., Jr. and Seetharam, H. C., "Development of a Fowler Flap System for a High Performance General Aviation Airfoil," NASA CR-2443, 1974.
24. Ower, E. and Pankhurst, R. C., "The Measurement of Airflow," Pergamon Press, 4th Edition, 1966.
25. Karpuk, M. E. and Tiederman, W. G., Jr., "Effect of Finite-Size Probe Volume upon Laser Doppler Anemometer Measurements," AIAA Journal, Vol. 14, No. 8, pp. 1099-1105, August 1976.
26. McGhee, R. J. and Beasley, W. D., Low-Speed Aerodynamic Characteristics of a 17-Percent-Thick Airfoil Section Designed for General Aviation Applications. NASA TN-D-7428, 1973.
27. Meyers, J. F., Wilkenson, S. P., A Comparison of Turbulence Measurements Using a Laser Velocimeter and a Hot Wire in a Low Speed Jet Flow. International Symposium on Applications of Laser-Doppler Anemometry to Fluid Mechanics, Lisbon, Portugal, July 1982.

28. Sandborn, V. A., Resistance Temperature Transducer, Metrology Press, 1972.
29. Bearman, P. W., Corrections for the Effect of Ambient Temperature Drift on Hot-Wire Measurements in Incompressible Flow. DISA Information No. 11, May 1971.
30. Batchelor, G. K., The Theory of Homogeneous Turbulence. Cambridge Monographs on Mechanics and Applied Mathematics, 1960.
31. White, Frank M., "Viscous Fluid Flow," McGraw-Hill Book Company, 1974.
32. Dean, R. B., "A Single Formula for the Complete Velocity Profile in a Turbulent Boundary-Layer," ASME Journal of Fluids Engineering, Vol. 98, No. 4, Dec. 1976.
33. Bario, F., Chasnay, G. and Papailion, K. D., "An Experiment Concerning the Confluence of a Wake and a Boundary Layer," Transactions of the ASME, Vol. 104, pp. 18-23, March 1982.



Upper Surface		Lower Surface	
X / c	Z / c	X / c	Z / c
0.00000	0.00000	0.00000	0.00000
.00200	.01300	.00200	-.00930
.00500	.02040	.00500	-.01380
.01250	.03070	.01250	-.02050
.22500	.04170	.02500	-.02690
.03750	.04965	.03750	-.03190
.05000	.05589	.05000	-.03580
.07500	.06551	.07500	-.04210
.10000	.07300	.10000	-.04700
.12500	.07900	.12500	-.05100
.15000	.08400	.15000	-.05430
.17500	.08840	.17500	-.05700
.20000	.09200	.20000	-.05930
.25000	.09770	.25000	-.06270
.30000	.10160	.30000	-.06450
.35000	.10400	.35000	-.06520
.40000	.10491	.40000	-.06490
.45000	.10445	.45000	-.06350
.50000	.10258	.50000	-.06100
.55000	.09910	.55000	-.05700
.57500	.09668	.57500	-.05400
.60000	.09371	.60000	-.05080
.62500	.09006	.62500	-.04690
.65000	.08599	.65000	-.04280
.67500	.08136	.67500	-.03840
.70000	.07634	.70000	-.03400
.72500	.07092	.72500	-.02940
.75000	.06513	.75000	-.02490
.77500	.05907	.77500	-.02040
.80000	.05286	.80000	-.01600
.82500	.04646	.82500	-.01200
.85000	.03988	.85000	-.00860
.87500	.03315	.87500	-.00580
.90000	.02639	.90000	-.00360
.92500	.01961	.92500	-.00250
.95000	.01287	.95000	-.00260
.97500	.00609	.97500	-.00400
1.00000	-.00070	1.00000	-.00800

TABLE I(a) - GAW-1 AIRFOIL COORDINATES



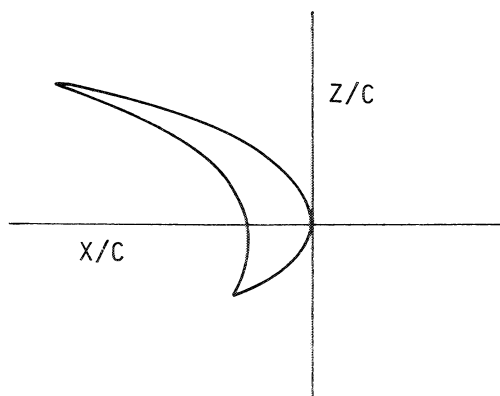
29% Fowler Flap Coordinates			
Upper Surface		Lower Surface	
x_f/c	z_f/c	x_f/c	z_f/c
0.00000	-.02350	0.00000	-.02350
.00030	-.02000	.00100	-.02700
.00200	-.01790	.00200	-.02880
.00400	-.01550	.00400	-.03000
.00800	-.01130	.00800	-.03100
.01200	-.00780	.01200	-.03040
.01800	-.00330	.02000	-.02880
.02300	.00000	.03000	-.02700
.02800	.00230	.05000	-.02350
.03800	.00700	.07000	-.01980
.04800	.01100	.09000	-.01600
.05800	.01410	.11000	-.01300
.06800	.01680	.13000	-.01000
.07800	.01900	.15000	-.00770
.08800	.02070	.17000	-.00580
.09800	.02180	.19000	-.00360
.10800	.02230	.21000	-.00270
.11800	.02280	.23000	-.00280
.12800	.02300	.25000	-.00350
.13800	.02340	.27000	-.00500
.14800	.02280	.29000	-.00800
.15800	.02230		
.16800	.02190		
.19000	.01980		
.21000	.01680		
.23000	.01380		
.25000	.00980		
.27000	.00590		
.29000	-.00070		

Nose Radius = .0075C

Nose Radius Location ($x_f/c, z_f/c$) = (.0075, -.0235)

TABLE I(b) - 29% C FOWLER FLAP CONFIGURATION

<u>Upper Surface</u>		<u>Lower Surface</u>	
X / c	Z / c	X / c	Z / c
0.00000	0.00000	0.00000	0.00000
.02000	.01300	.00200	-.00930
.00500	.02040	.00500	-.01380
.01250	.03070	.01250	-.02050
.02500	.04170	.02500	-.02690
.03750	.04965	.03750	-.03190
.05000	.05589	.04500	-.03440
.07500	.06551		
.10000	.07300		
.12500	.07900		
.14000	.08210		
.15000	.08400		



<u>Cove Region</u>	
X / c	Z / c
.04000	-.01600
.03900	.00000
.04500	.01850
.06000	.03800
.08000	.05510
.10000	.06640
.12000	.07500
.14000	.08110
.15000	.08350

TABLE II. - 15 PERCENT CHORD LEADING-EDGE SLAT COORDINATES

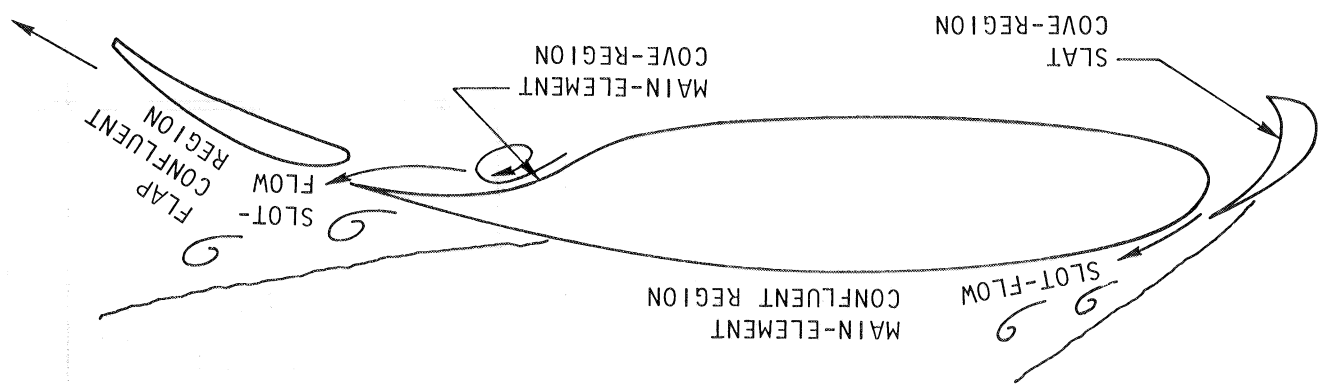


FIGURE 1 REGIONS EXHIBITING CONFLUENT BOUNDARY-LAYER FLOW ON HIGH-LIFT AIRFOIL.

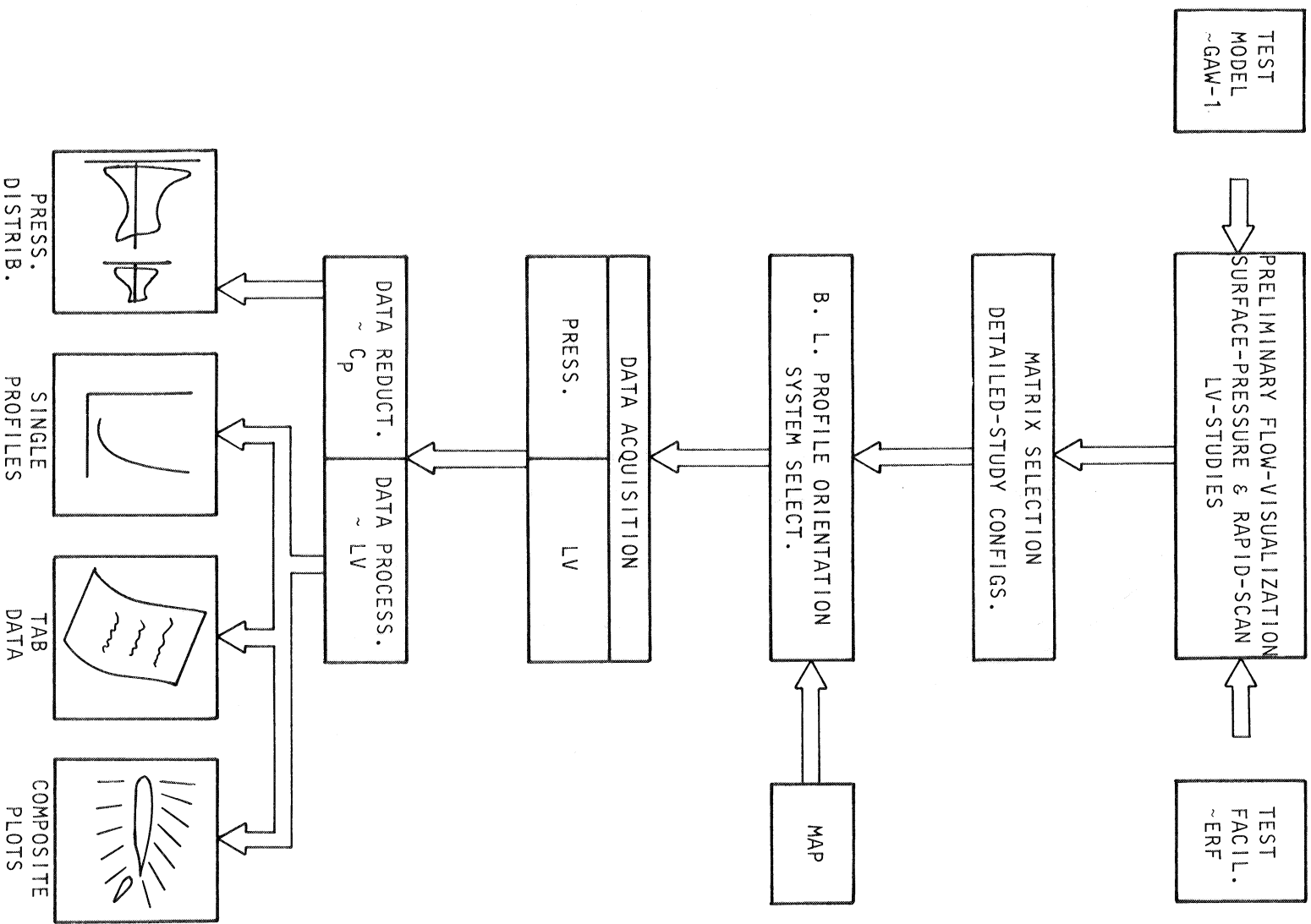


FIGURE 2 APPROACH TO CONFLUENT BOUNDARY-LAYER EXPERIMENTAL STUDY

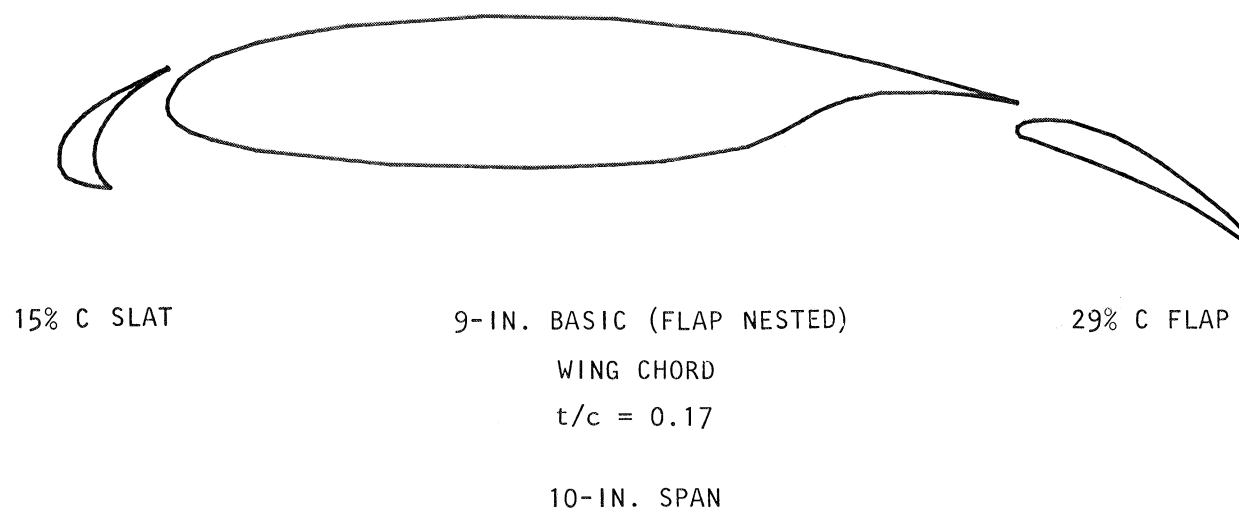


FIGURE 3 GEOMETRIC ARRANGEMENT OF GAW-1 HIGH-LIFT AIRFOIL FOR
SEPARATING CONFLUENT BOUNDARY-LAYER TEST PROGRAM

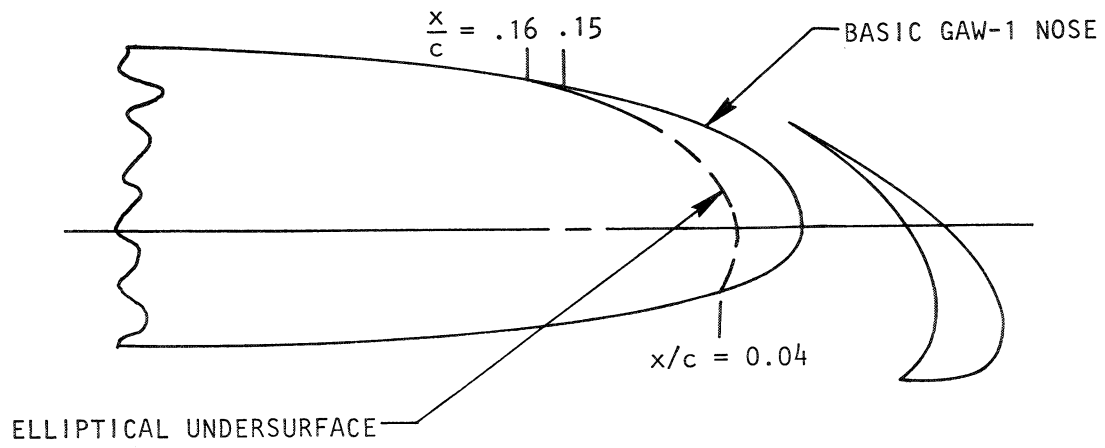


FIGURE 4 GAW-1 LEADING-EDGE SLAT DESIGN

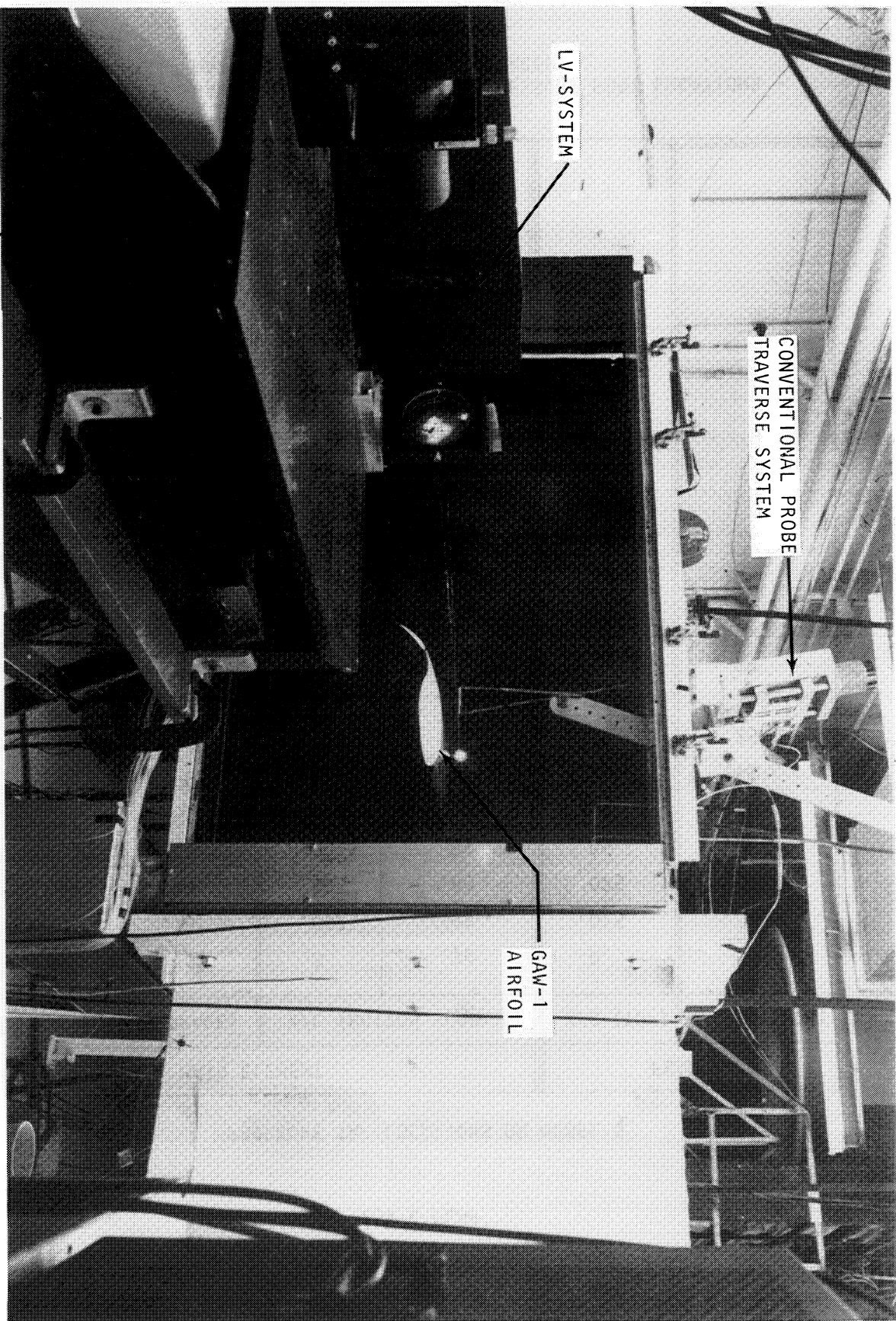


FIGURE 5 EXPERIMENTAL SET-UP FOR GAW-1 AIRFOIL IN ERF WIND TUNNEL

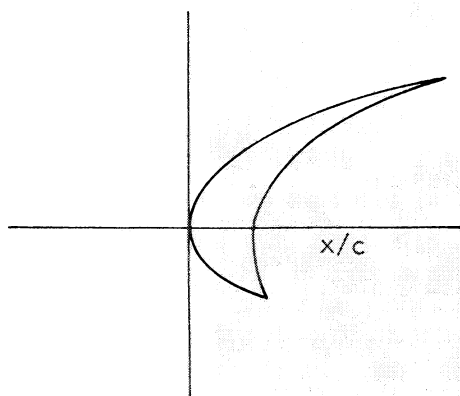
GAW-1 AIRFOIL

29% C FLAP

PRESSURE TAP LOCATIONS ON MODEL q_c

MAIN ELEMENT		FLAP	
X/C (TOP SURFACE)	X/C (BOTTOM SURFACE)	X/C (TOP)	X/C (BOTTOM)
0	.70	0	0
.0025	.75	.015	.015
.0050	.80	.025	.025
.0075	.85	.05	.05
.010	.90	.10	.10
.015	.925	.15	.15
.020	.95	.25	.25
.025		.275	.275
.050		.29	.29
.075			
.10			
.15			
.20			
.25			
.30			
.35			
.40			
.45			
.50			
.55			
.60			
.65			

TABLE III. GAW-1 CHORDWISE SURFACE PRESSURE PORT LOCATIONS -
MAIN ELEMENT AND FLAP SURFACES



TOP SURFACE	BOTTOM SURFACE
x/c	x/c
0	.005
.0025	.020
.0050	.040
.0100	.036
.0200	.050
.040	.030
.060	.110
.100	.135
.140	

COVE

$C = 9-IN.$

TABLE IV. - GAW-1 CHORDWISE SURFACE PRESSURE PORT LOCATIONS -
SLAT SURFACES

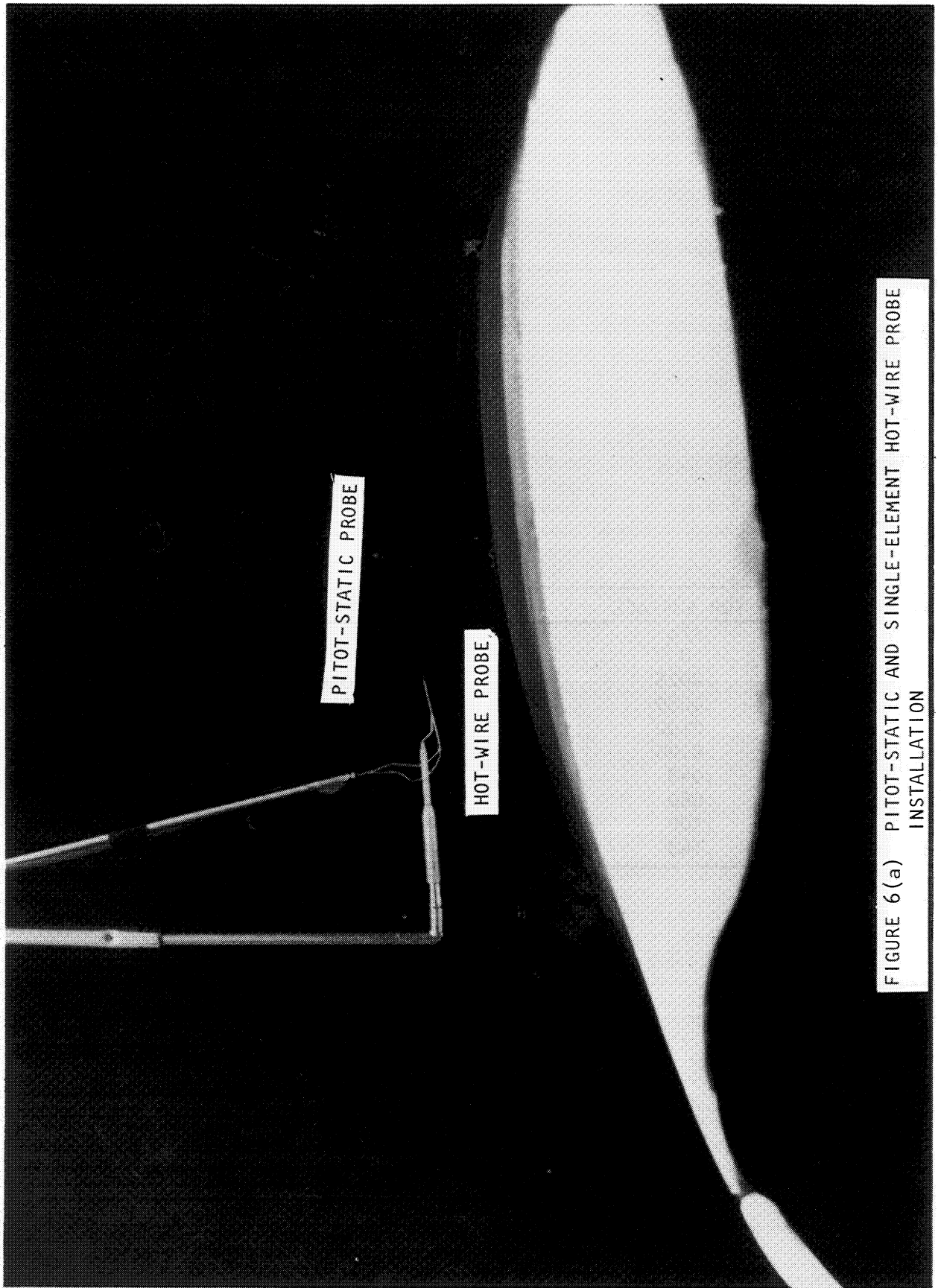


FIGURE 6(a) PITOT-STATIC AND SINGLE-ELEMENT HOT-WIRE PROBE INSTALLATION

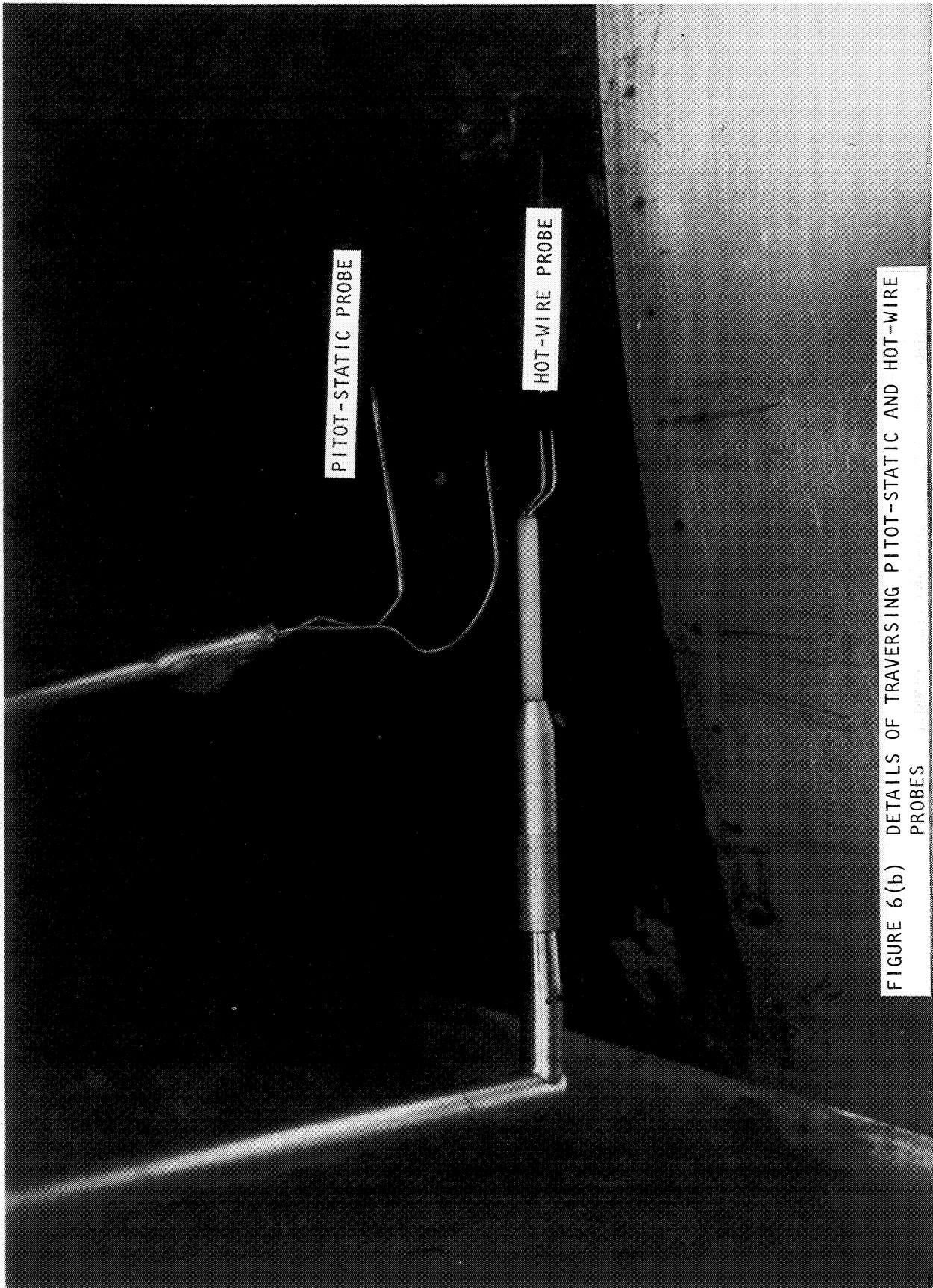


FIGURE 6(b) DETAILS OF TRAVERSING PITOT-STATIC AND HOT-WIRE PROBES

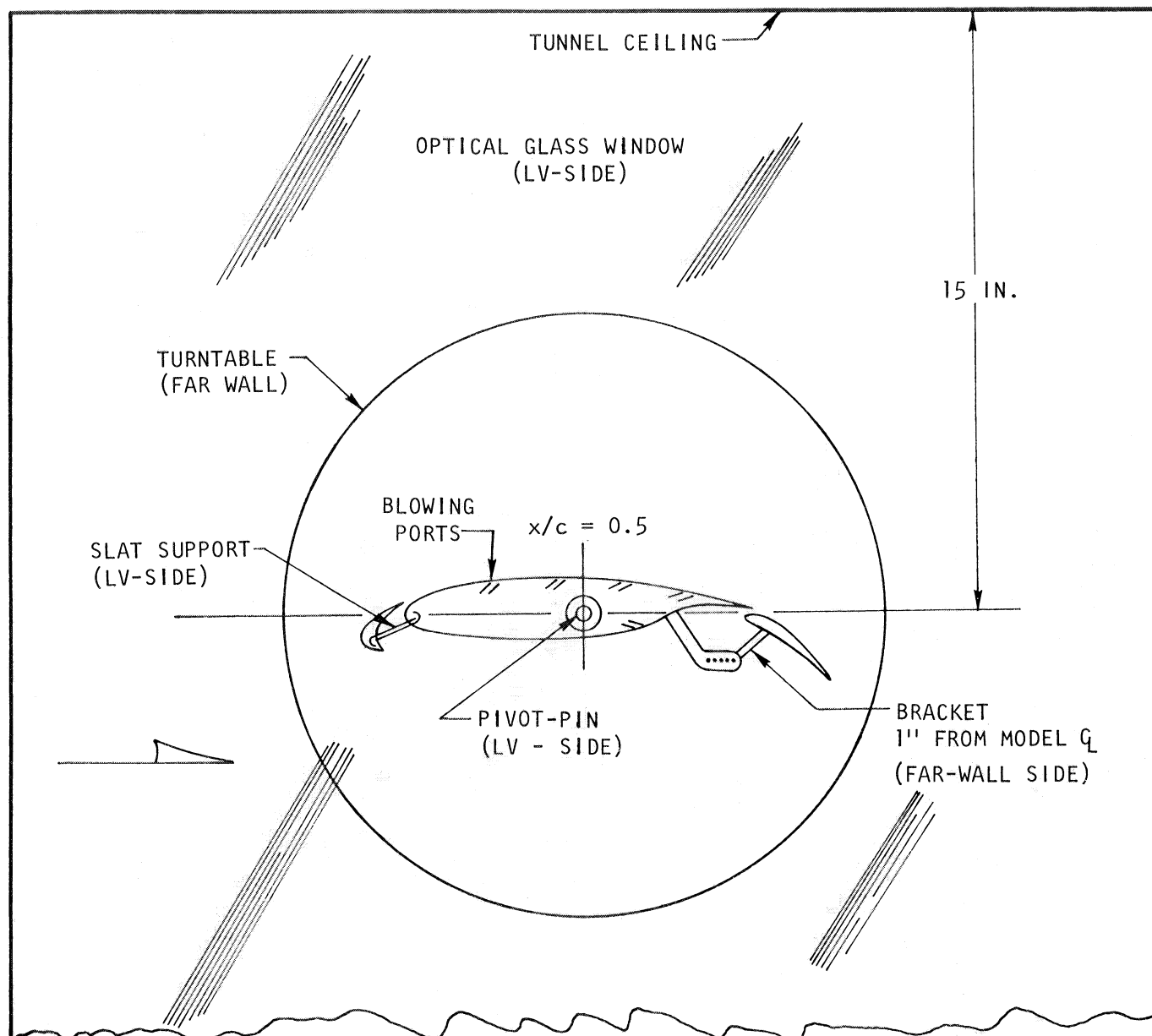
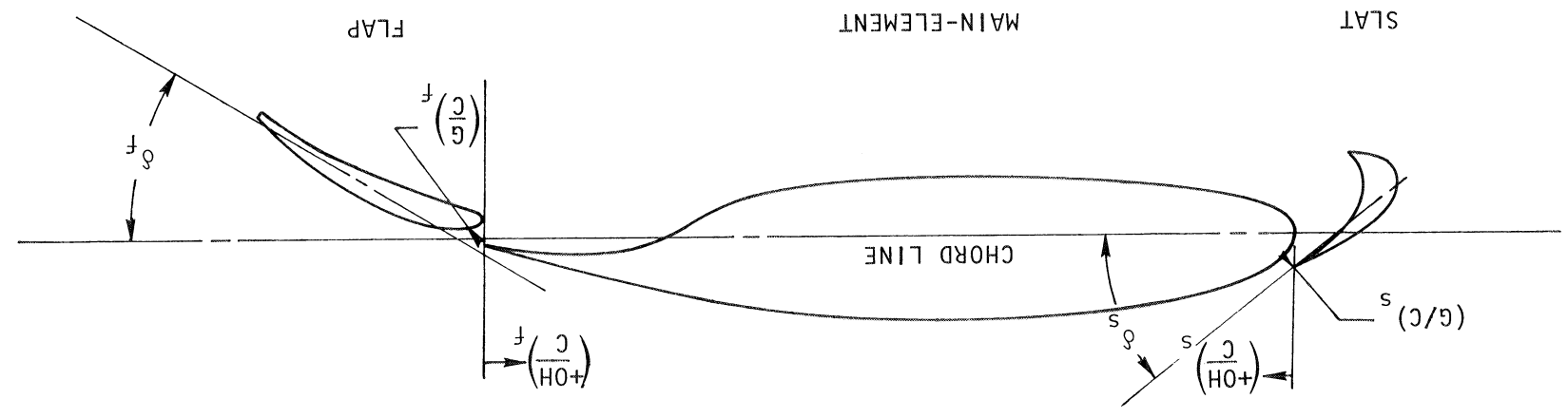


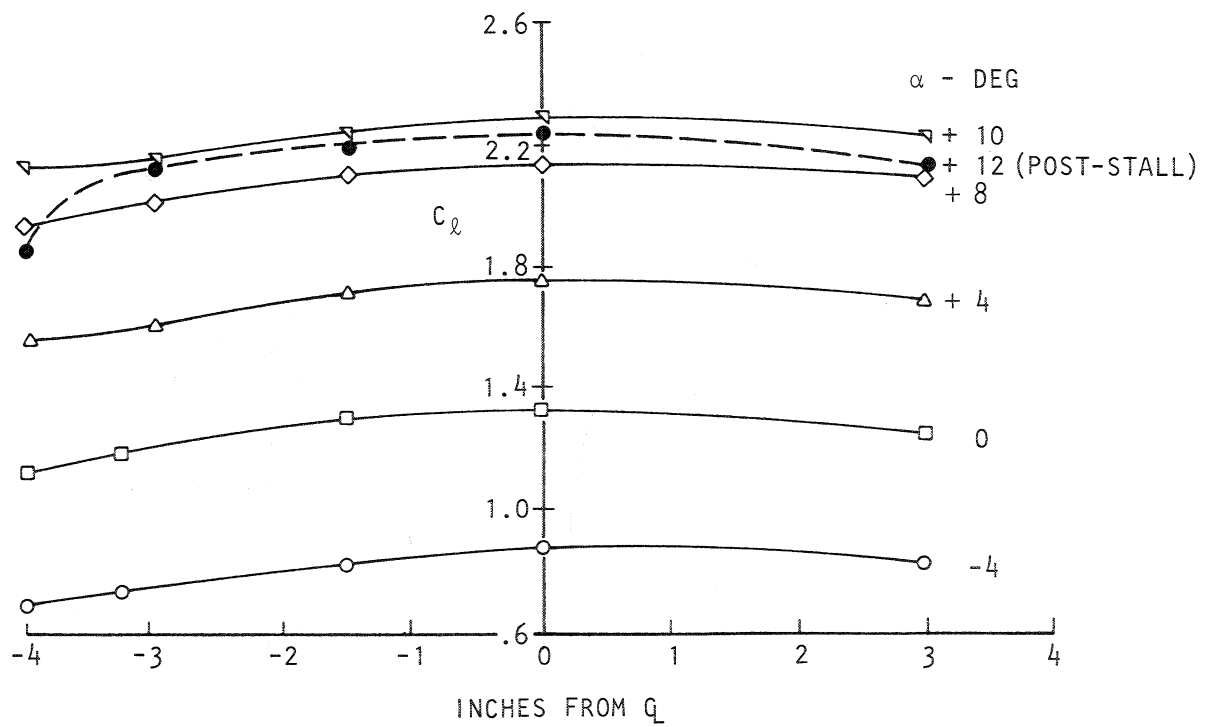
FIGURE 7. -GAW-1 MODEL INSTALLATION IN 10X30-INCH ERF WIND-TUNNEL

FIGURE 8 -DEFINITION OF GEOMETRIC PARAMETERS ON GAW-1 HIGH-LIFT AIRFOIL

FLAP	.015 - .04	-.025	0 → 40
SLAT	.01 - .03	±.015	25 → 55
	G/C	OH/C	δ^c

AVAILABLE RANGE OF VARIABLES





11-INCH CHORD HIGH-LIFT MODEL
TWO-DIMENSIONAL FLOW STUDY
 $\delta_f = 30^\circ$

FIGURE 9 ERF FLOW TWO-DIMENSIONALITY WITHOUT SIDEWALL BLOWING

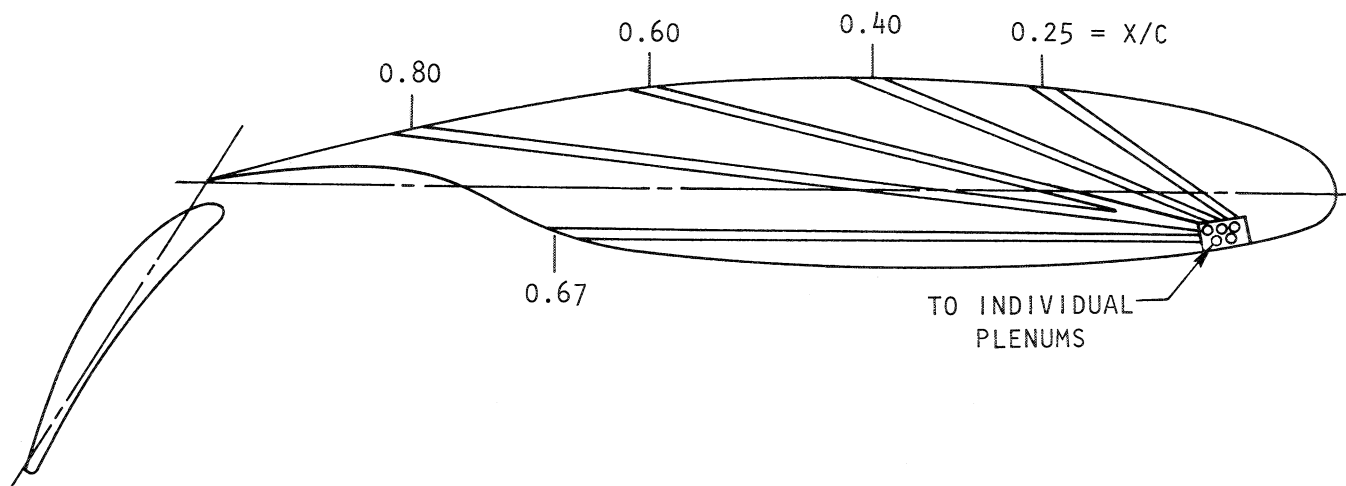


FIGURE 10 SIDEWALL BLOWING SCHEME FOR GAW-1 CONFLUENT
BOUNDARY LAYER STUDY

GAW - 1
 $\alpha = 10.0^\circ$
 $X/C = 0.94$

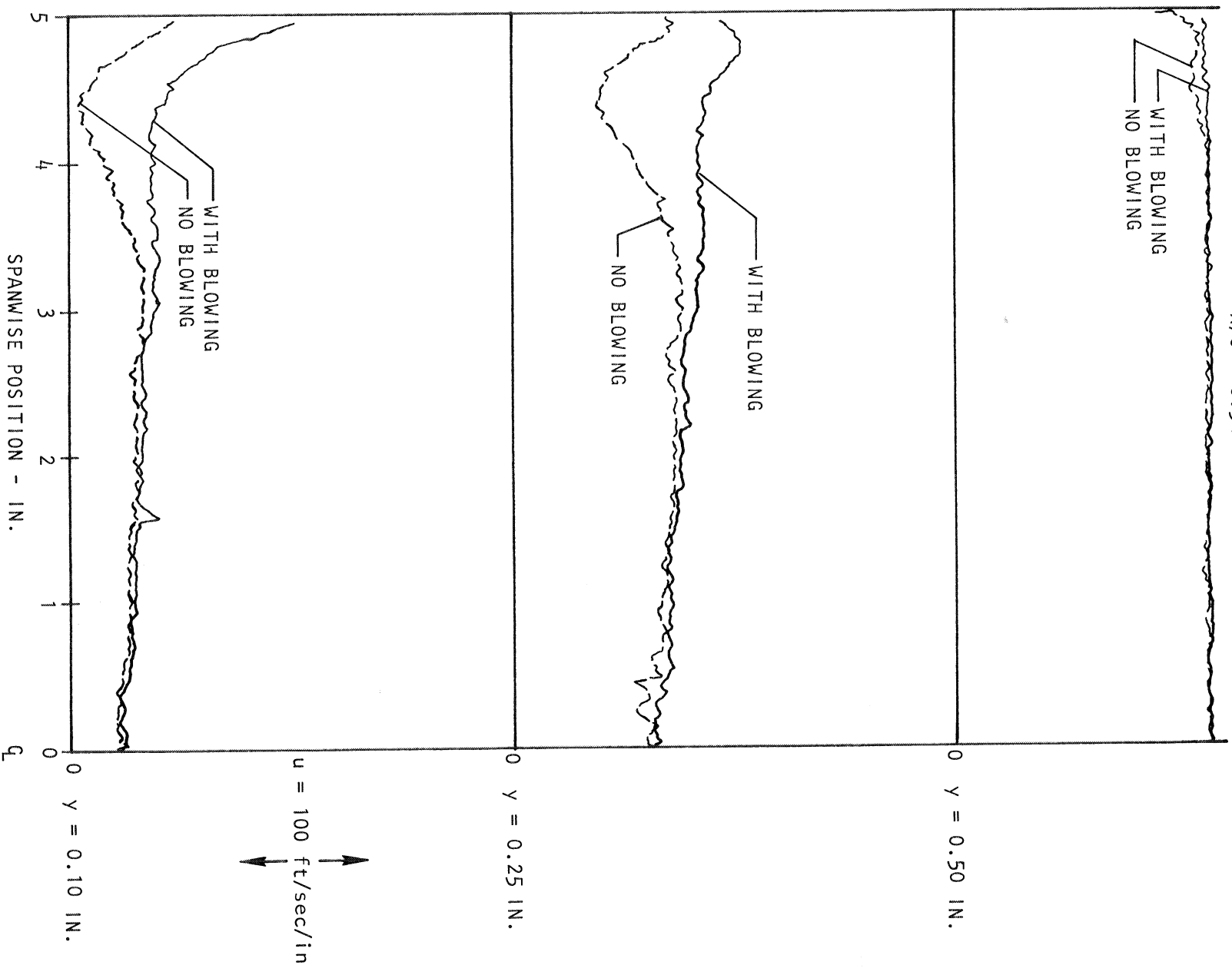


FIGURE 11 APPLICATION OF RAPID-TRAVERSE LV ANALOG SYSTEM
 FOR FLOW TWO-DIMENSIONALITY EVALUATION

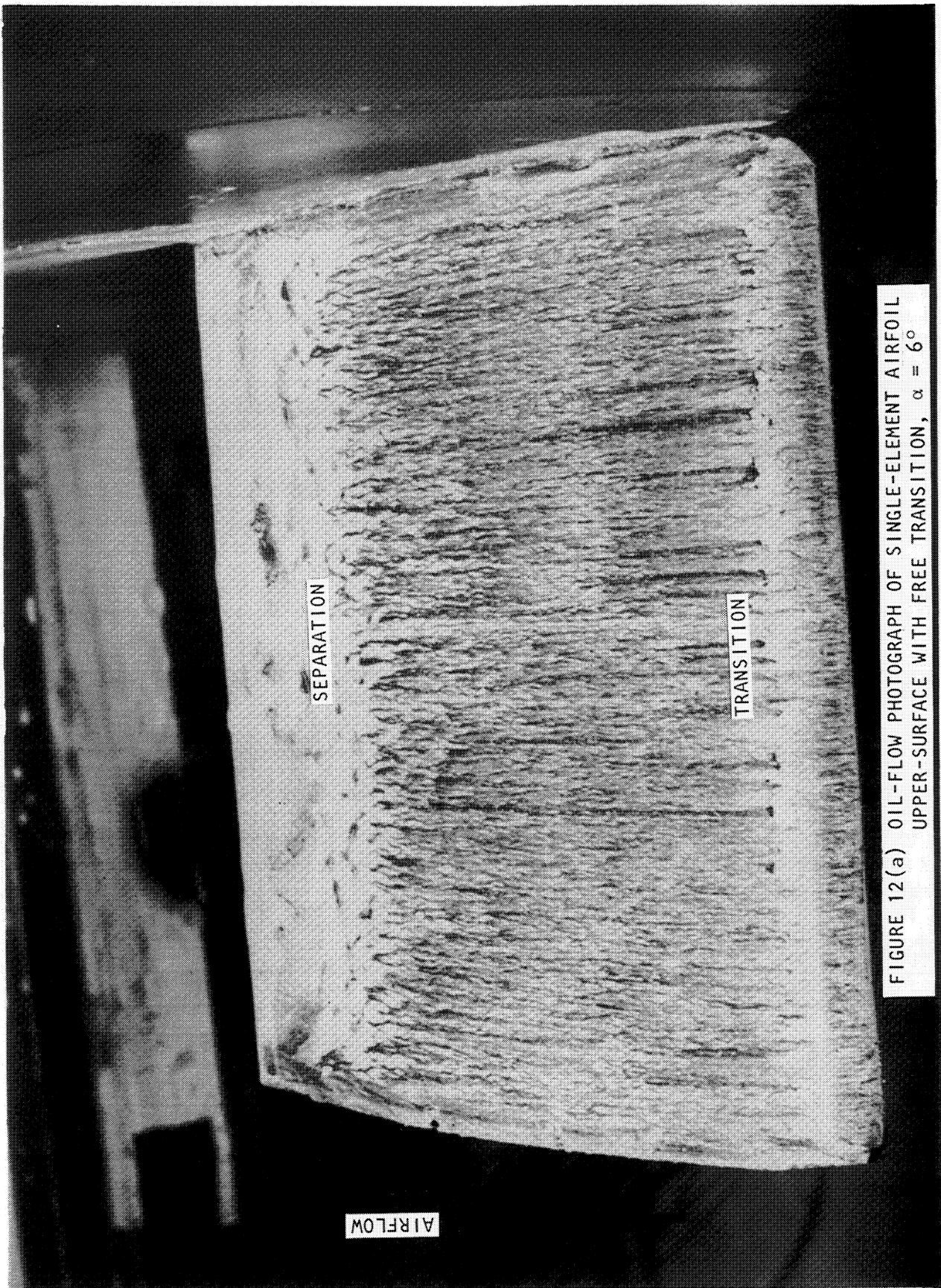


FIGURE 12(a) OIL-FLOW PHOTOGRAPH OF SINGLE-ELEMENT AIRFOIL
UPPER-SURFACE WITH FREE TRANSITION, $\alpha = 6^\circ$

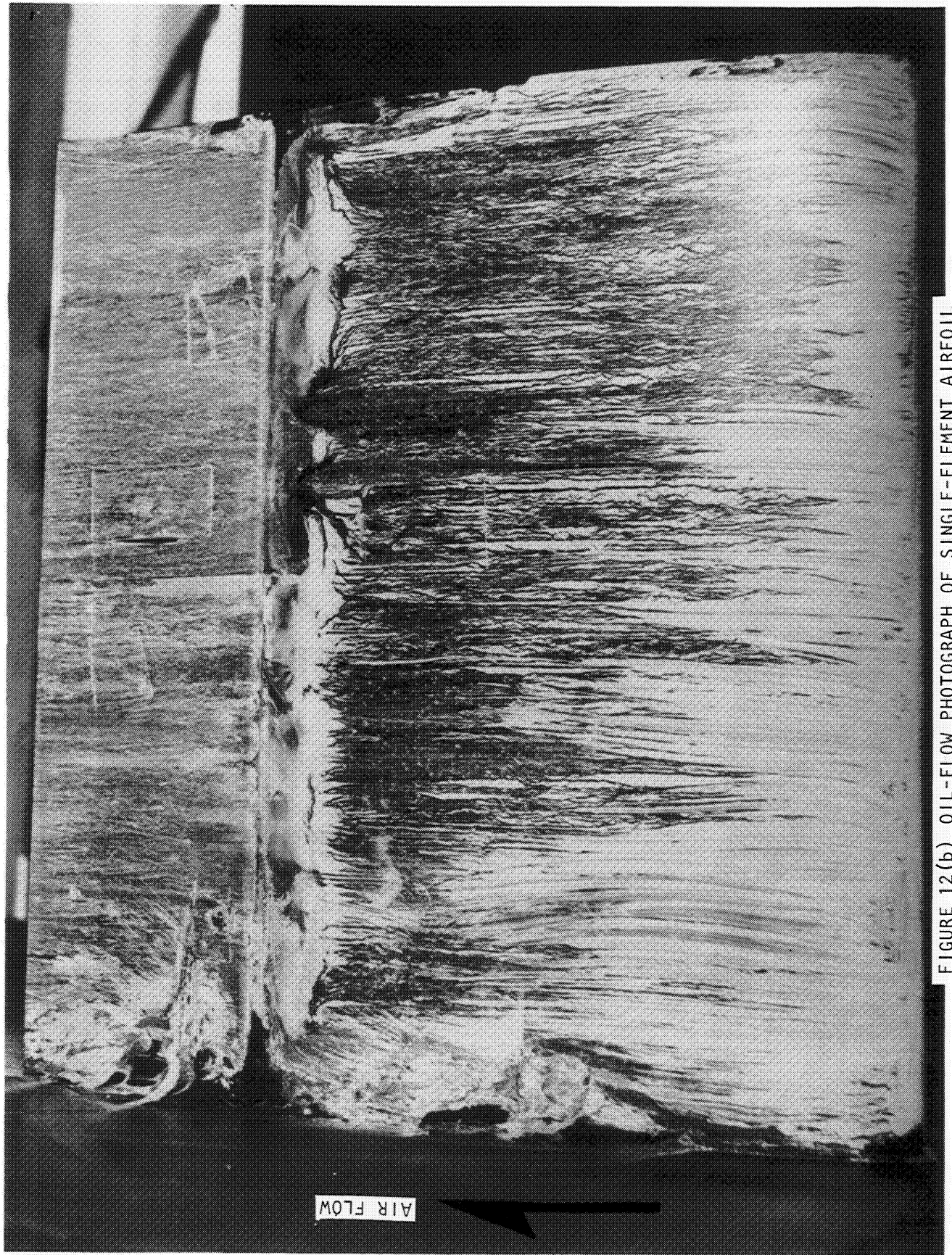



















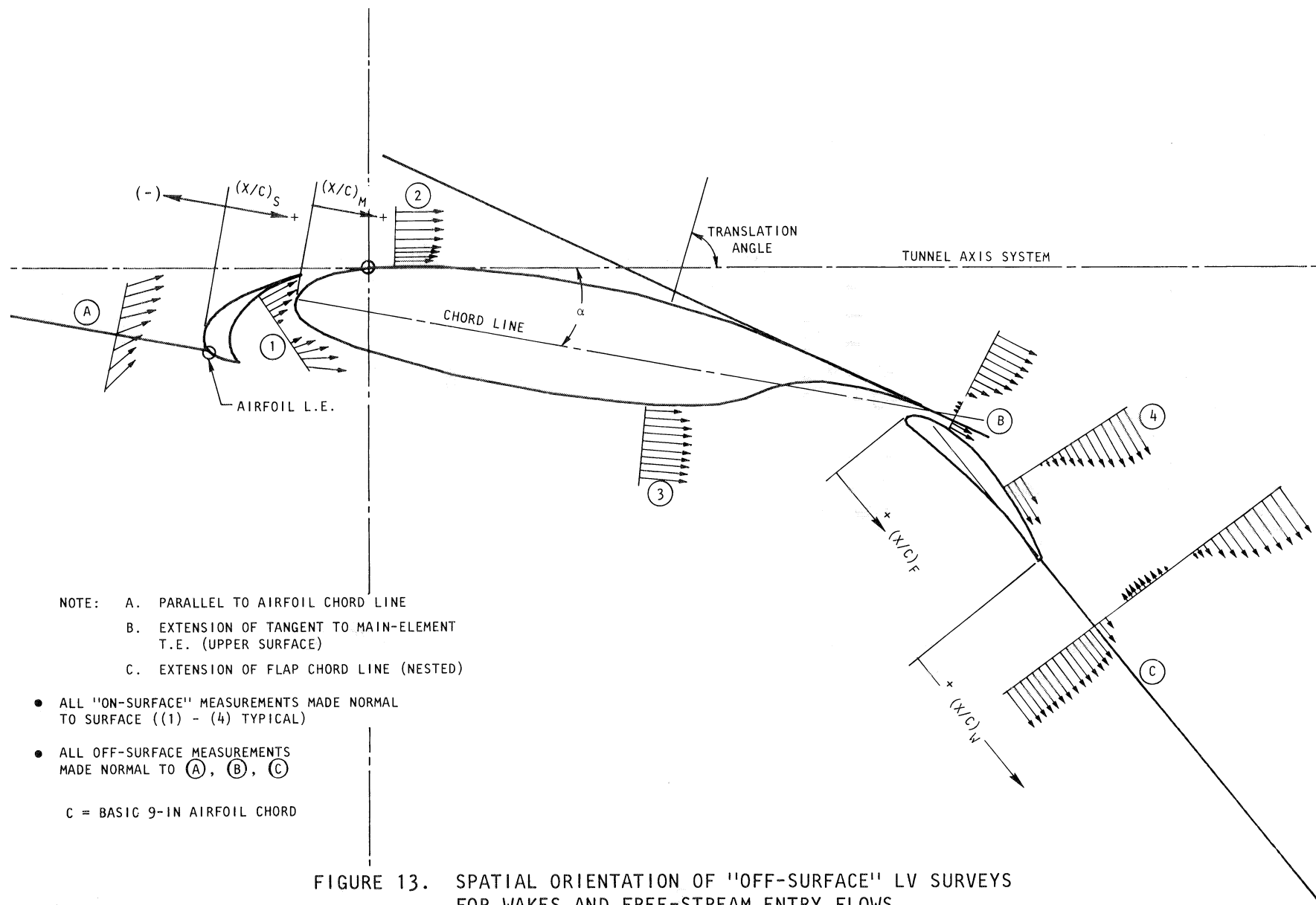


FIGURE 12 (b) OIL-FLOW PHOTOGRAPH OF SINGLE-ELEMENT AIRFOIL
LOWER-SURFACE WITH FREE TRANSITION, $\alpha = 6^\circ$

TABLE V. - CONFIGURATION MATRIX SELECTED FOR DETAILED LV-FLOW SURVEYS.

CONFIGURATION	1	2	3	4	5	6
A CLEAN AIRFOIL	$\alpha = 0^\circ$ 	$\alpha = 4.20^\circ$ 	$\alpha = 5.86^\circ$ 	$\alpha = 11.72^\circ$ 	$\alpha = 16.04^\circ$ 	
B FLAPPED $\delta_f = 30^\circ$	$(G/C)F=0.04$ (OH/C)F=0.0			$(G/C)F=0.025$ (OH/C)F=0.0		
	$\alpha = 3.98^\circ$ 	$\alpha = 7.94^\circ$ 	$\alpha = 11.95^\circ$ 	$\alpha = 4.13^\circ$ 	$\alpha = 12.23^\circ$ 	
C FLAPPED $\delta_f = 40^\circ$	$\alpha = 3.98^\circ$ 	$\alpha = 7.99^\circ$ 	$\alpha = 10^\circ$ 	$\alpha = 3.97^\circ$ 	$\alpha = 7.97^\circ$ 	$\alpha = 11.05^\circ$ 
	$(G/C)F=0.015$ (OH/C)F=0.025			$(G/C)F=0.015$ (OH/C)F=0.0		
D SLATTED $\delta_s = 27^\circ$	$\alpha = 17.90^\circ$ 	$\alpha = 21.48^\circ$ 	$\alpha = 23.03^\circ$ 	A-1 \rightarrow A-5	027	031-9
	$(G/C)S=0.023$ (OH/C)S=0.028			B-1 \rightarrow B-3	032	032-24
				B-4 \rightarrow B-6		032-25
E FLAPPED & SLATTED $\delta_s = 42^\circ$ $\delta_f = 30^\circ$	$(\frac{G}{C})S=0.015$ $(\frac{G}{OH})S=0.015$ $(\frac{G}{C})F=0.025$ $(\frac{G}{OH})F=0.0$			C-1 \rightarrow C-3		032-29
				C-4 \rightarrow C-6		032-65
				D-1 \rightarrow D-3		032-58
F FLAPPED & SLATTED $\delta_s = 42^\circ$ $\delta_f = 40^\circ$	$(\frac{G}{C})S=0.015$ $(\frac{G}{OH})S=0.015$ $(\frac{G}{C})F=0.025$ $(\frac{G}{OH})F=0.025$			E-1 \rightarrow E-3		032-40
				F-1 \rightarrow F-3		032-59

LV-TEST *
PRESS. TEST-RUN **



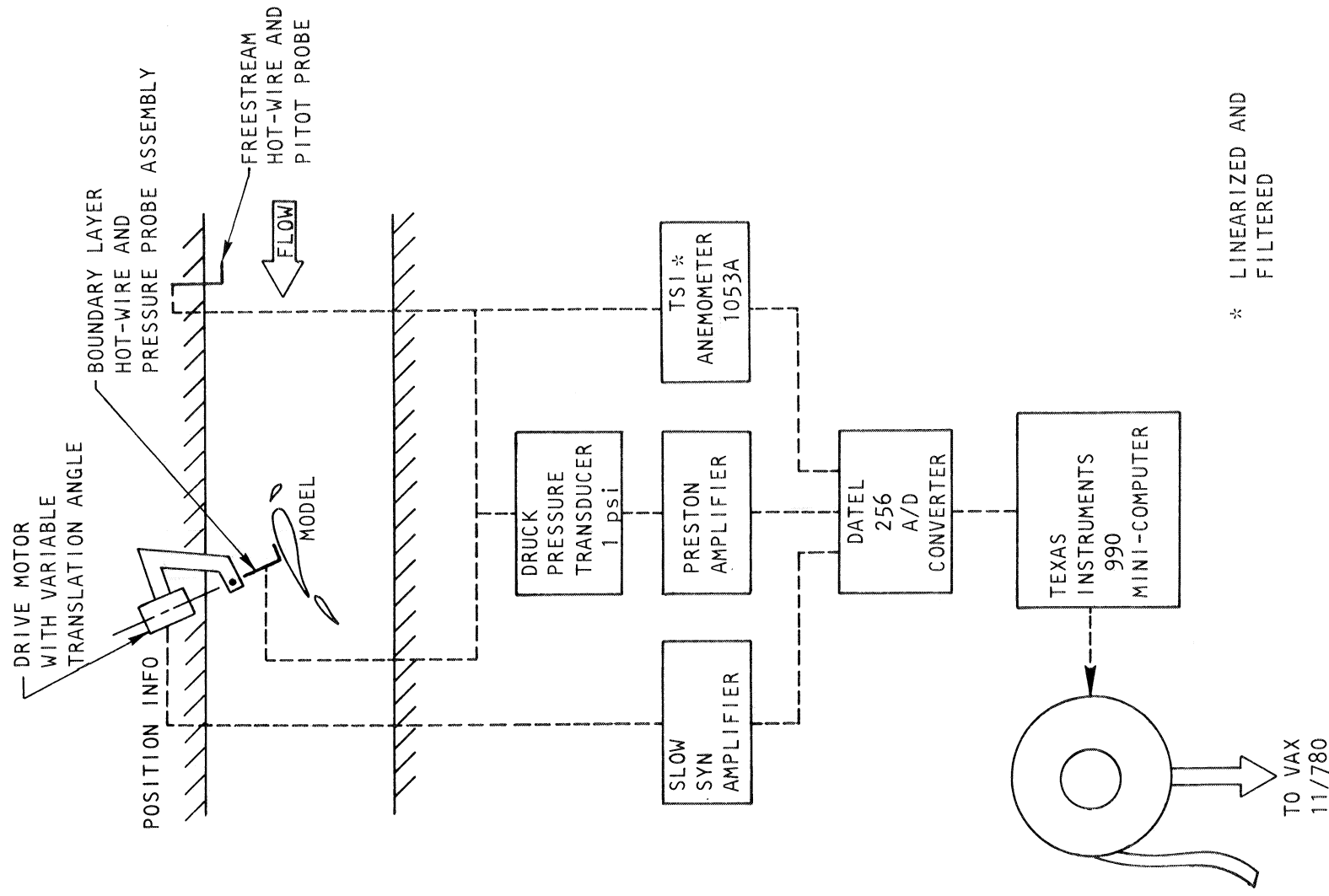


FIGURE 14 BLOCK DIAGRAM OF PITOT-STATIC AND HOT-WIRE DATA REDUCTION SYSTEMS

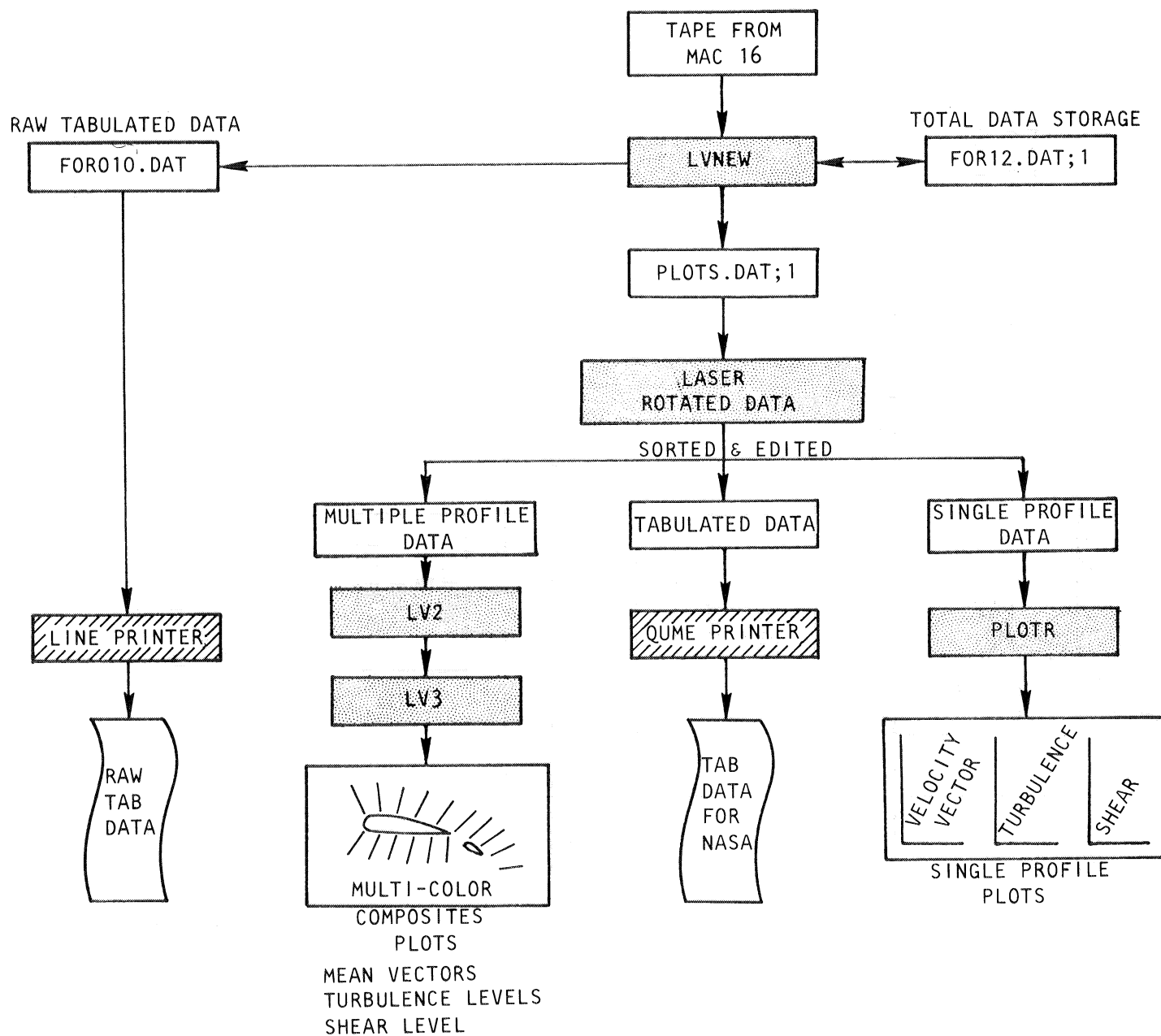


FIGURE 15

BLOCK DIAGRAM OF LASER VELOCIMETER DATA REDUCTION SYSTEM

ERF, $R_{NC} = 0.62 \times 10^6$, FREE TRANSITION
 WSU, $R_{NC} = 2.25 \times 10^6$, FORCE TESTS

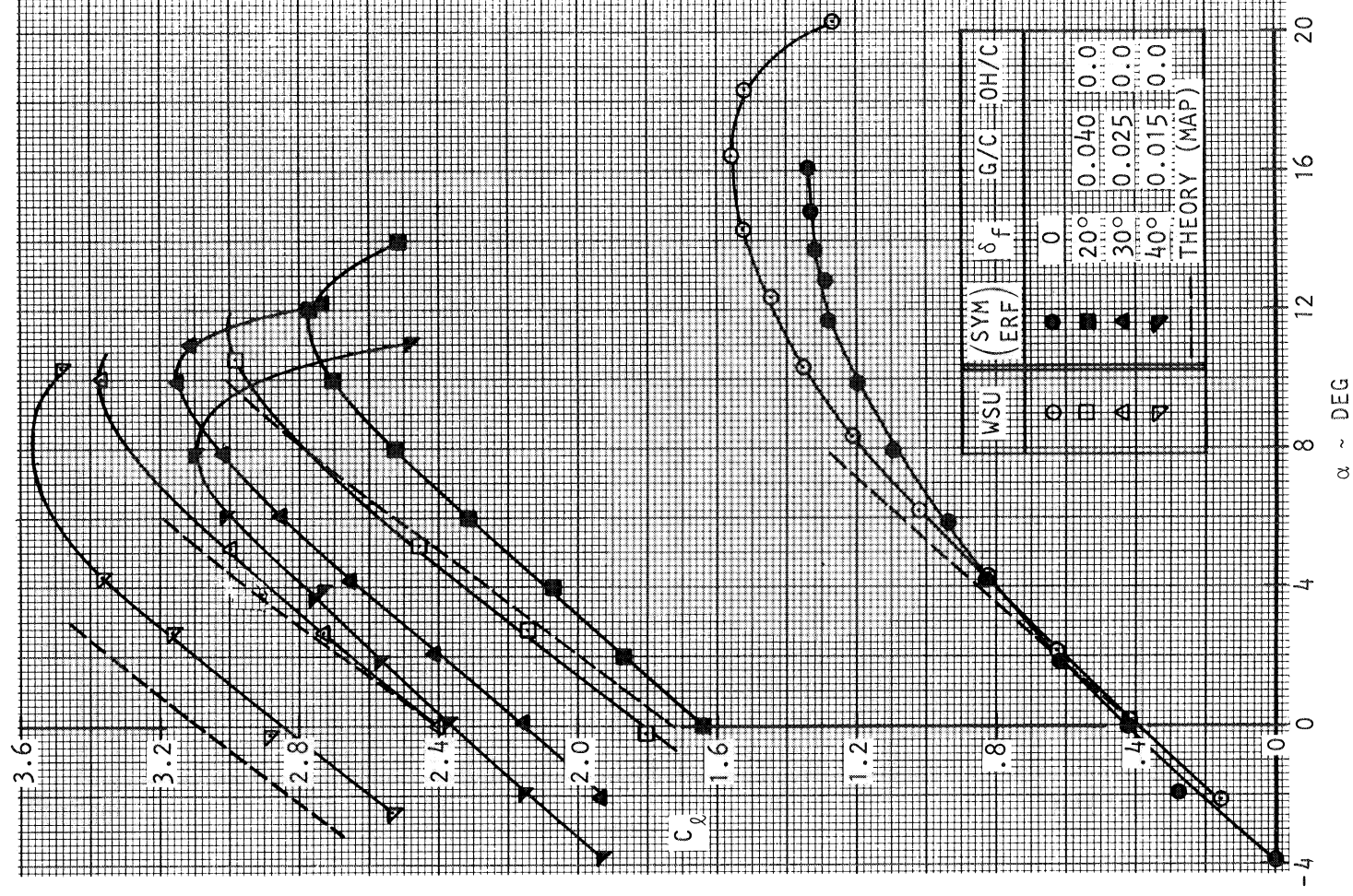


FIGURE 16 COMPARISON OF GAW-1 AIRFOIL PERFORMANCE

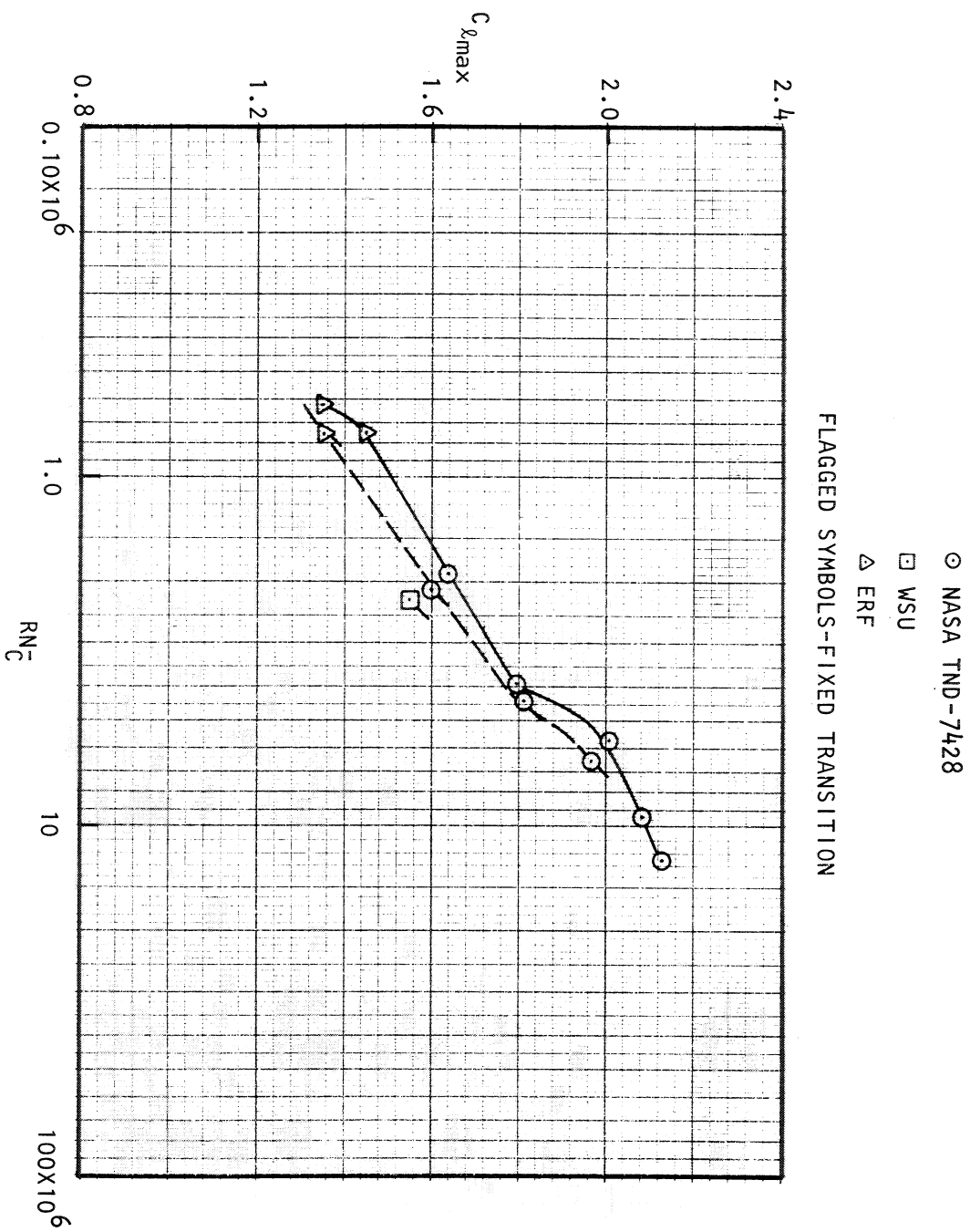


FIGURE 17 - VARIATION OF MAXIMUM LIFT COEFFICIENT
 WITH REYNOLDS NUMBER, GAW-1 SINGLE-
 ELEMENT AIRFOIL ($M_\infty \approx 0.15$)

GAW-1 AIRFOIL
SINGLE ELEMENT

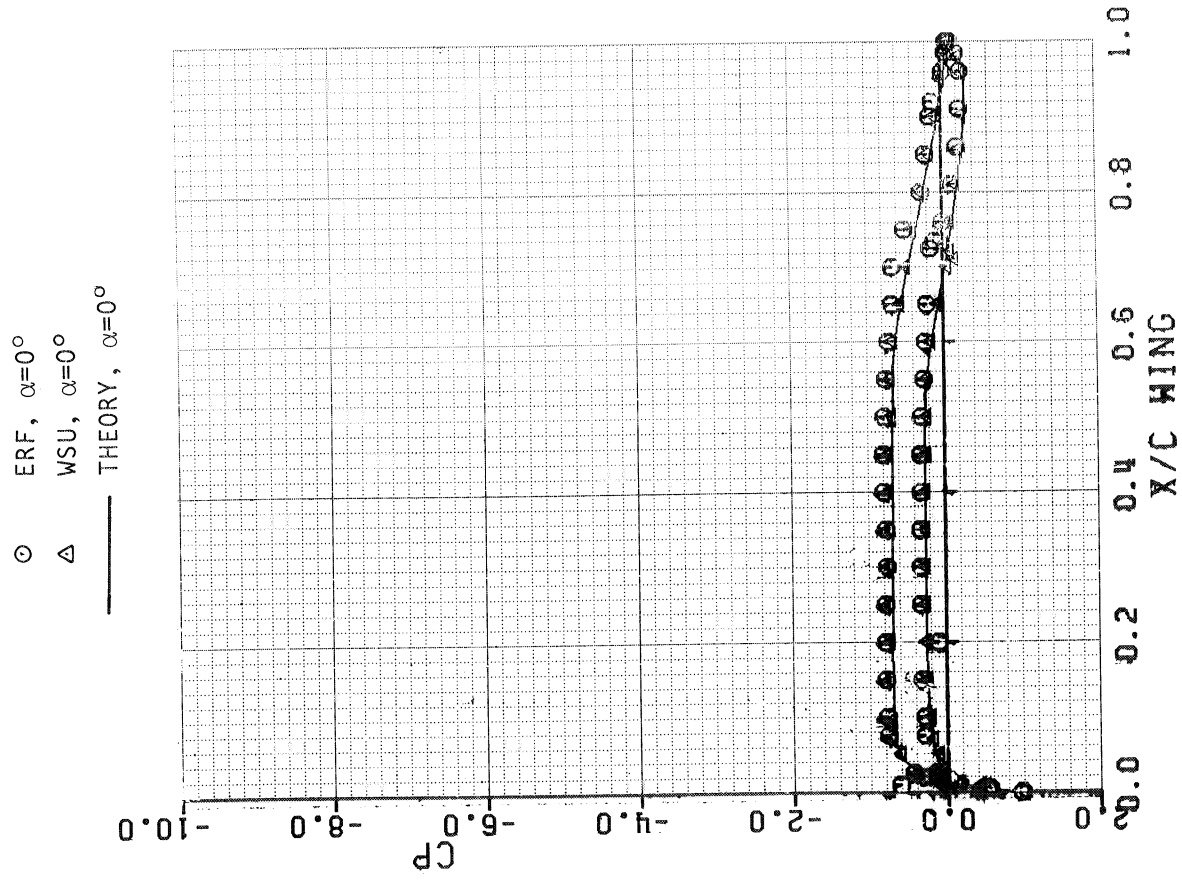


FIGURE 18 COMPARISON OF GAW-1 AIRFOIL
SURFACE PRESSURE DISTRIBUTIONS

GAW-1 AIRFOIL
SINGLE ELEMENT

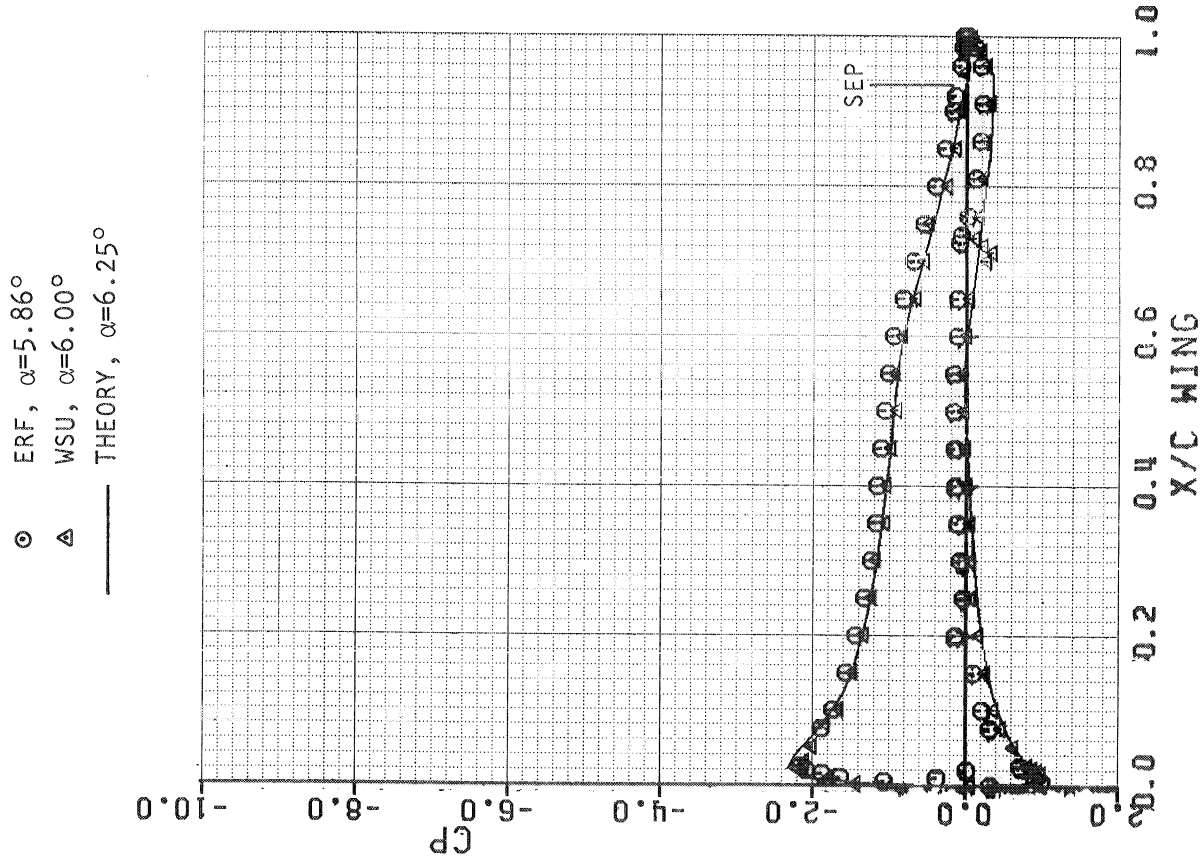


FIGURE 19 COMPARISON OF GAW-1 AIRFOIL
SURFACE PRESSURE DISTRIBUTIONS

GAW-1 AIRFOIL
SINGLE ELEMENT

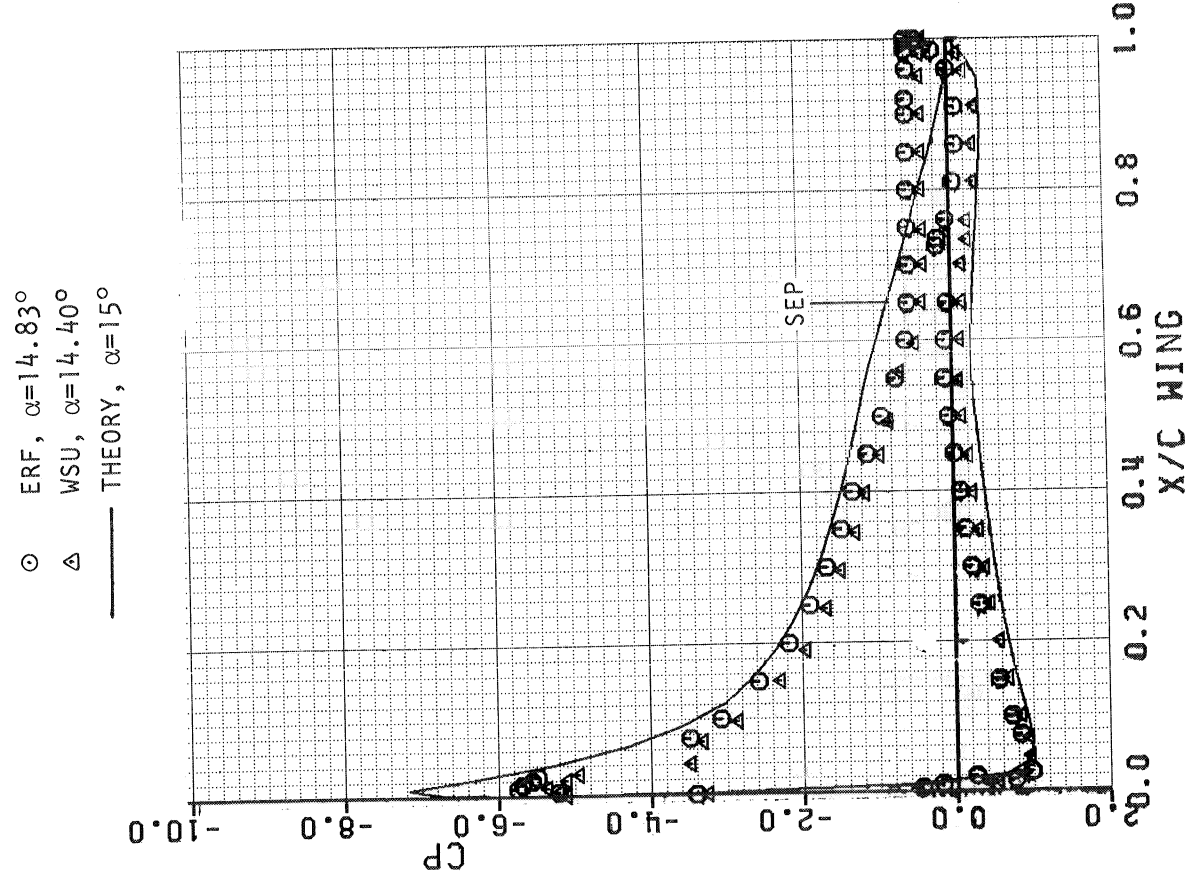


FIGURE 20 COMPARISON OF GAW-1 AIRFOIL
SURFACE PRESSURE DISTRIBUTIONS

GAW-1 AIRFOIL

$\delta_f = 30^\circ$, $(G/C)_f = .025$ $(OH/C)_f = 0.0$

- ERF, $\alpha = 4.2^\circ$
- △ WSU, $\alpha = 5^\circ$
- THEORY, $\alpha = 5^\circ$

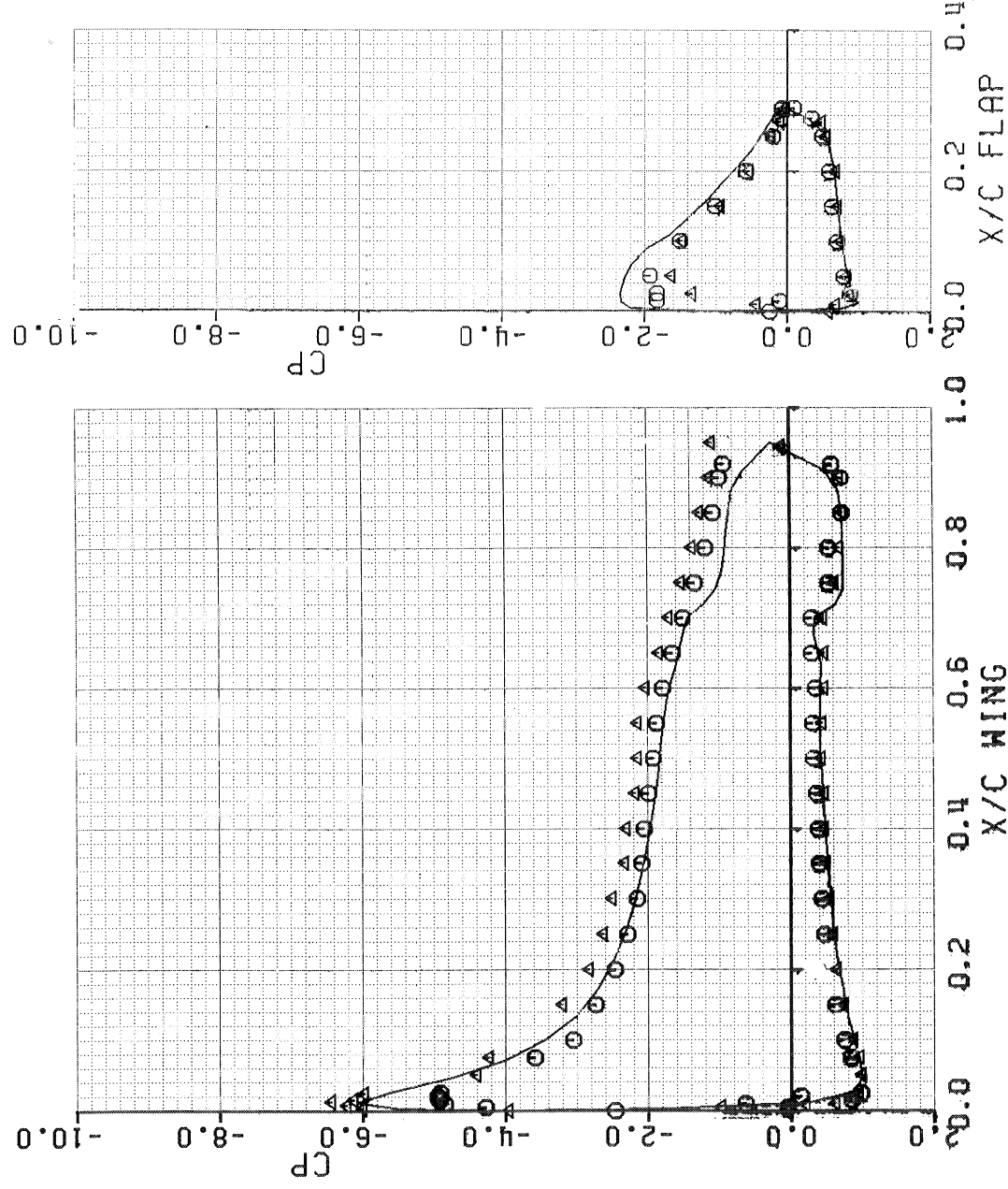


FIGURE 21 COMPARISON OF GAW-1 AIRFOIL SURFACE PRESSURE DISTRIBUTIONS

GAW-1 AIRFOIL
 $\delta_f = 30^\circ$, $(G/C)_f = .025$, $(OH/C)_f = 0.0$

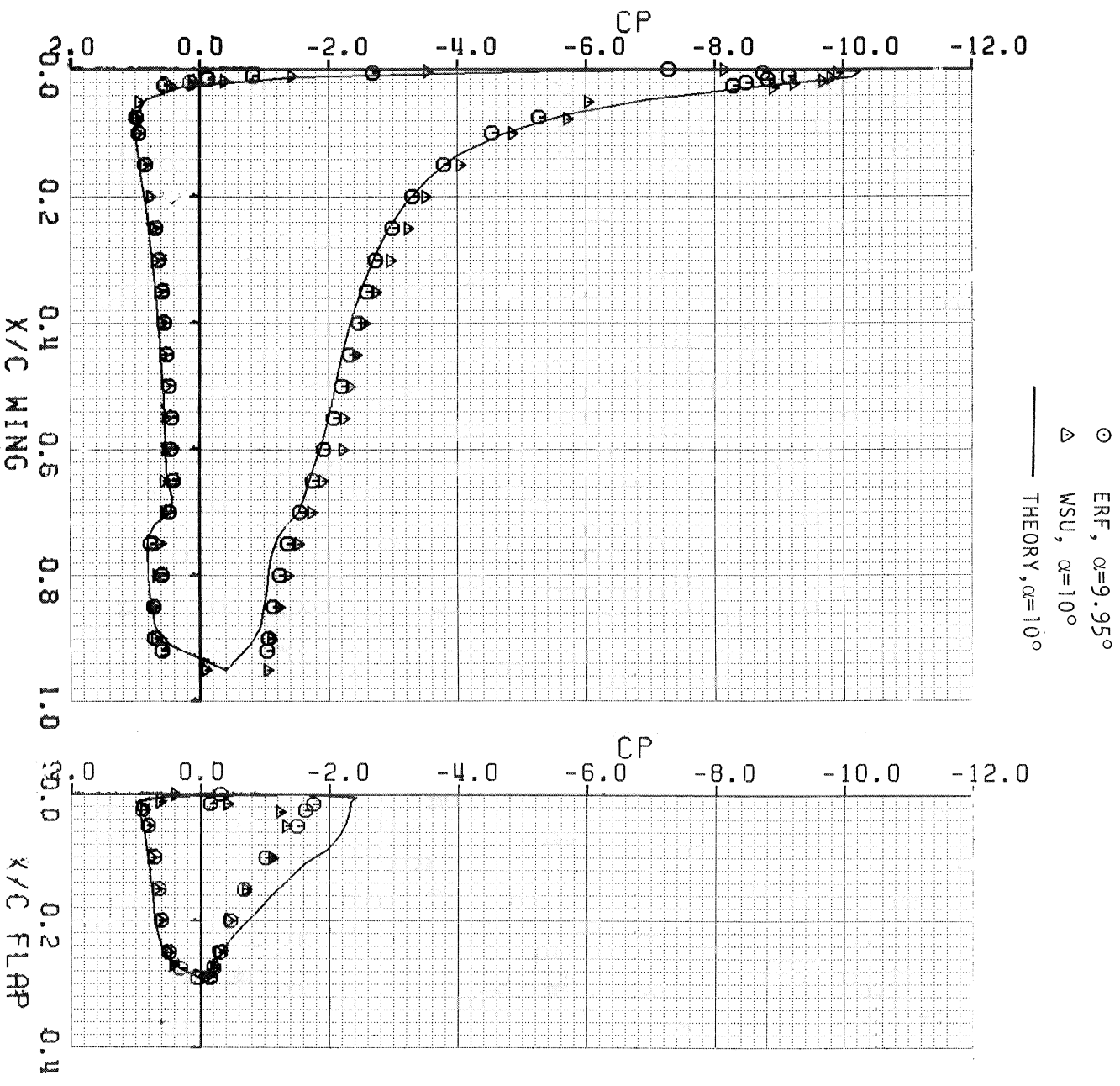
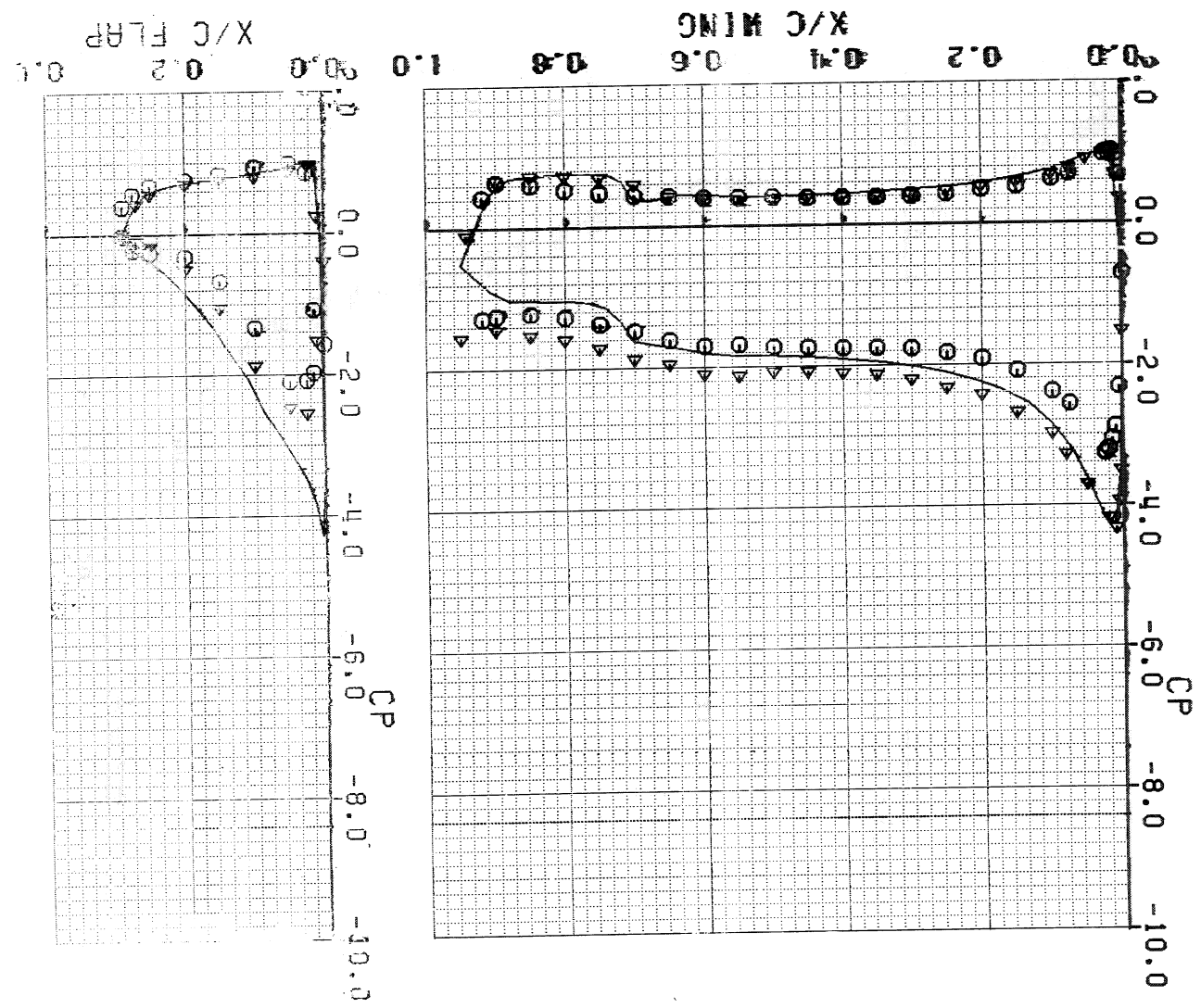


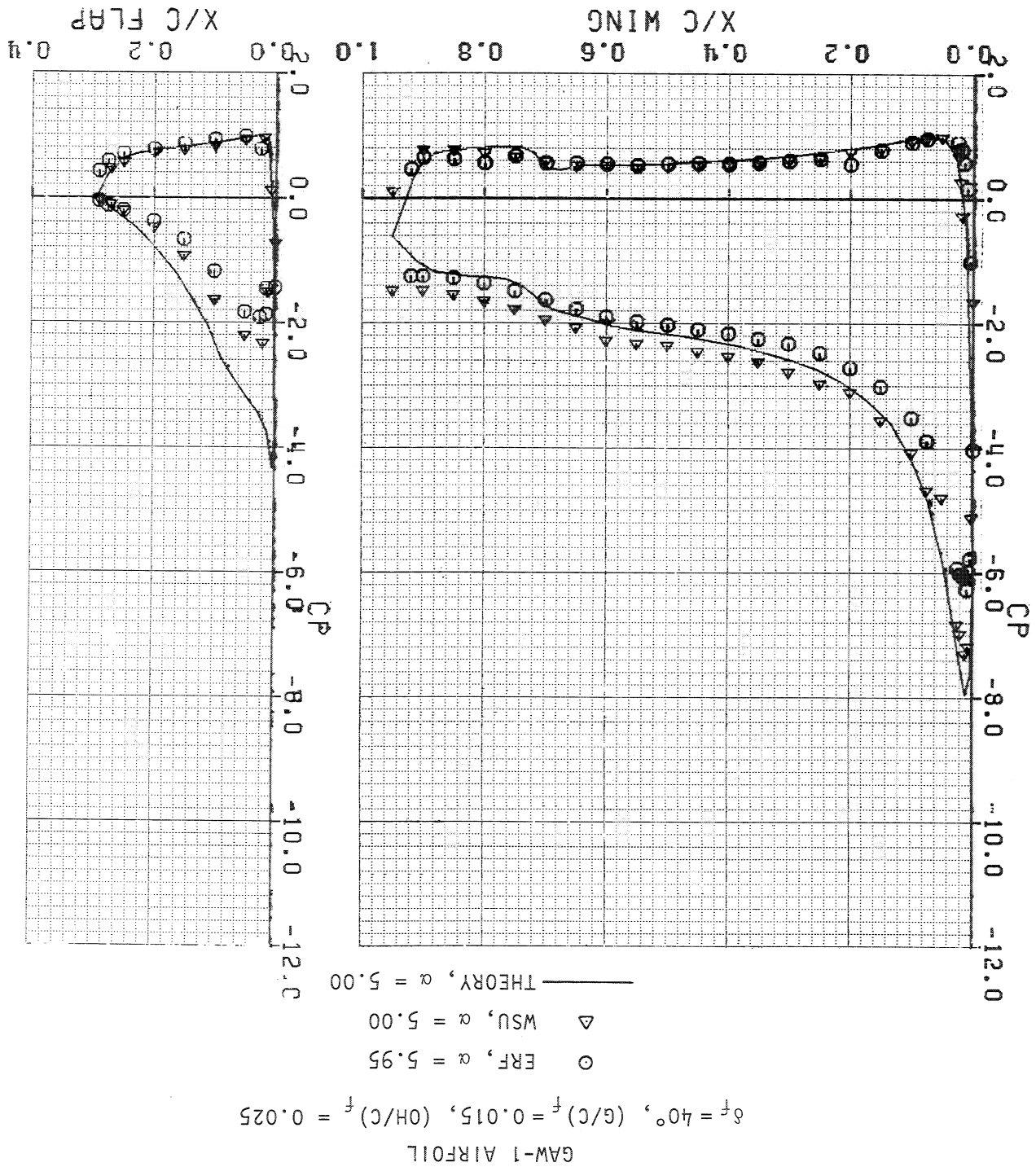
FIGURE 22 COMPARISON OF GAW-1 AIRFOIL
 SURFACE PRESSURE DISTRIBUTIONS

FIGURE 23 COMPARISON OF GAW-1 AIRFOIL SURFACE PRESSURE DISTRIBUTIONS



GAW-1 AIRFOIL
 $\delta_f^\circ = 40^\circ, (G/C)_f = 0.015, (OH/C)_f = 0.025$
 Δ WSU, $\alpha = 0.00^\circ$
 \circ ERF, $\alpha = 0.26^\circ$
 — THEORY, $\alpha = 0.00^\circ$

FIGURE 24 COMPARISON OF GAW-1 AIRFOIL SURFACE PRESSURE DISTRIBUTIONS



○ SINGLE-ELEMENT CONFIG. A

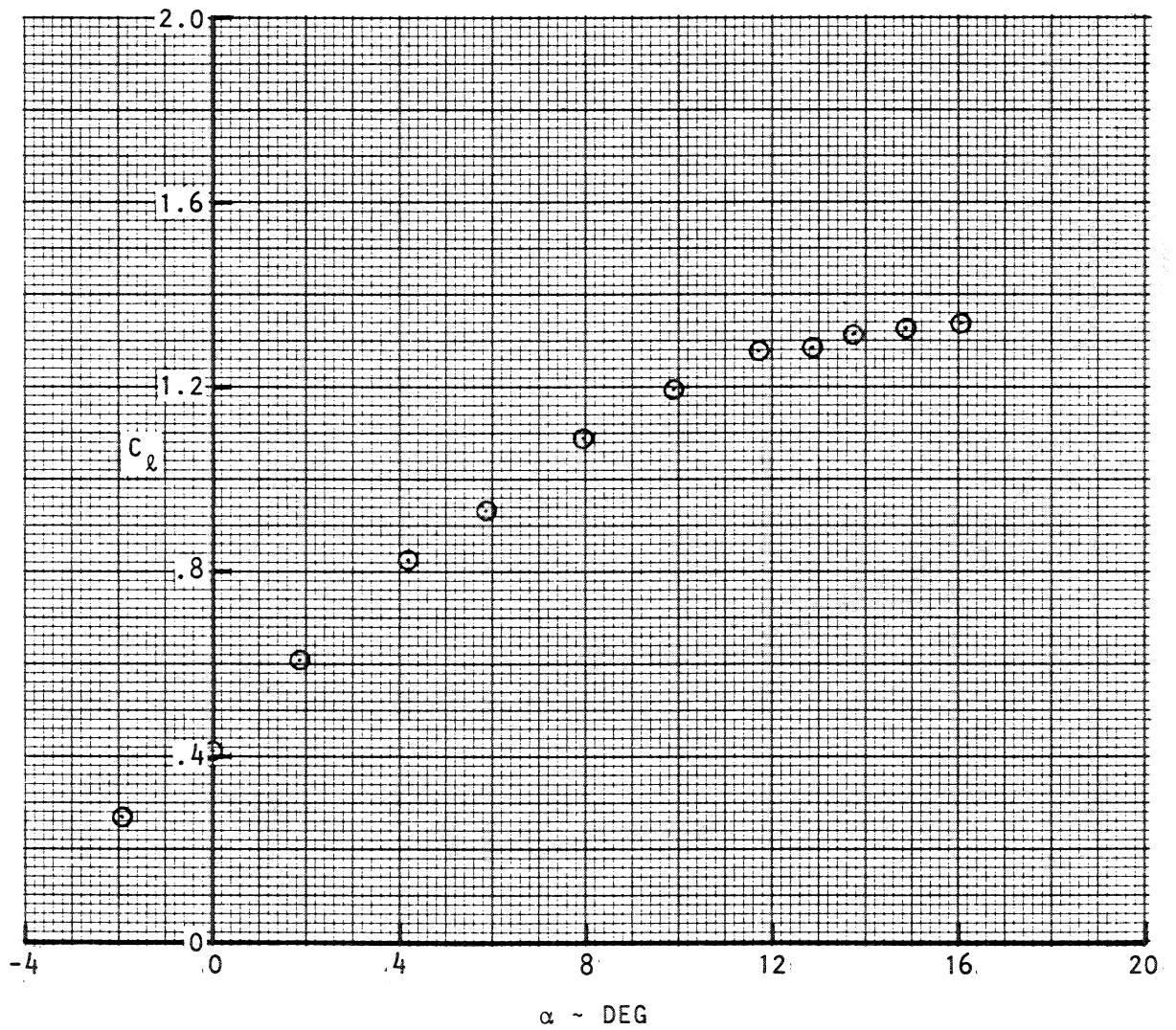


FIGURE 25 VARIATION OF LIFT COEFFICIENT WITH
ANGLE-OF-ATTACK, GAW-1 AIRFOIL

SYM	δ_f	$(g/c)_f$	$(\text{OH}/c)_f$	CONFIG.
○	30°	0.040	0.0	B(1-3)
□	30°	0.025	0.0	B(4-6)

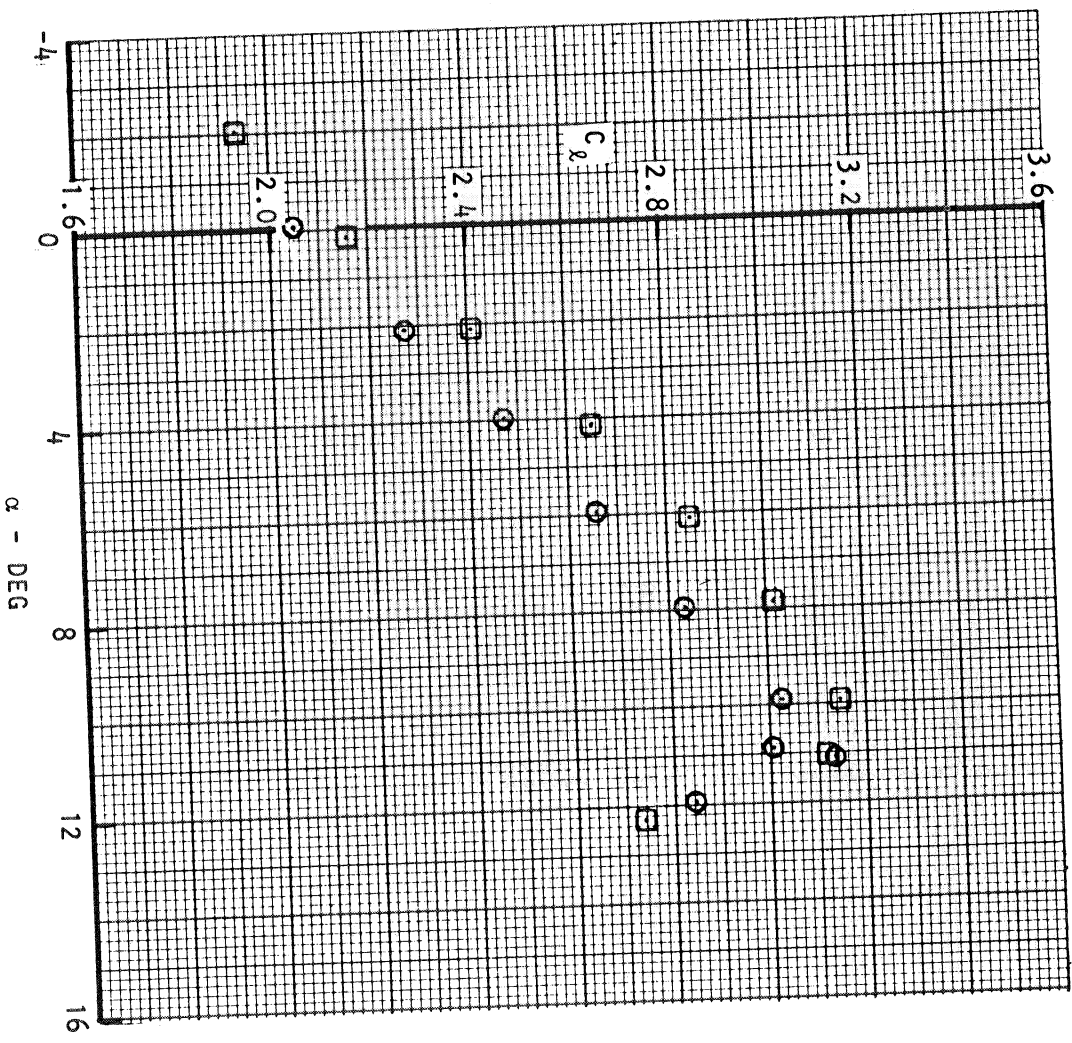


FIGURE 26 VARIATION OF LIFT COEFFICIENT WITH
ANGLE-OF-ATTACK, GAW-1 AIRFOIL

SINGLE ELEMENT AIRFOIL
 $\alpha = 11.72^\circ$

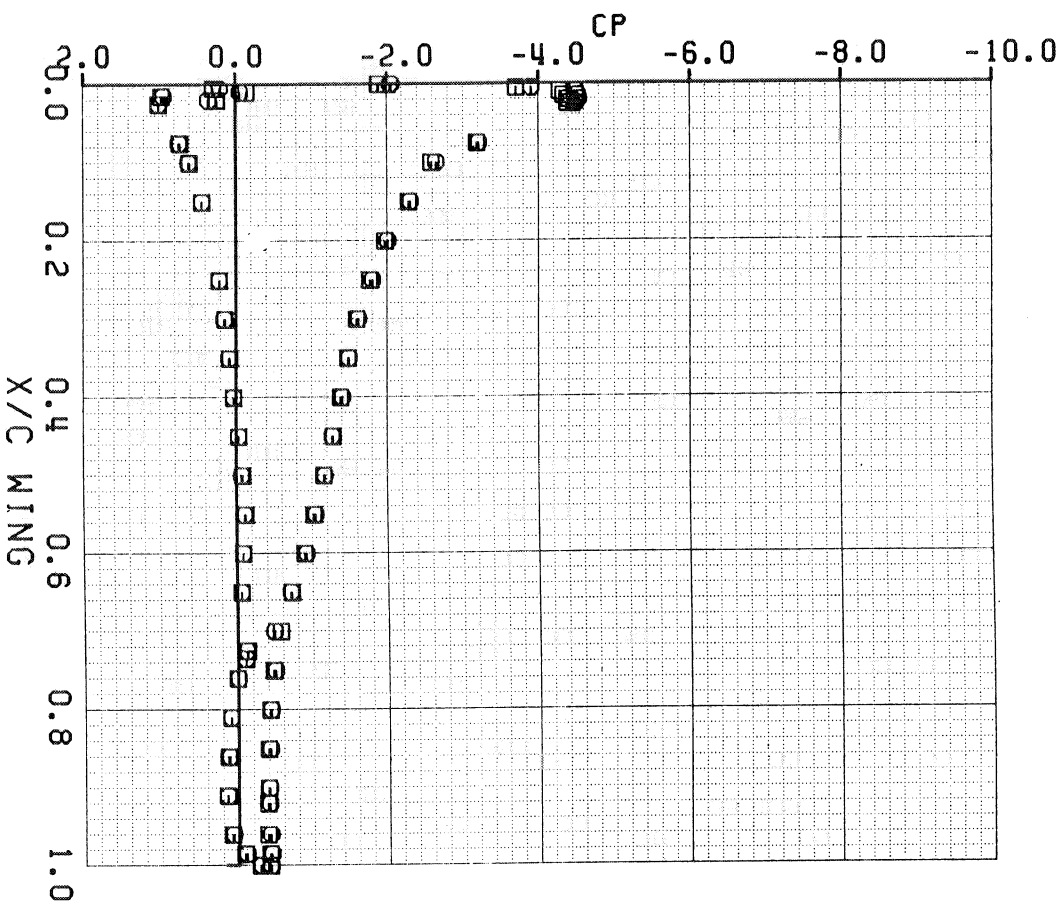


FIGURE 29 GAW-1 AIRFOIL CONFIGURATION FOR LV-
 SURVEYS - PRESSURE DISTRIBUTION, CONFIG. A-4

δ_f	$(G/C)_f$	$(OH/C)_f$
30°	0.025	0.00

$\alpha - 11.95^\circ$

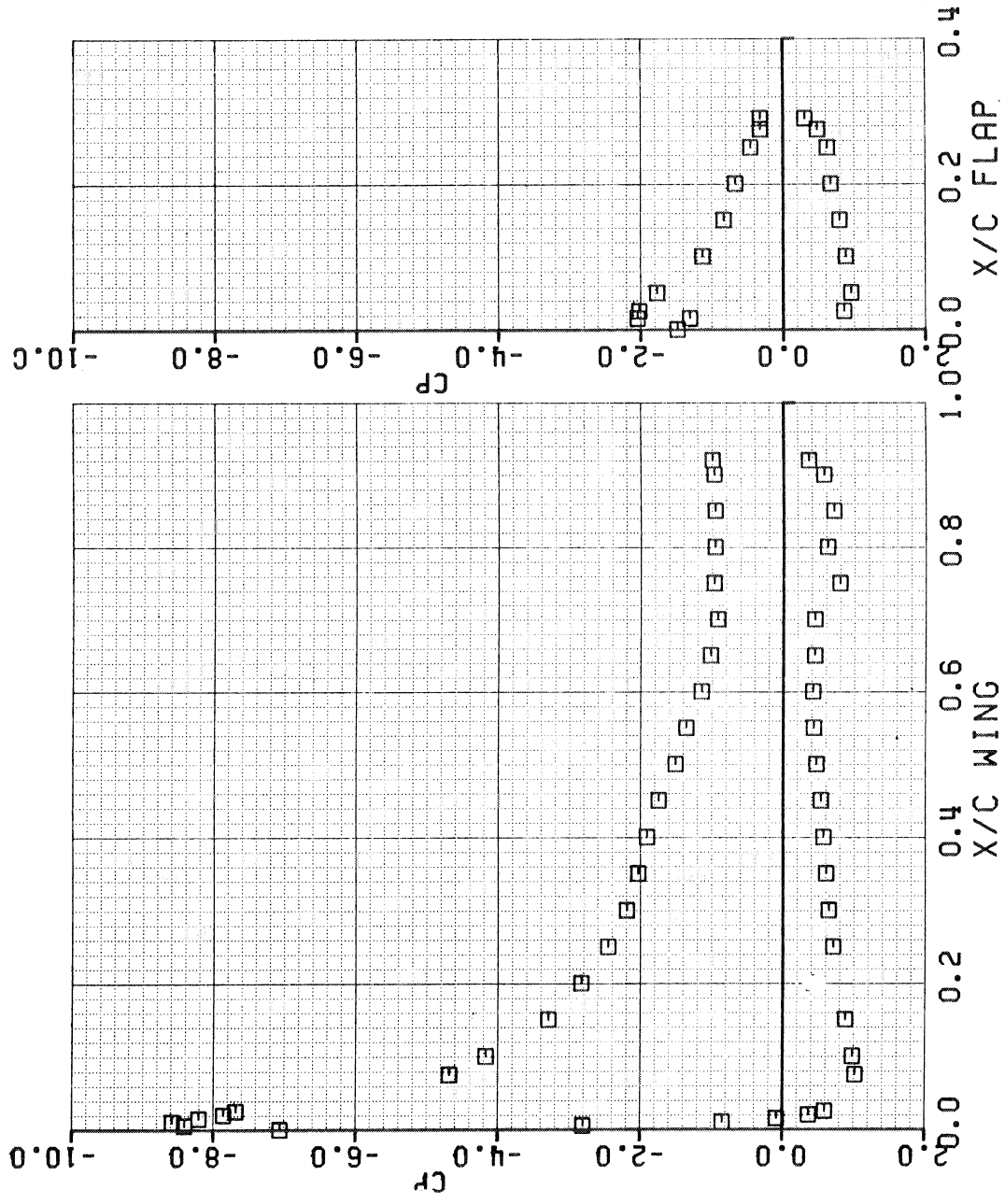


FIGURE 30 GAW-1 AIRFOIL CONFIGURATION FOR LV-SURVEYS-
PRESSURE DISTRIBUTION, CONFIG. B-3

δ_f	$(G/C)_f$	$(OH/C)_f$
40°	0.015	0.025

$$\alpha = 7.99^\circ$$

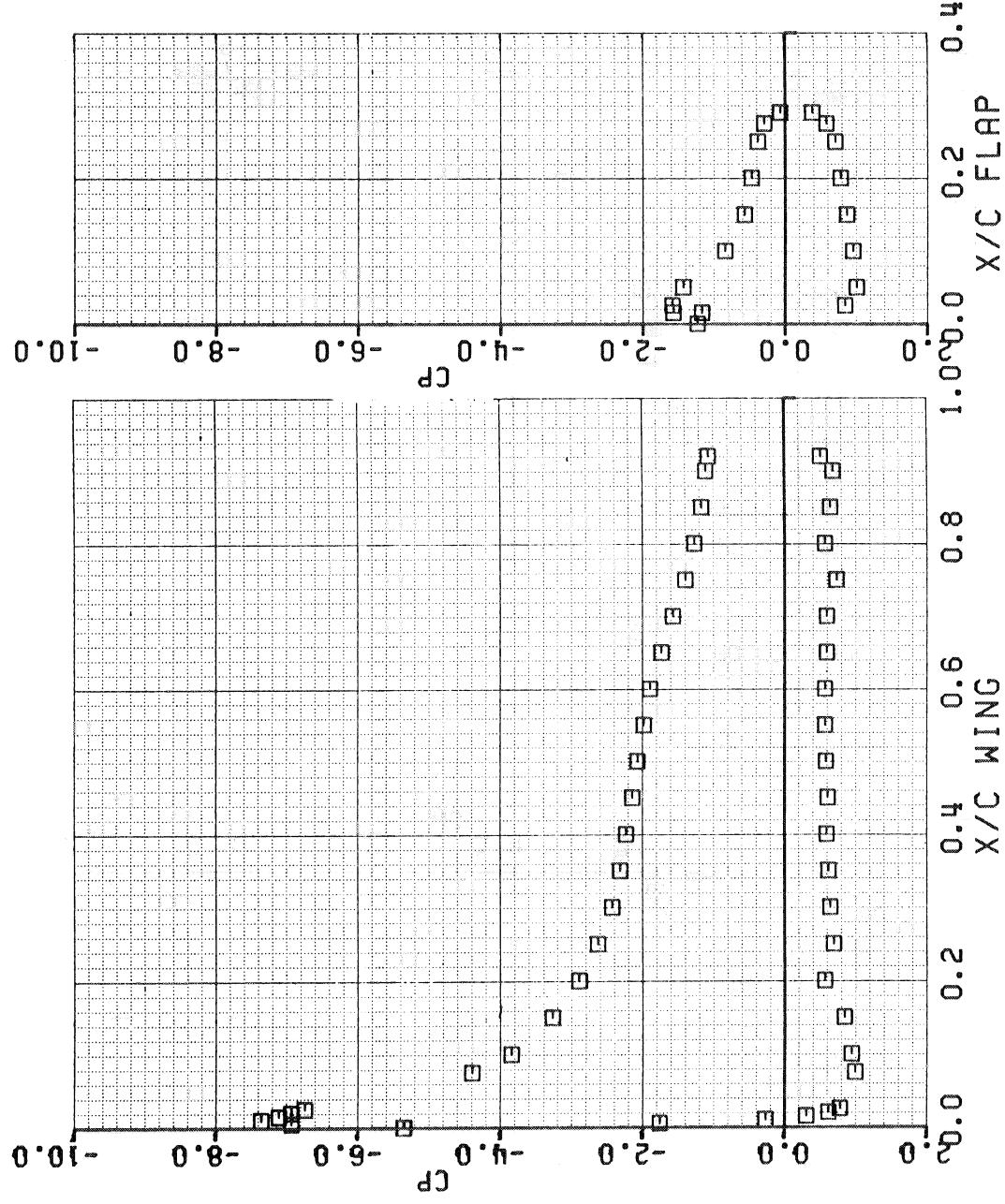


FIGURE 31 GAW-1 AIRFOIL CONFIGURATION FOR LV-SURVEYS-PRESSURE DISTRIBUTION, CONFIG. C-2

δ_s	$(G/C)_f$	$(OH/C)_f$
27°	0.023	0.028

$$\alpha = 21.48^\circ$$

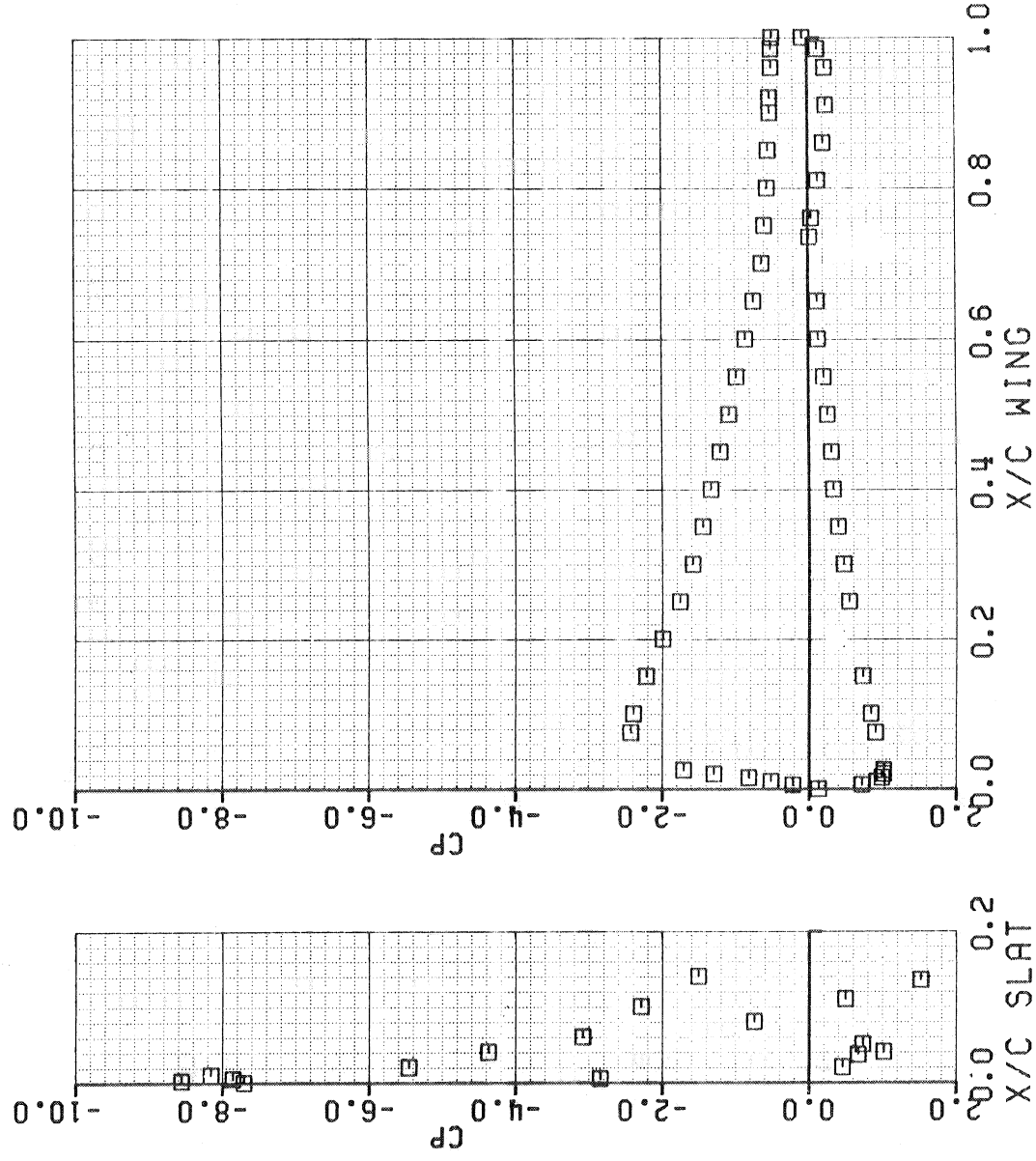


FIGURE 32 GAW-1 AIRFOIL CONFIGURATION FOR LV-SURVEYS-
PRESSURE DISTRIBUTION, CONFIG. D-2.

δ_f	$(G/C)_f$	$(OH/C)_f$	δ_s	$(G/C)_s$	$(OH/C)_s$
30°	0.025	0.0	42°	0.015	0.015

$\alpha = 16.07^\circ$

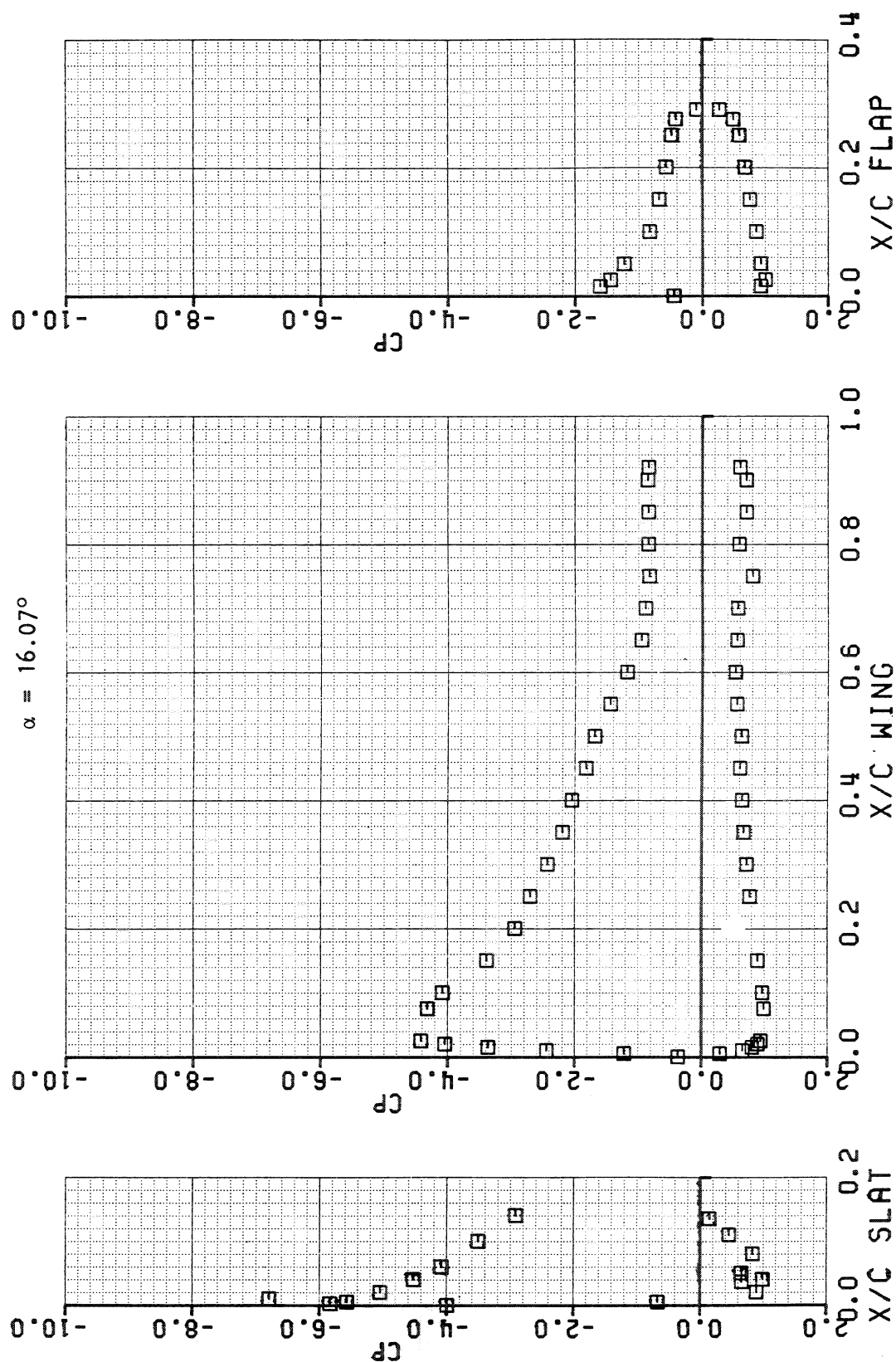


FIGURE 33 GAW-1 AIRFOIL CONFIGURATION FOR LV-SURVEYS - PRESSURE DISTRIBUTION, CONFIG. E-3

δ_f	$(G/C)_f$	$(OH/C)_f$	δ_s	$(G/C)_s$	$(OH/C)_s$
40°	0.015	0.025	42	0.015	0.015

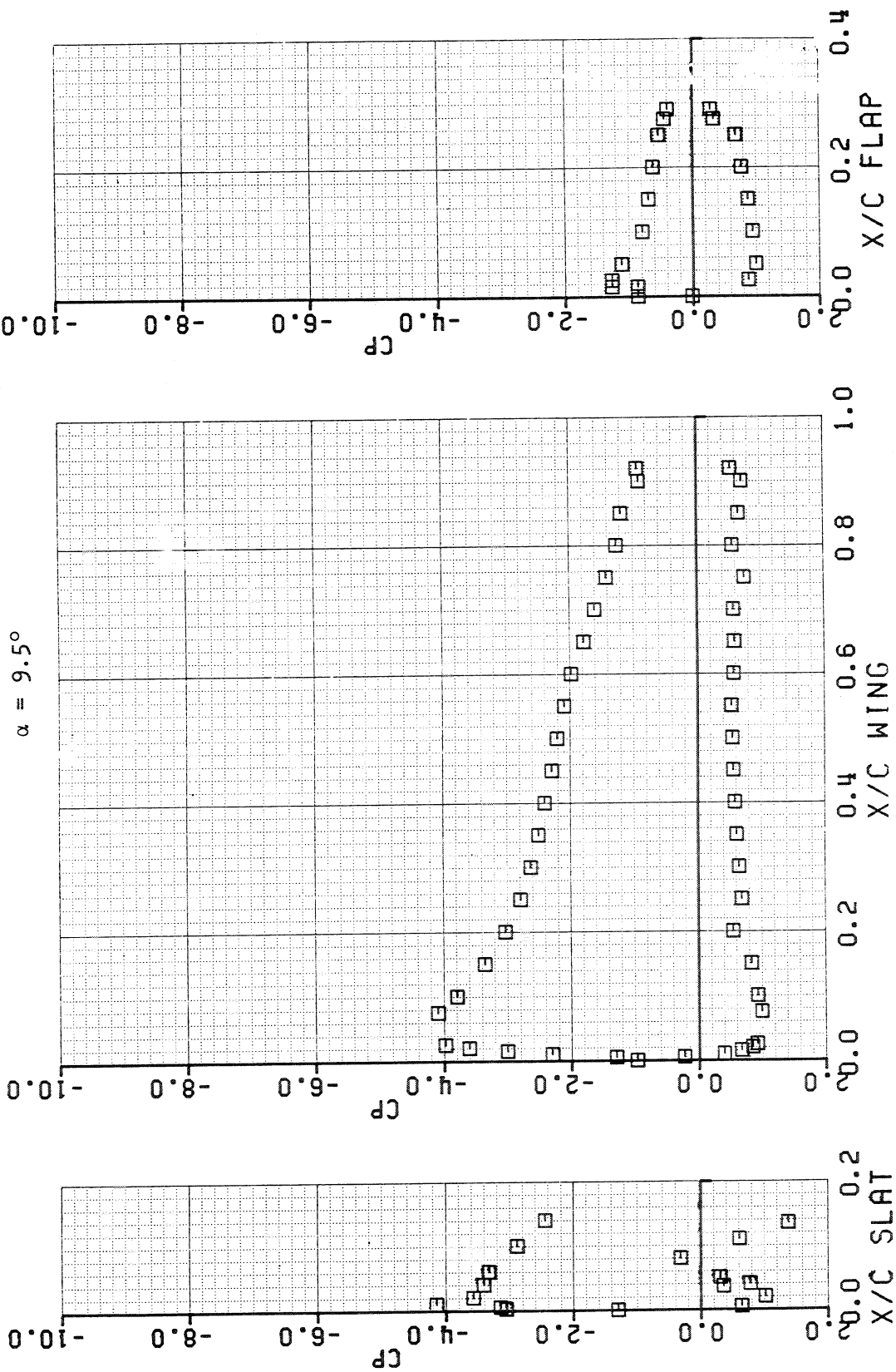


FIGURE 34 GAW-1 AIRFOIL CONFIGURATION FOR LV-SURVEYS-
PRESSURE DISTRIBUTION, CONFIG. F-2

LOCKHEED-GEORGIA COMPANY - LASER VELOCIMETER SURVEYS

ERF 027 GAW-1M ALPHA=16.00 VELOCITY VECTORS

CONFIGURATION A-5

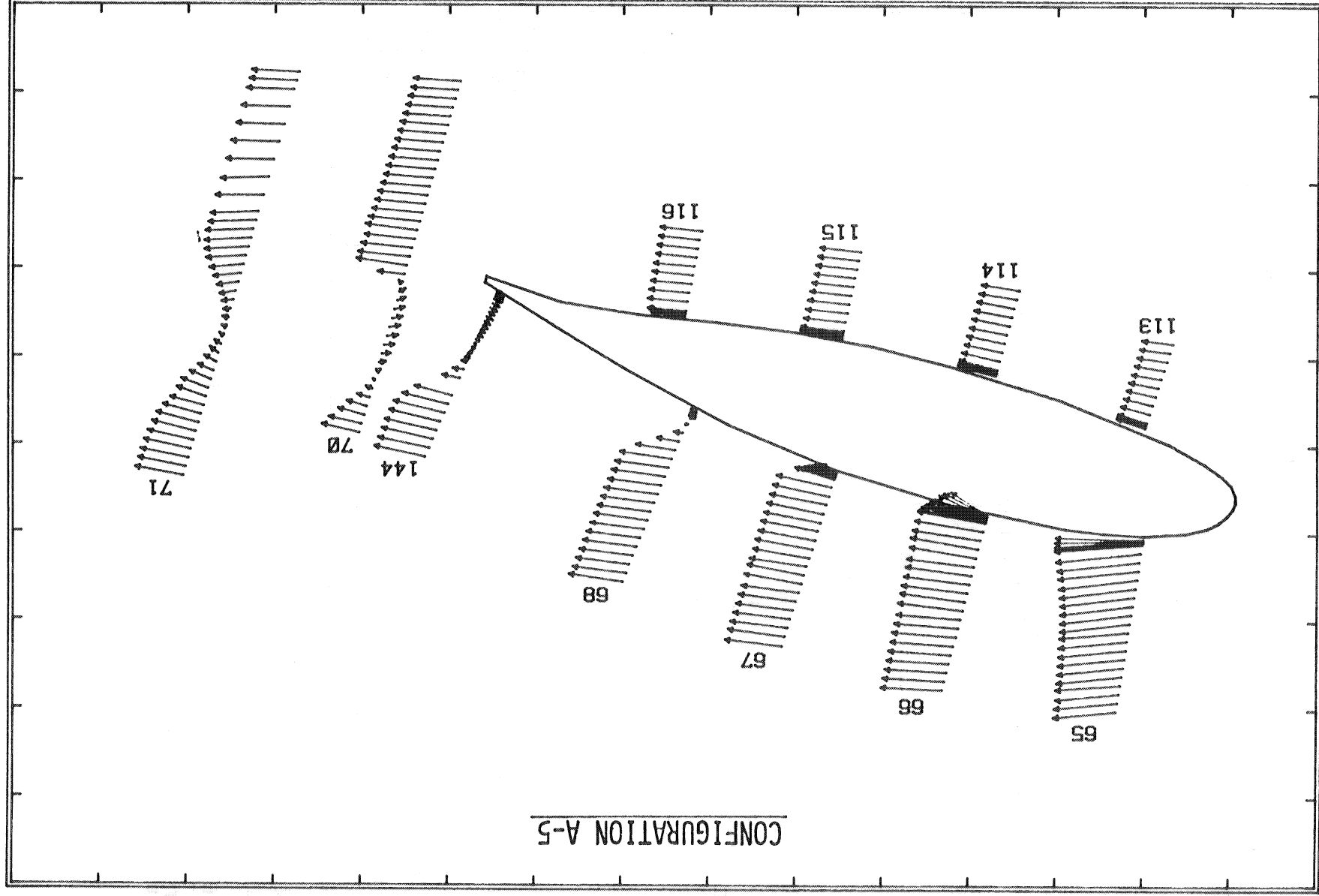


FIGURE 35. VELOCITY PROFILE COMPOSITE PLOT, $\alpha = 16^\circ$

LOCKHEED-GEORGIA COMPANY - LASER VELOCIMETER SURVEYS

GAW-1W F-30 G-0.040 OH-0.0 ALPHA=12.00 VELOCITY VECTORS

CONFIGURATION B-3

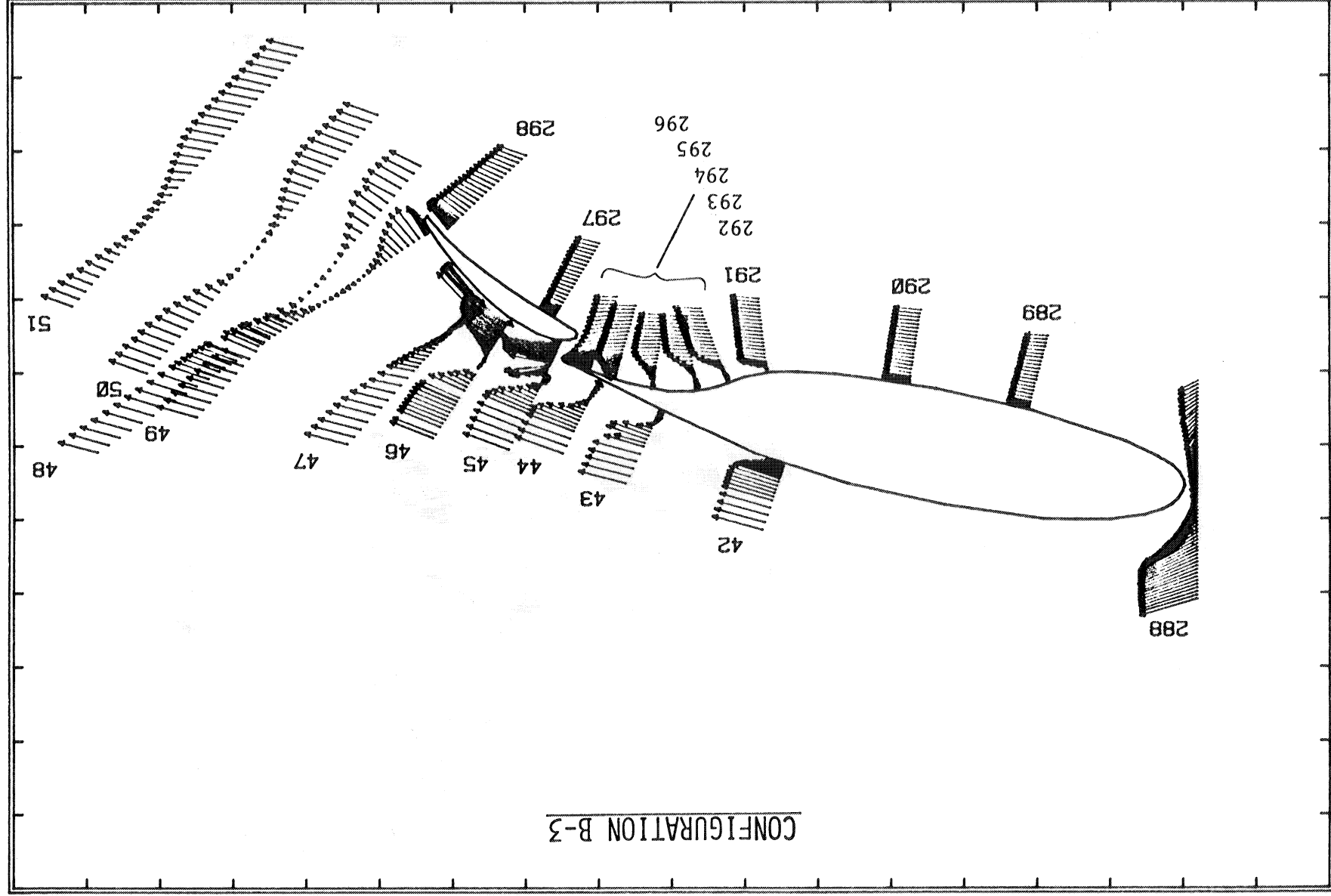


FIGURE 36. VELOCITY PROFILE COMPOSITE PLOT, $\alpha = 12^\circ$

LOCKHEED-GEORGIA COMPANY - LASER VELOCIMETER SURVEYS

GAW-1W F-40 G-0.015 OH-0.025 ALPHA=10.00 VELOCITY VECTORS

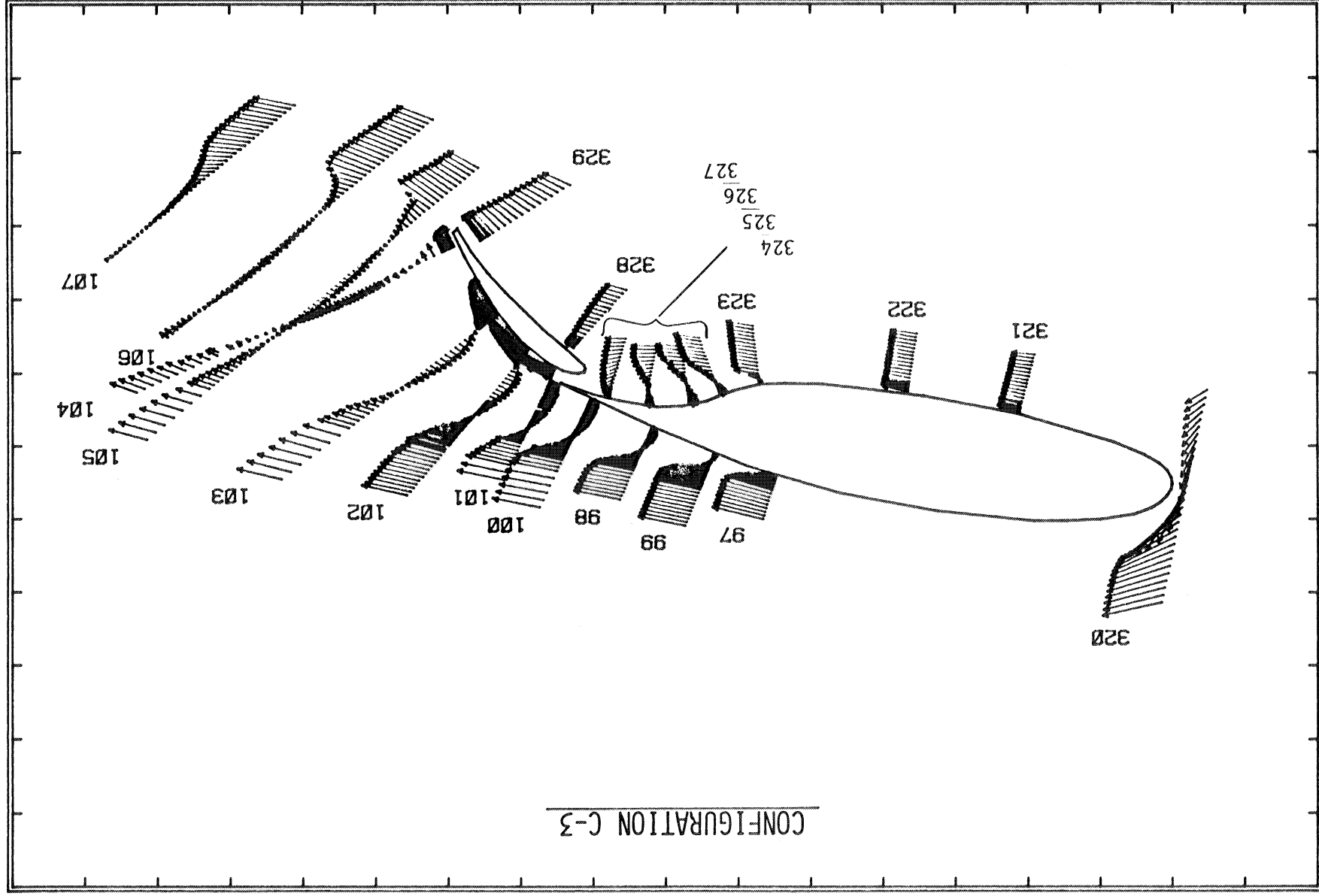


FIGURE 37. VELOCITY PROFILE COMPOSITE PLOT, $\alpha = 10^\circ$

LOCKHEED-GEORGIA COMPANY - LASER VELOCIMETER SURVEYS

GAW-1W F-0 S-27.0 G-.023 0-.028

ALPHA=24.00

VELOCITY VECTORS

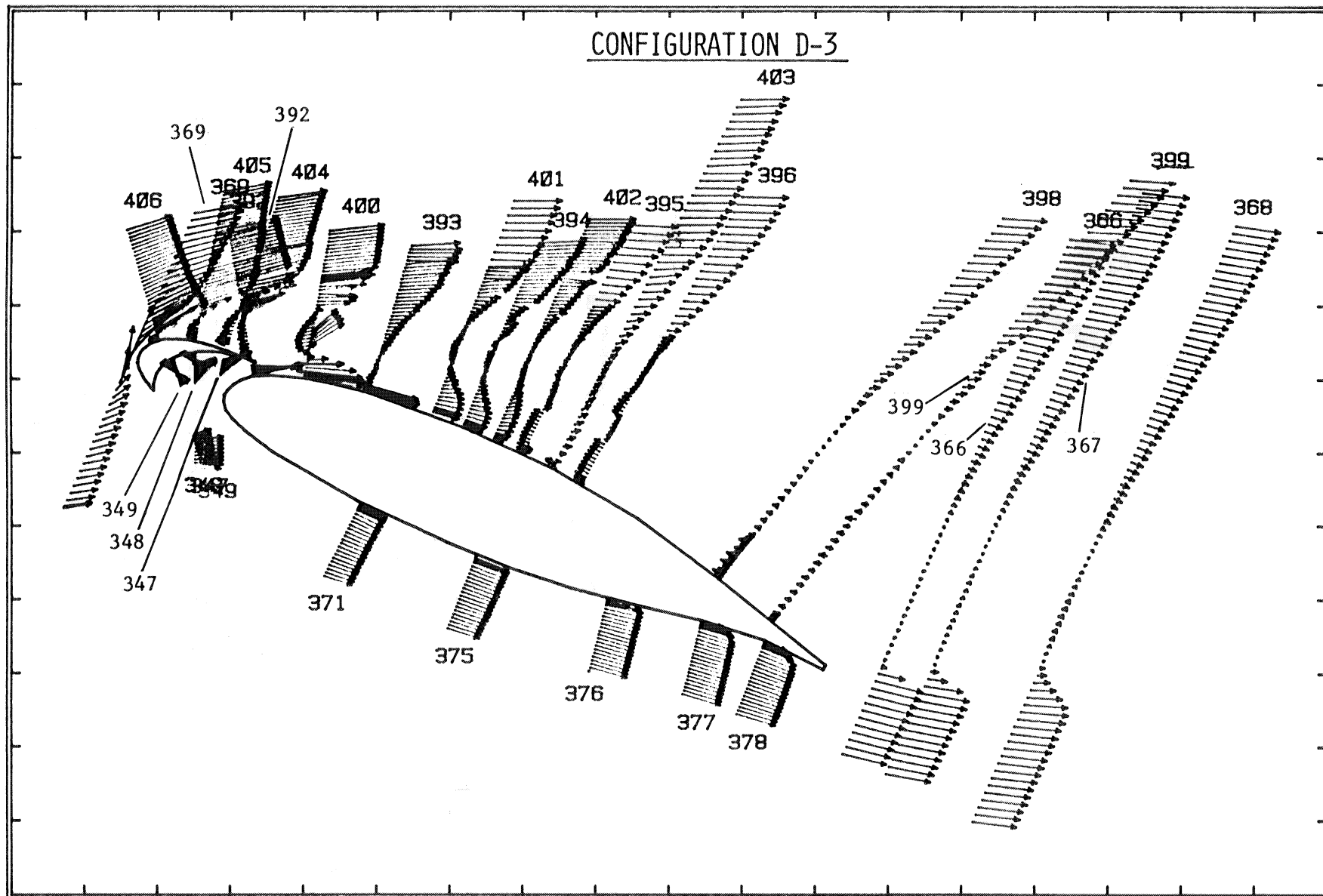


FIGURE 38. VELOCITY PROFILE COMPOSITE PLOT, $\alpha = 24^\circ$

LOCKHEED-GEORGIA COMPANY - LASER VELOCIMETER SURVEYS

GAW-1W F-30 G-0.025 OH-0.0 S-42.5 G-0.015 OH-0.015 ALPHA-16.00 VELOCITY VECTORS

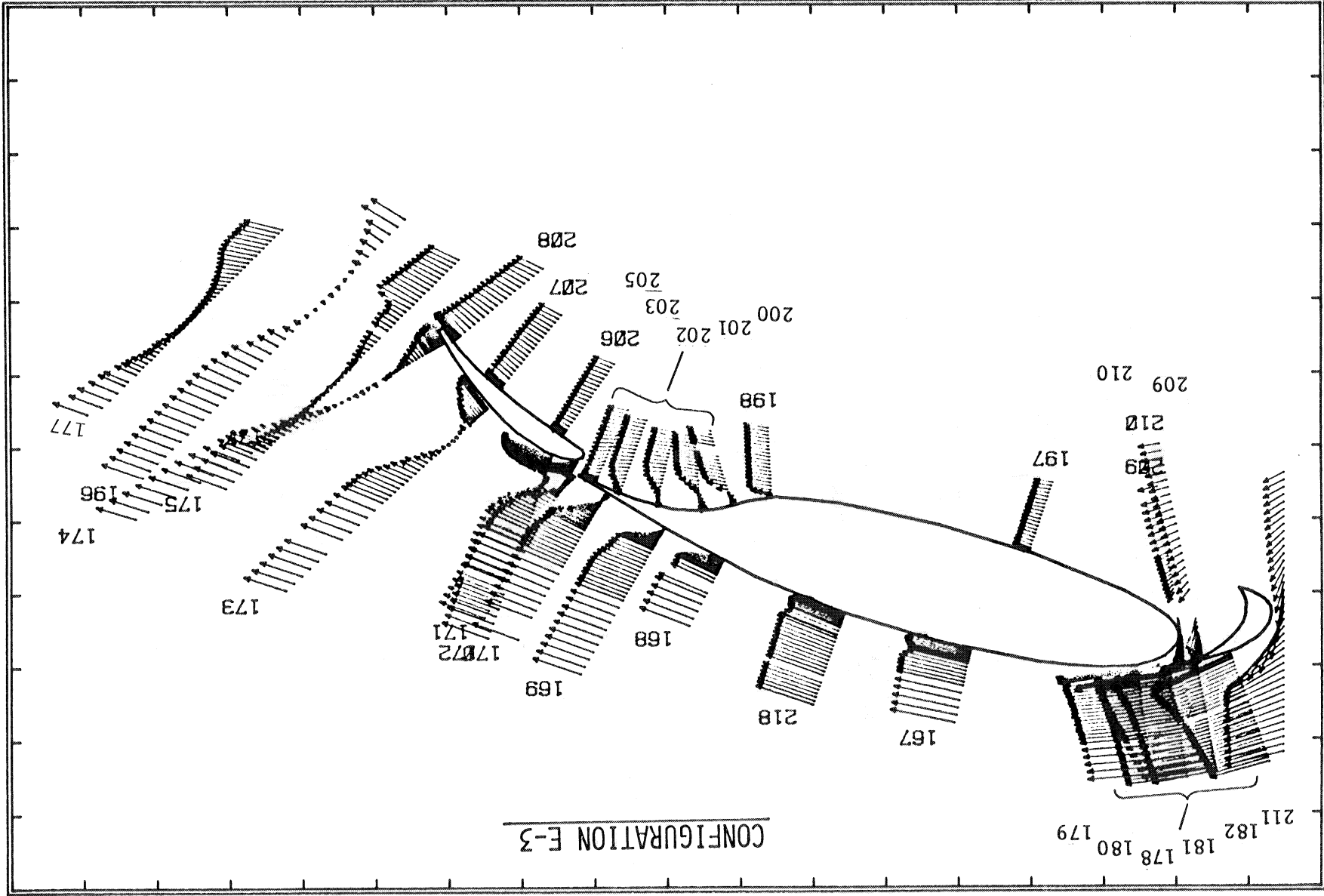


FIGURE 39. VELOCITY PROFILE COMPOSITE PLOT, $\alpha = 16^\circ$

LOCKHEED-GEORGIA COMPANY - LASER VELOCIMETER SURVEYS

GAW-1W F=40 G=.015 OH=.025 S=42 G=.015 OH=.015

ALPHA=14.00

VELOCITY VECTORS

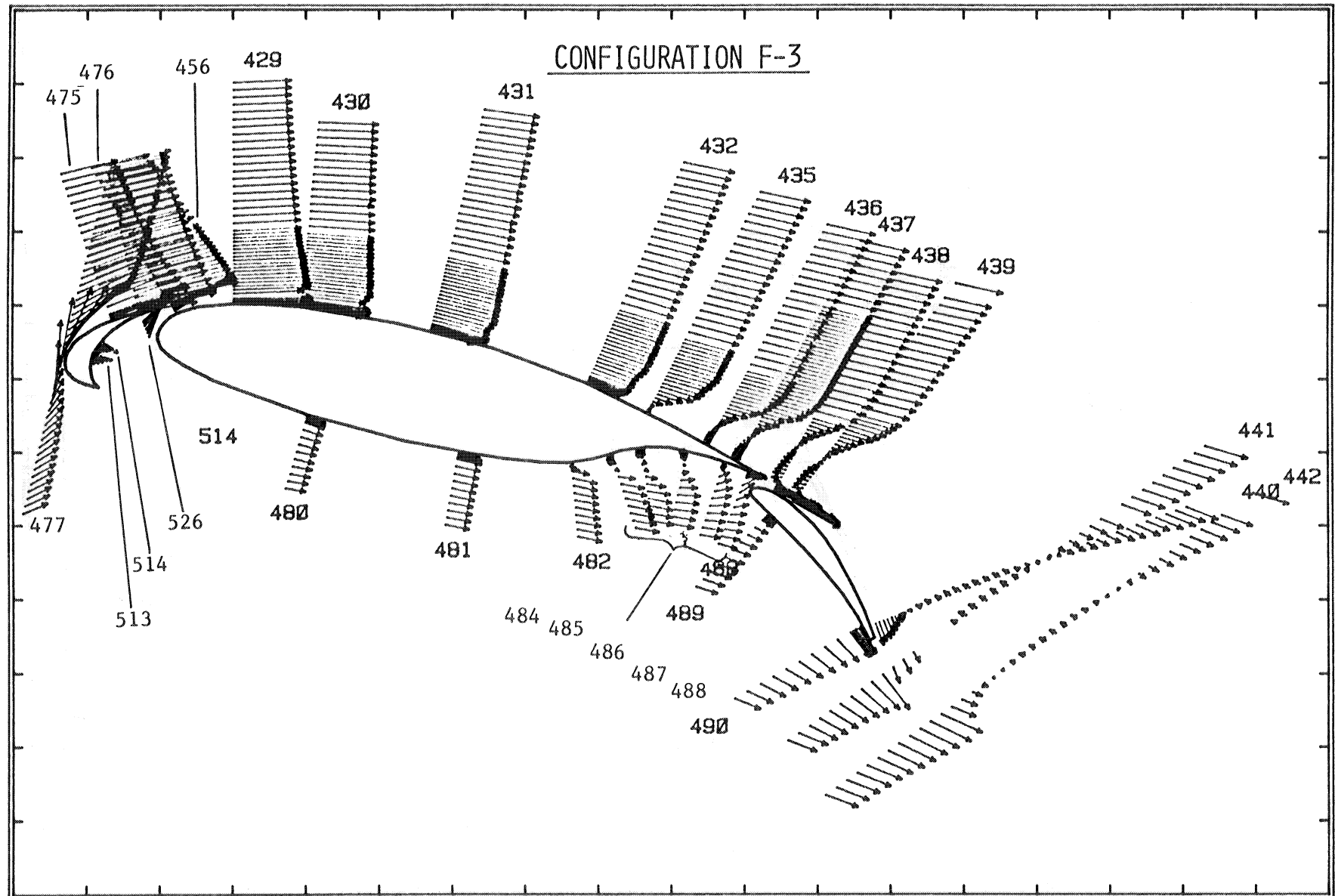


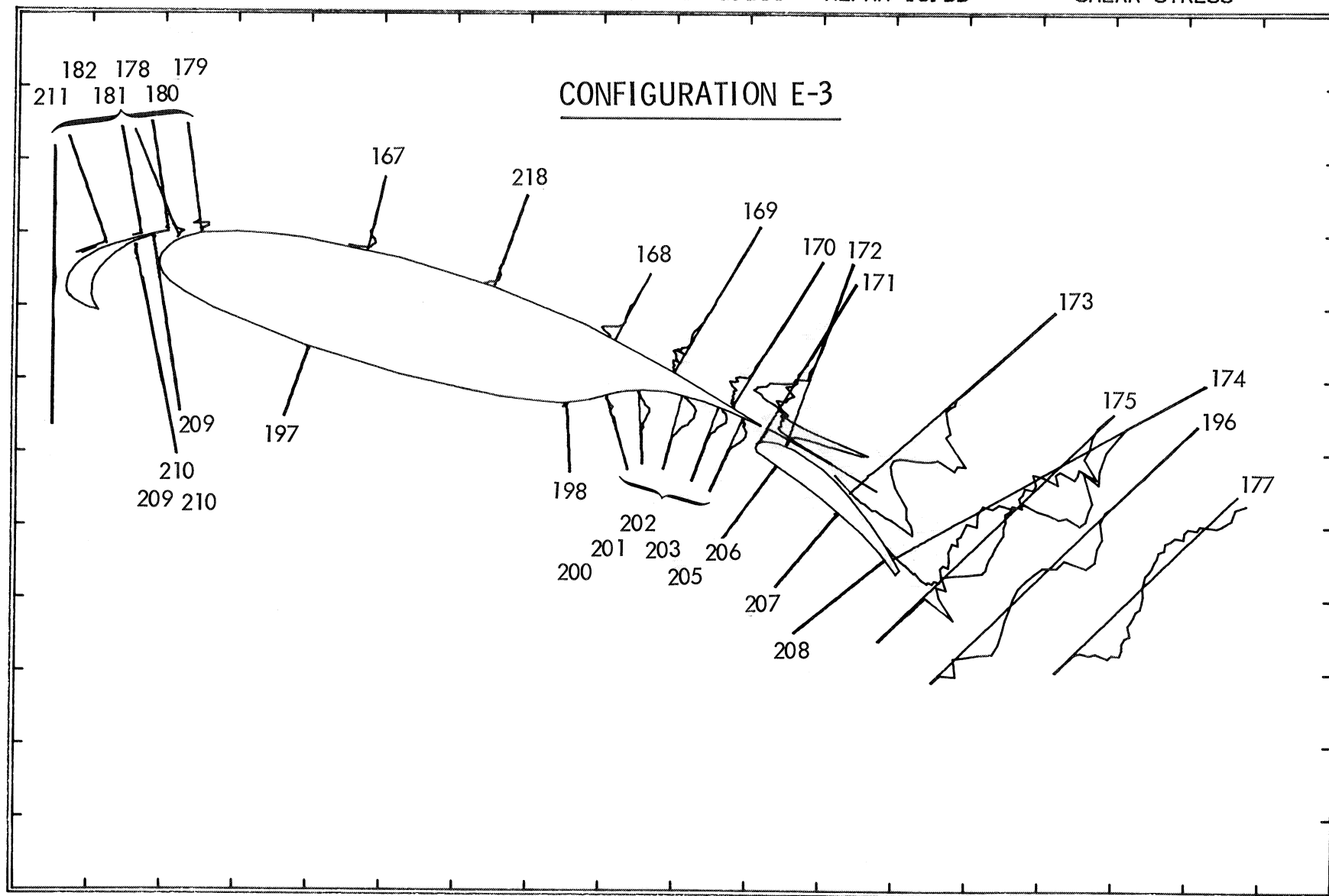
FIGURE 40. VELOCITY PROFILE COMPOSITE PLOT, $\alpha = 14^\circ$

LOCKHEED-GEORGIA COMPANY - LASER VELOCIMETER SURVEYS

GAW-1W F=30 G=0.025 OH=0.0 S=42.5 G=0.015 OH=0.015

ALPHA=16.00

SHEAR STRESS

FIGURE 41(a). SHEAR STRESS COMPOSITE PLOT, $\alpha = 16^\circ$

LOCKHEED-GEORGIA COMPANY - LASER VELOCIMETER SURVEYS

GAW-1W F=30 G=0.025 OH=0.0 S=42.5 G=0.015 OH=0.015 ALPHA=16.00 U PRIME

CONFIGURATION E-3

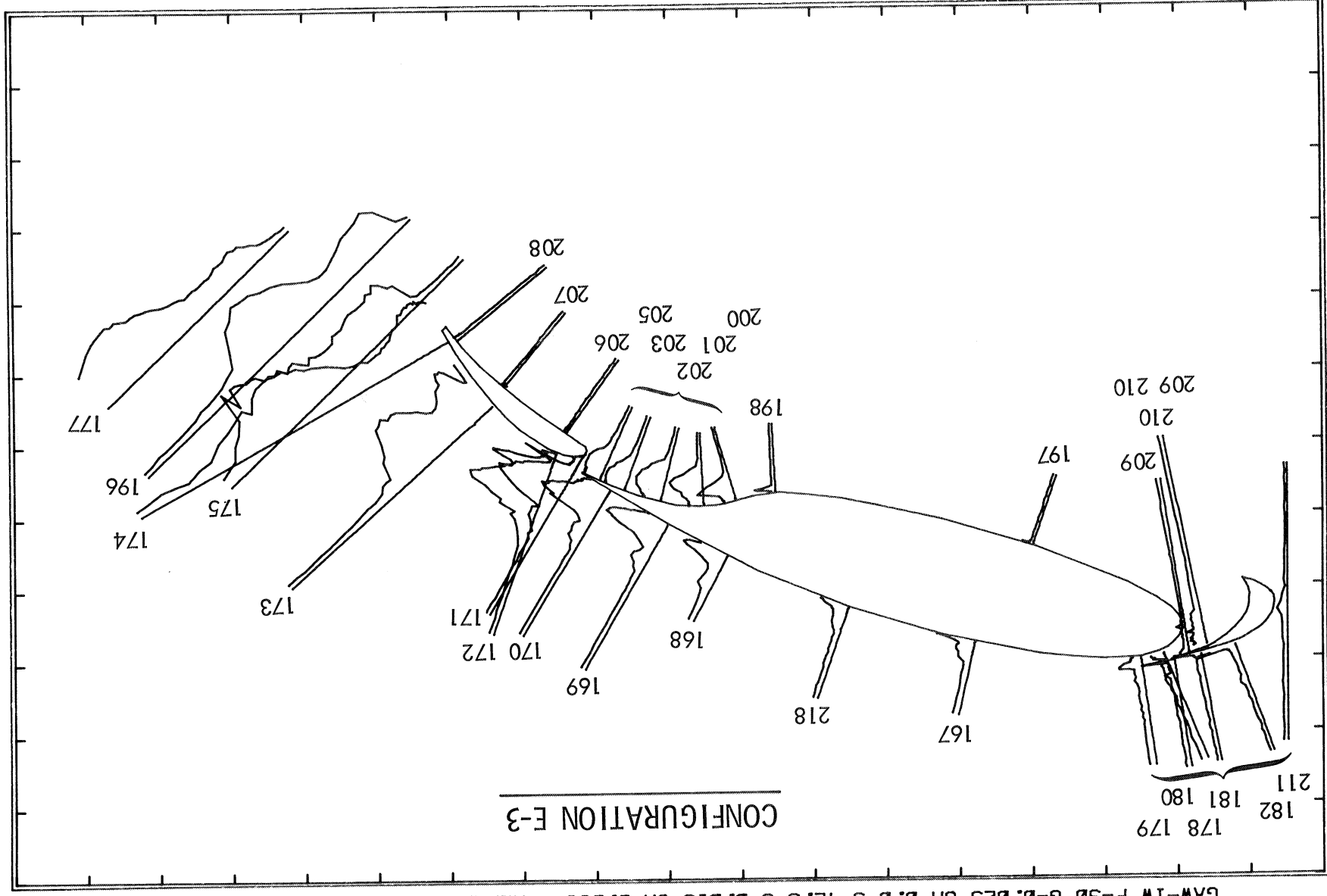


FIGURE 41(b). STREAMWISE TURBULENCE COMPONENT, u' , $\alpha = 16^\circ$

LOCKHEED-GEORGIA COMPANY - LASER VELOCIMETER SURVEYS

GAW-1W F=30 G=0.025 OH=0.0 S=42.5 G=0.015 OH=0.015 ALPHA=16.00 V PRIME

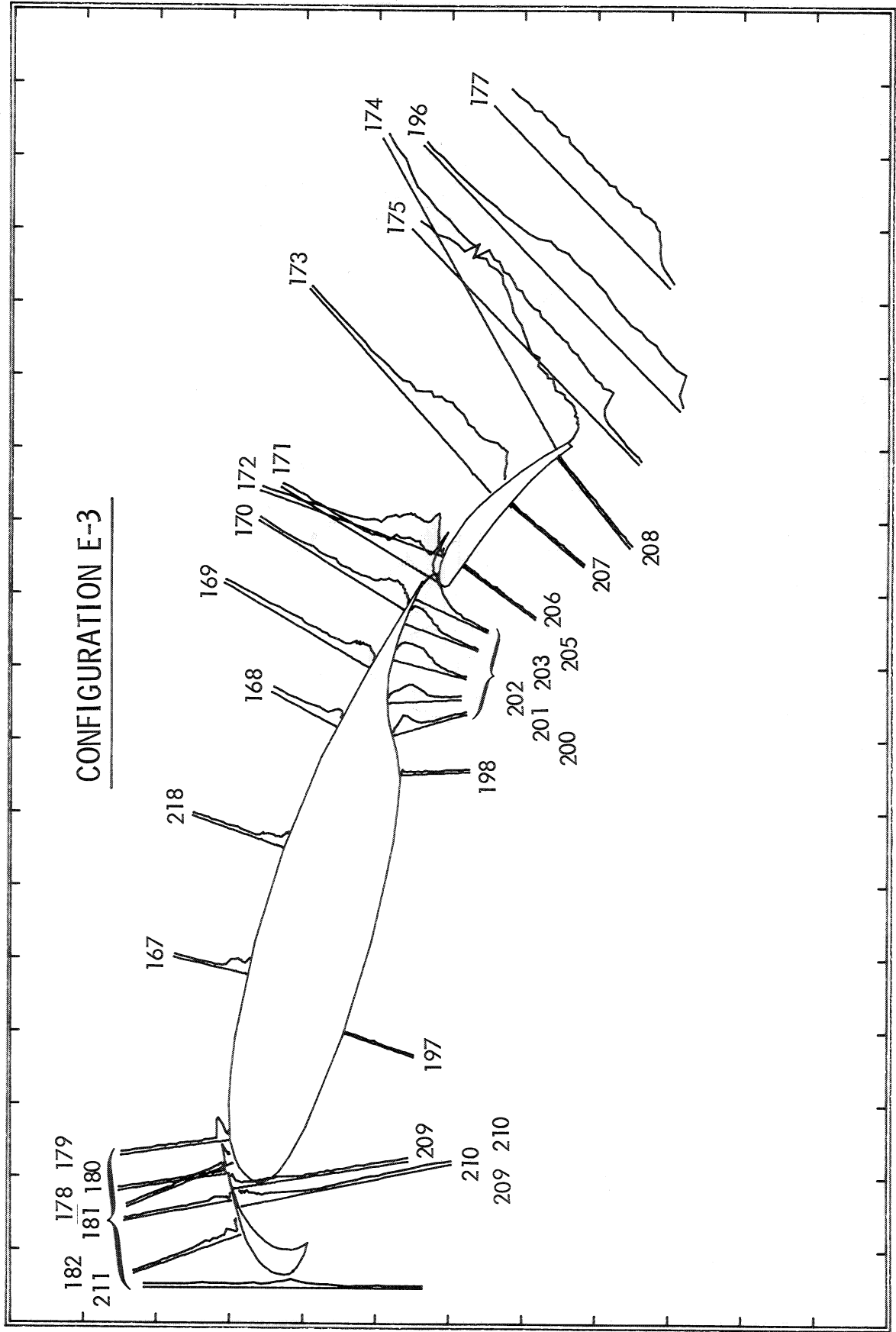


FIGURE 41(c). NORMAL TURBULENCE COMPONENT, v' , $\alpha = 16^\circ$

LOCKHEED GEORGIA COMPANY
ERF WINDTUNNEL TEST 032

RUN NUMBER 42

GAW-1M F=30 G=0.040 OH=0.0

ALPHA : 12.00

UE : 130.00

X/C : 0.60

TRANSLATION ANGLE : 18.30

			(COMP)		(PRIME)		(UVBAR)
			----- * 100		----- * 100		----- * 100
			UE		UE		UE**2

#	CODE	H	U-COMP	V-COMP	U-PRIME	V-PRIME	SHEAR

1	3	0.947	142.162	7.088	1.785	0.911	0.0079
2	4	0.842	142.128	6.234	1.599	0.769	0.0083
3	5	0.736	141.463	5.698	1.535	0.477	0.0038
4	6	0.631	142.060	4.210	1.825	0.308	0.0020
5	8	0.527	141.932	3.641	1.821	0.639	0.0017
6	9	0.473	142.563	3.007	1.682	0.091	0.0013
7	10	0.420	141.930	2.693	1.778	0.986	0.0031
8	11	0.368	141.738	1.681	1.601	0.886	0.0040
9	12	0.315	142.022	1.459	1.995	1.388	0.0038
10	13	0.262	140.755	0.514	3.136	2.699	-0.0098
11	18	0.210	131.008	-2.182	7.869	5.198	-0.1401
12	14	0.210	131.008	-2.182	8.226	4.740	-0.1068
13	19	0.189	124.619	-2.610	9.798	5.915	-0.2862
14	20	0.167	115.541	-3.821	12.008	7.025	-0.3984
15	15	0.157	111.682	-3.938	12.688	7.758	-0.4746
16	21	0.146	106.623	-3.926	13.476	8.248	-0.5346
17	22	0.125	96.251	-3.774	14.504	8.730	-0.7028
18	23	0.104	84.741	-3.367	15.817	10.000	-0.9093
19	24	0.083	74.306	-3.342	15.624	9.496	-0.8371
20	25	0.062	63.176	-2.493	15.782	9.274	-0.7967
21	26	0.041	49.962	-0.753	14.777	8.642	-0.6554
22	27	0.020	38.134	-1.294	13.093	6.851	-0.4360
23	28	0.011	29.124	-0.481	12.971	4.984	-0.3203

TABLE VI. - TYPICAL LV-DATA TABULATION

GAW-1M F=30 $C=0.040$ $OH \pm 0.0$

ERF TEST 32

RUN 42

○ U COMPONENT

+ V COMPONENT

ALPHA = 12.000

UE = 130.0

X/C = 0.600

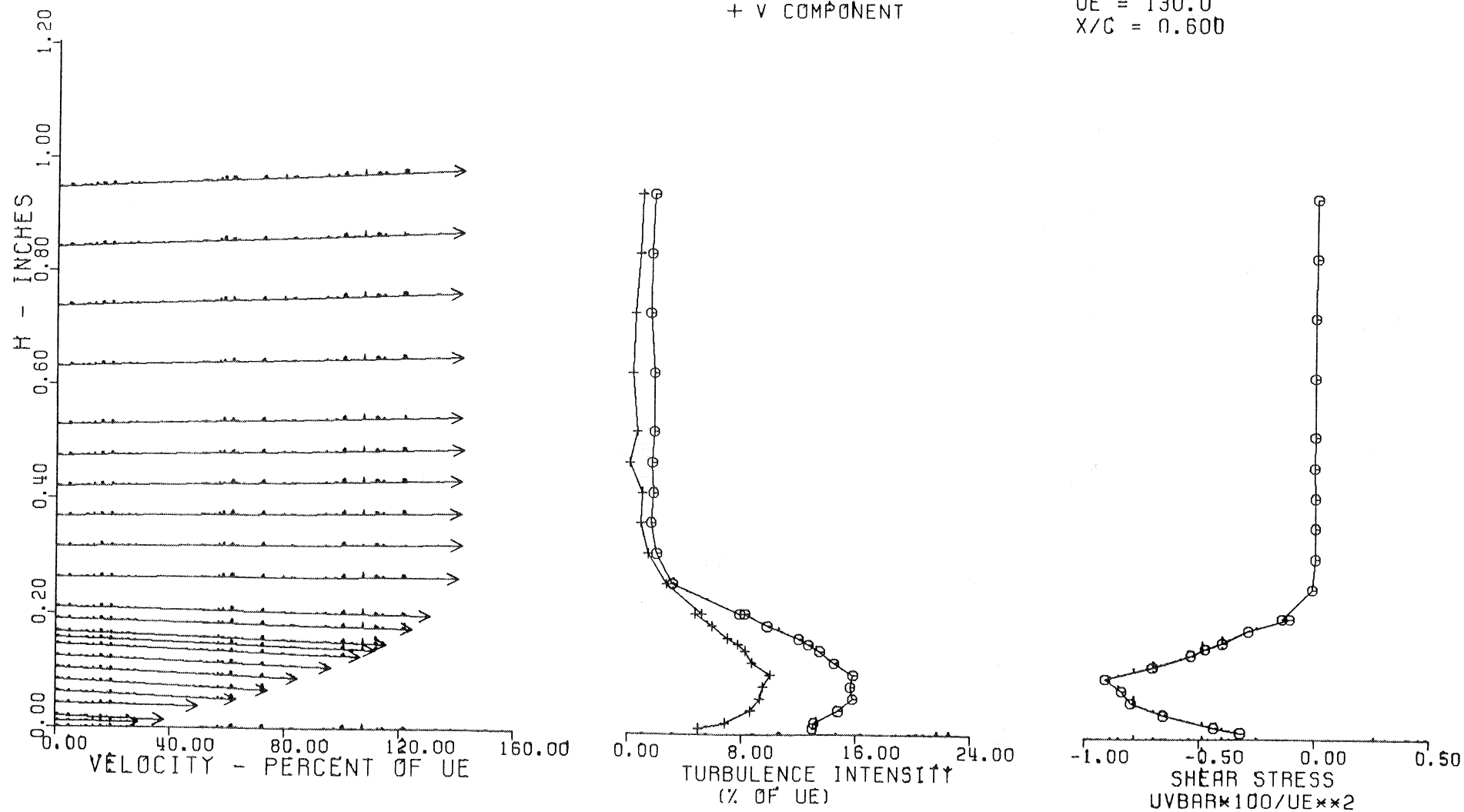


FIGURE 42. TYPICAL PLOT FORMAT FOR INDIVIDUAL PROFILES

LOCKHEED-GEORGIA COMPANY - LASER VELOCIMETER SURVEYS

GAW-1W F=30 G=0.025 OH=0.0 S=42.5 G=0.015 OH=0.015 ALPHA=16.00 VELOCITY VECTORS

CONFIGURATION E-3

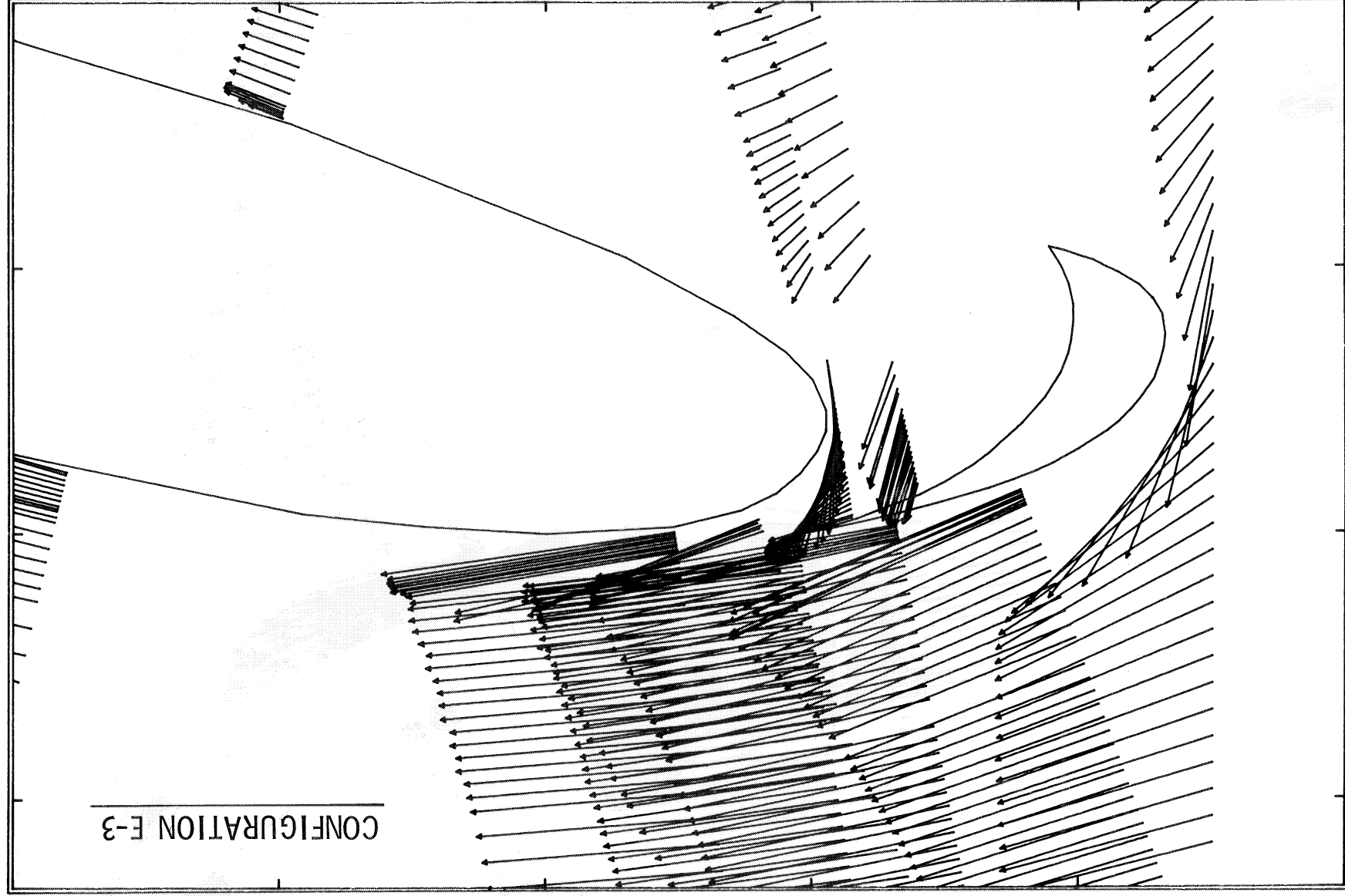


FIGURE 43(a). ENLARGEMENT OF LEADING EDGE SLAT FLOW-FIELD, $\alpha = 16^\circ$

LOCKHEED-GEORGIA COMPANY - LASER VELOCIMETER SURVEYS

GAW-1W F=30 G=0.025 OH=0.0 S=42.5 G=0.015 OH=0.015 ALPHA=16.00 VELOCITY VECTORS

CONFIGURATION E-3

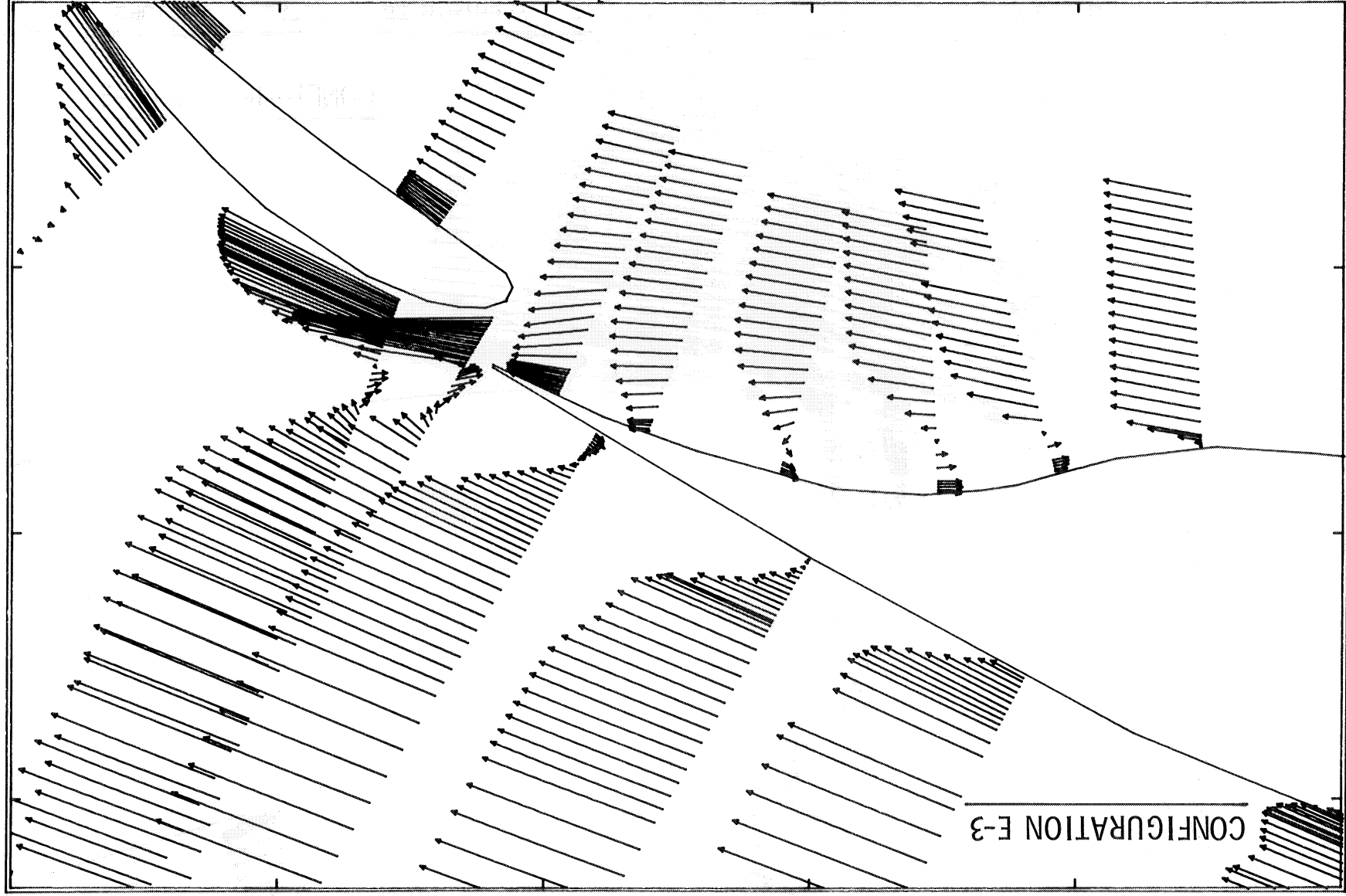


FIGURE 43(b). ENLARGEMENT OF TRAILING-EDGE SLOT FLOW-FIELD, $\alpha = 16^\circ$

LOCKHEED-GEORGIA COMPANY - LASER VELOCIMETER SURVEYS

GAW-1W F=0 S=27.0 G=.023 θ =.028 ALPHA=24.00 VELOCITY VECTORS

CONFIGURATION D-3

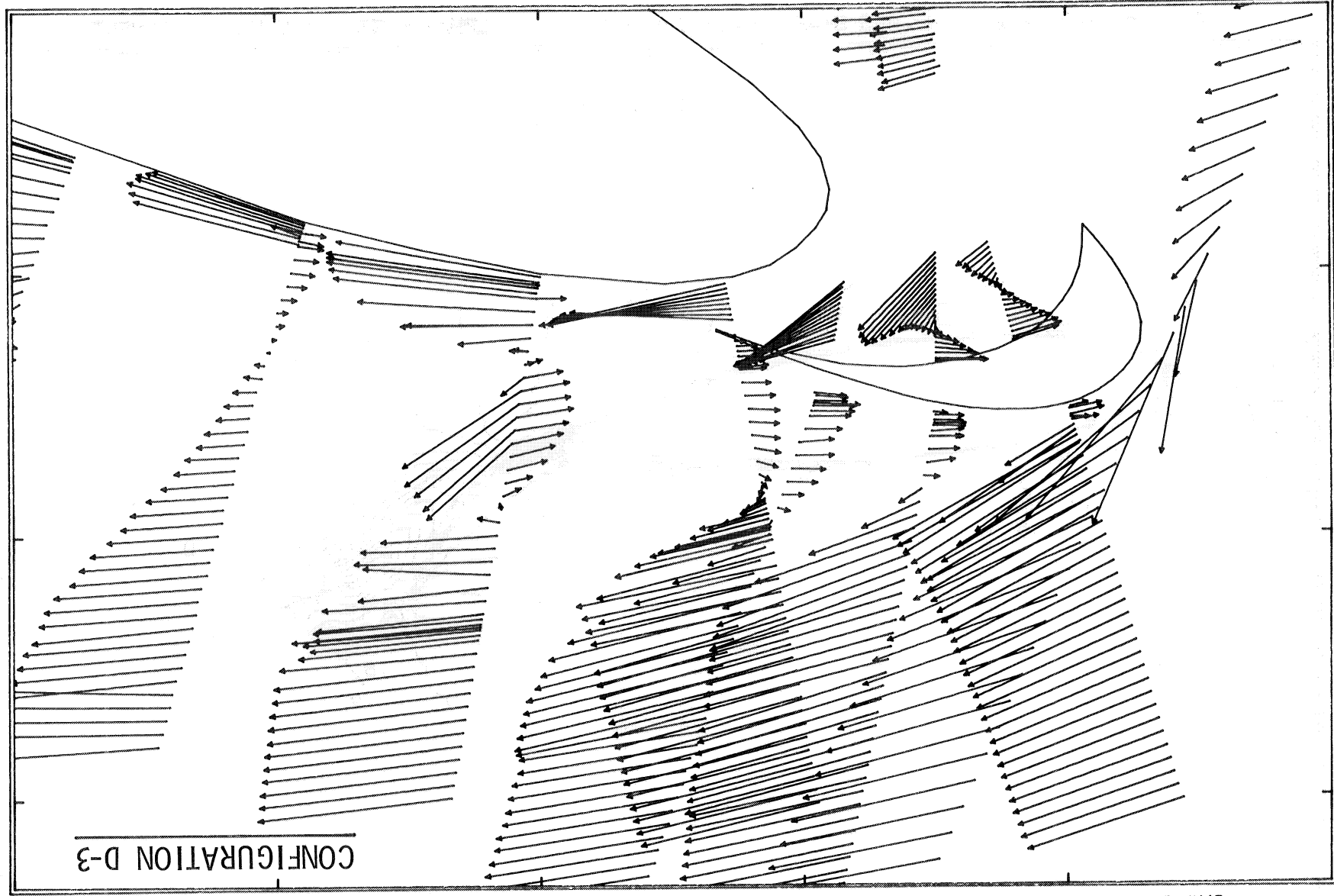


FIGURE 43(c). ENLARGEMENT OF LEADING-EDGE SLAT FLOW FIELD
EXHIBITING UNSTABLE FLOW, $\alpha = 24^\circ$

LOCKHEED-GEORGIA COMPANY - LASER VELOCIMETER SURVEYS

GAW-1W F-40 G-.015 OH-.025 S-42 G-.015 OH-.015 ALPHA= 6.00 U VEL COMPONENT

CONFIGURATION F-1

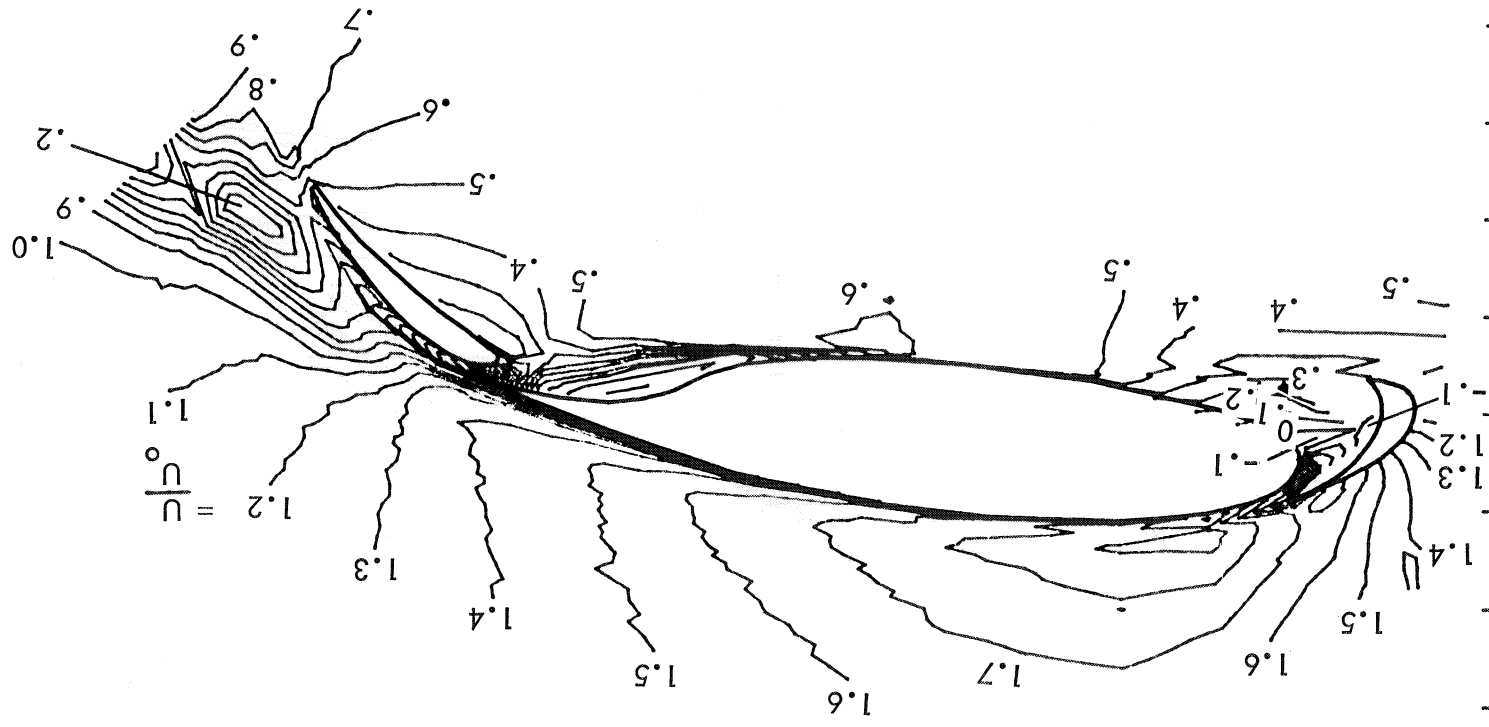


FIGURE 44(a). COMPOSITE PLOT OF STREAMWISE VELOCITY COMPONENT, u/u_0 , $\alpha = 6^\circ$

LOCKHEED-GEORGIA COMPANY - LASER VELOCIMETER SURVEYS

GAW-1W F-40 G-.015 OH-.025 S-42 G-.015 OH-.015 ALPHA= 6.00 V VEL COMPONENT

CONFIGURATION F-1

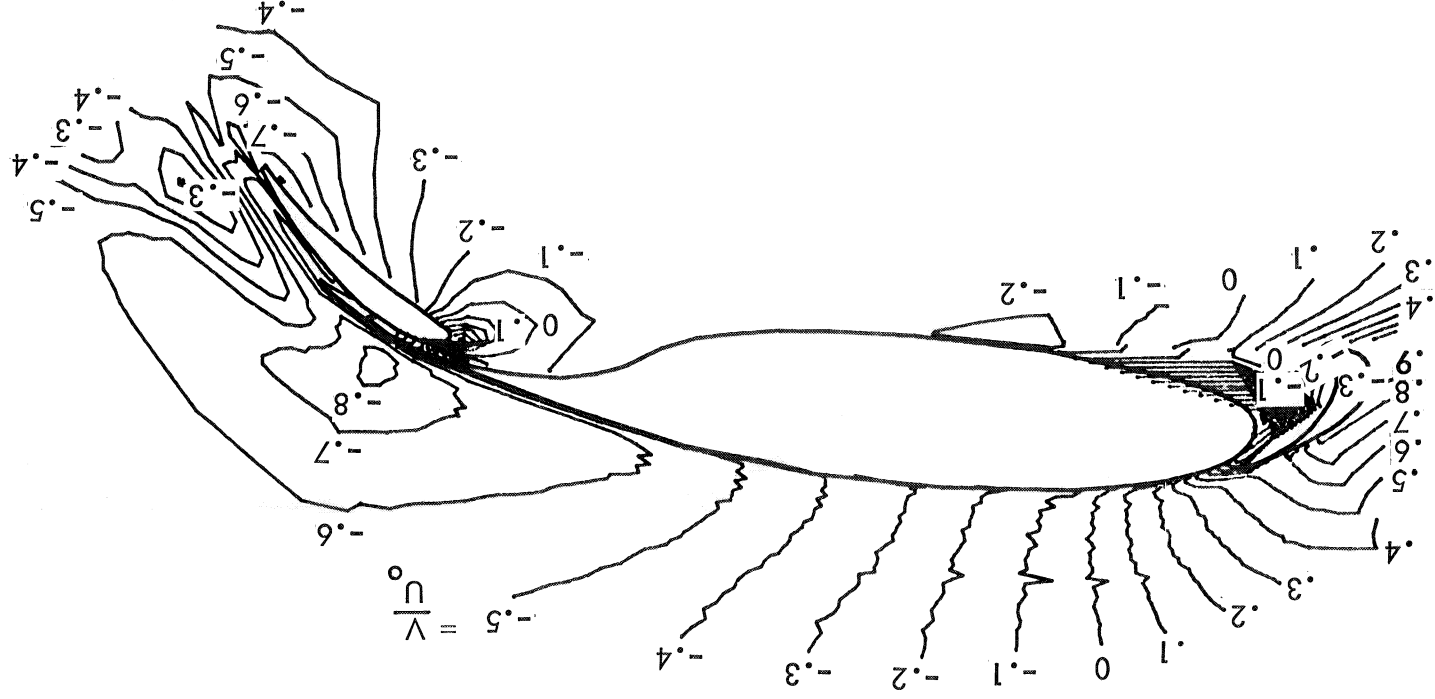


FIGURE 44(b). COMPOSITE PLOT OF NORMAL VELOCITY COMPONENT, v/u_0 , $\alpha = 6^\circ$

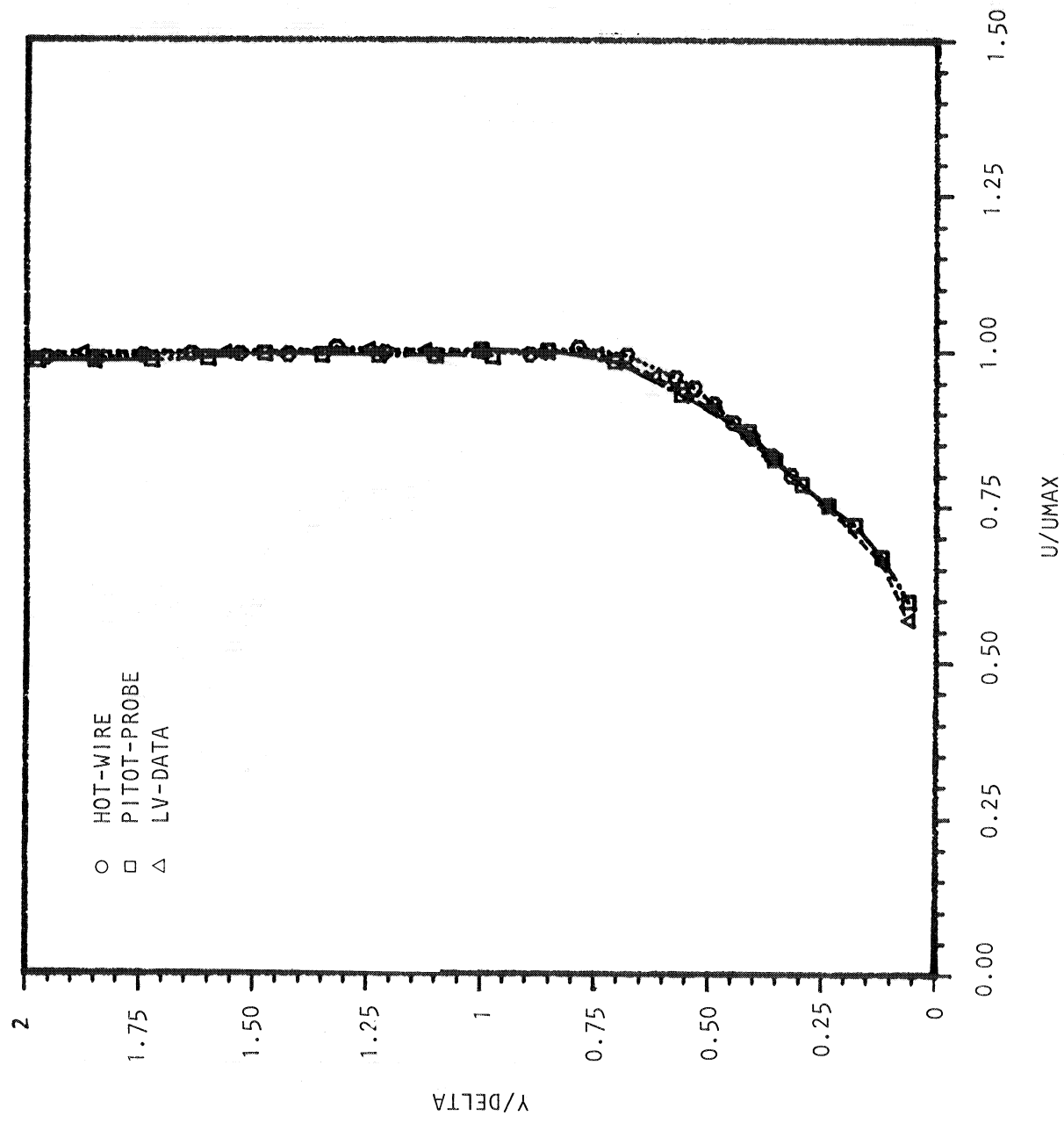


Figure 45(a) Comparison of LV-, Single-Element Hot-Wire and Pressure-Probe Velocity Profiles, Configuration C-1, $X/C = 0.60$ Main.

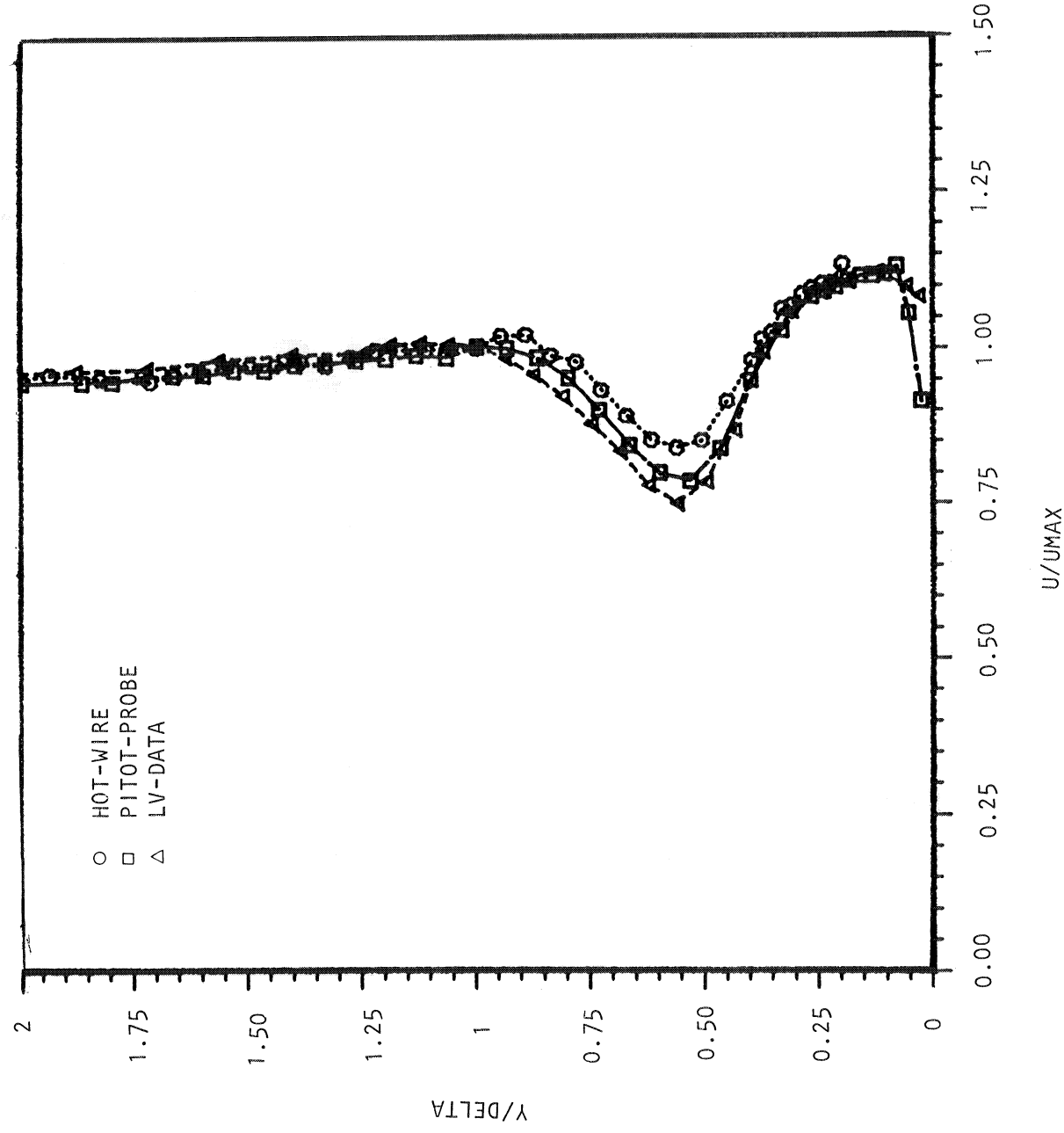


Figure 45(b). Comparison of LV-, Single-Element Hot-Wire and Pressure Probe Velocity Profiles, Configuration C-1, $X/C = 0.03$, Flap

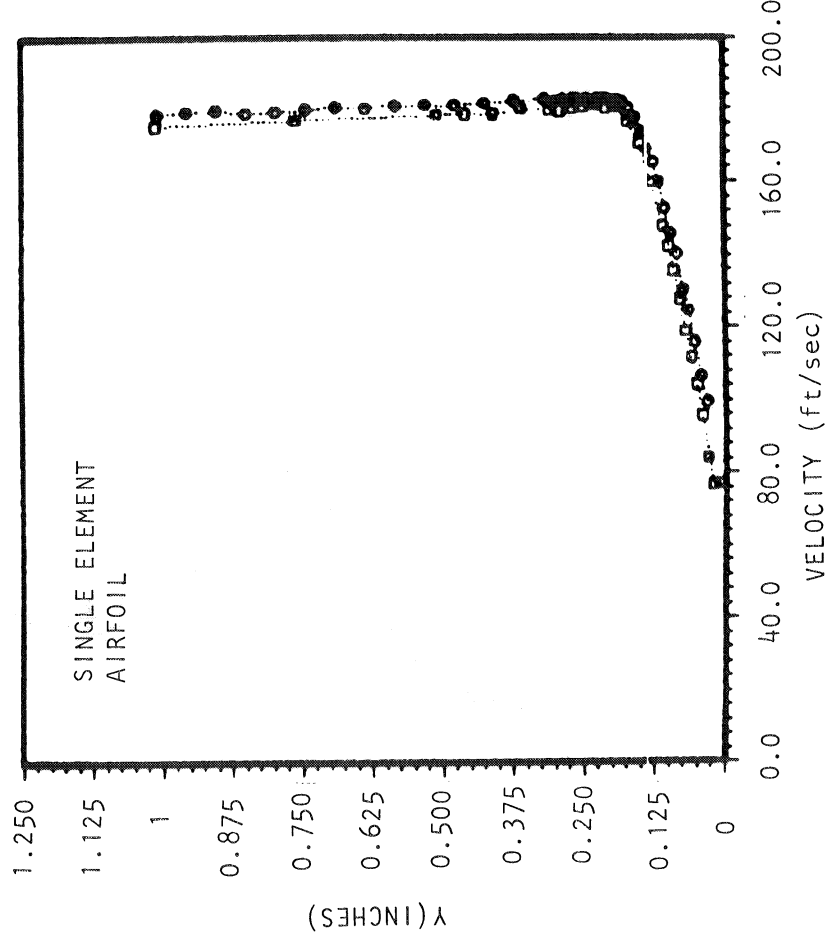
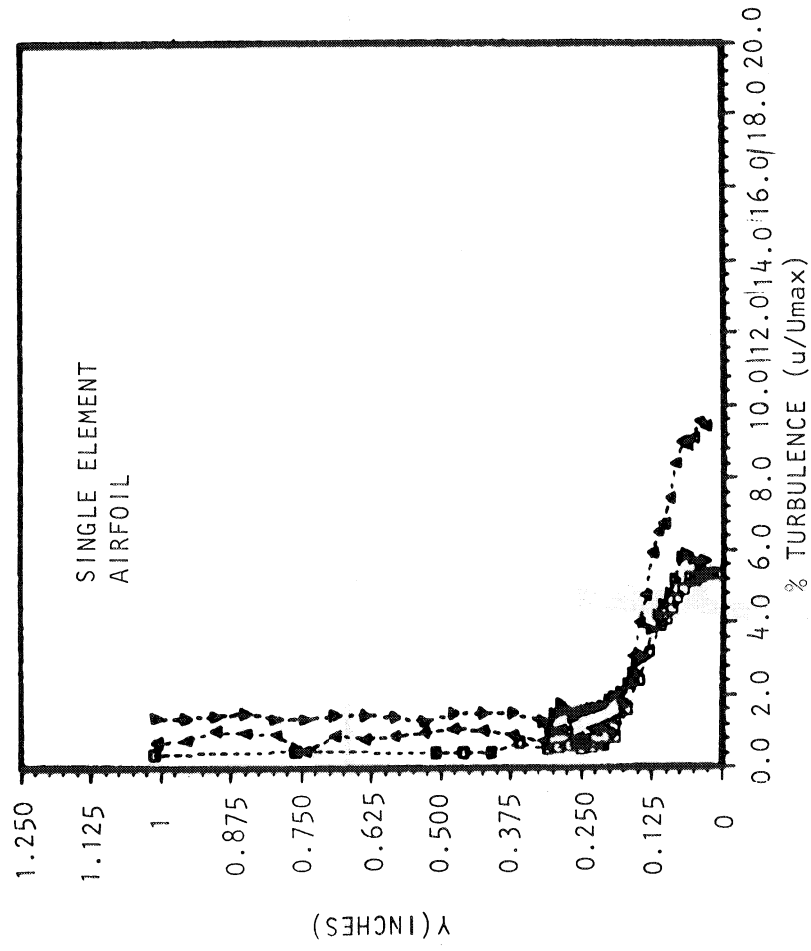
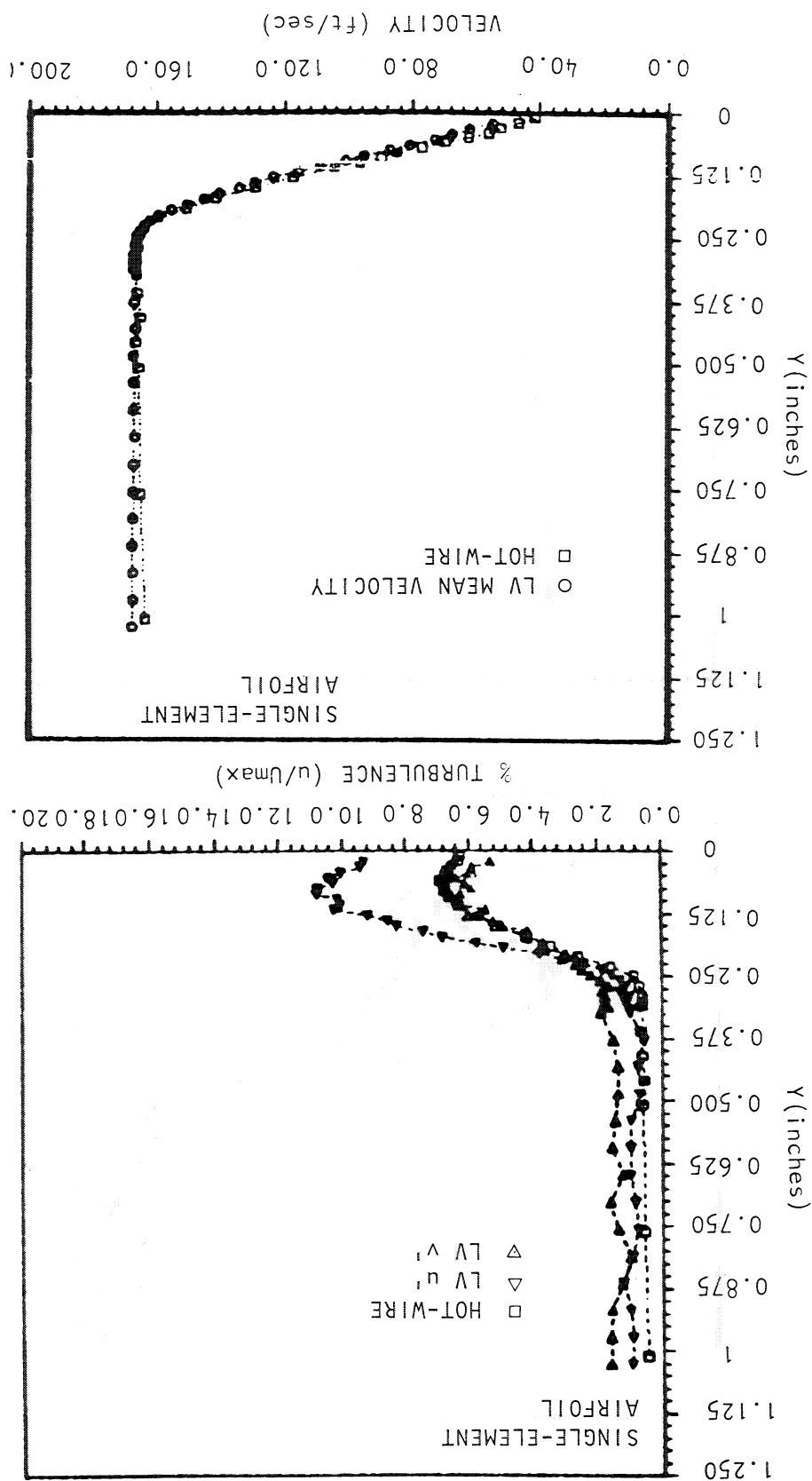


Figure 46(a) Comparison of LV- and Hot-Wire Mean and Turbulence Profiles in Boundary Layer; $X/C = 0.70$, Main

Figure 46(b) Comparison of LV- and Hot-Wire Mean and Turbulence Profiles
In Boundary Layer; $X/C = 0.80$, Main



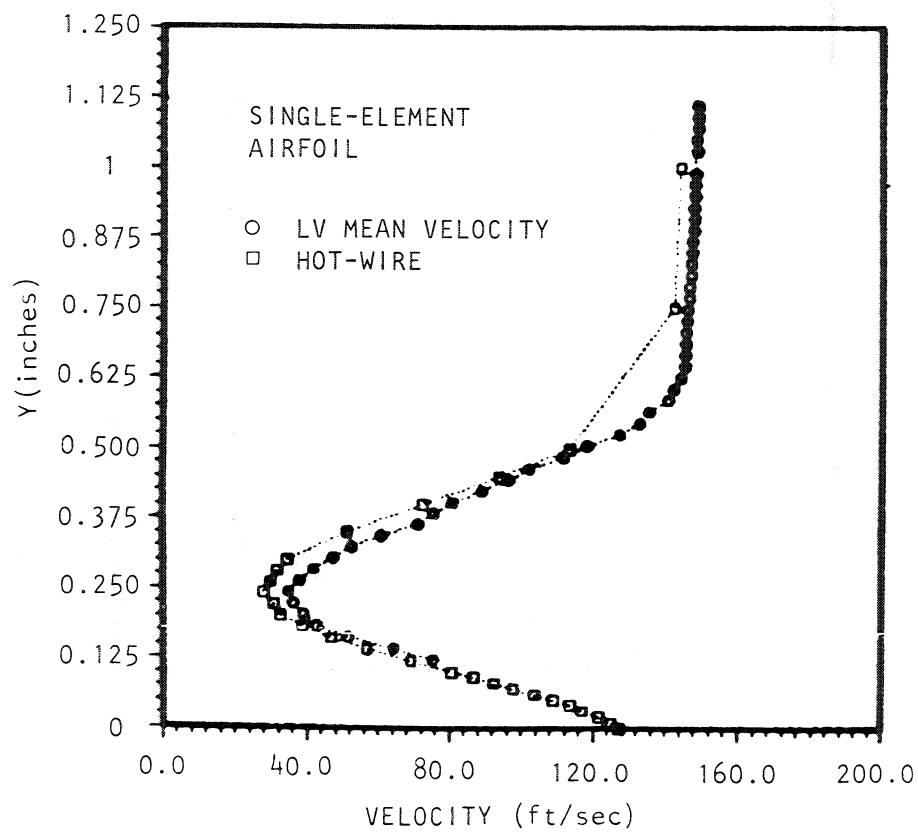
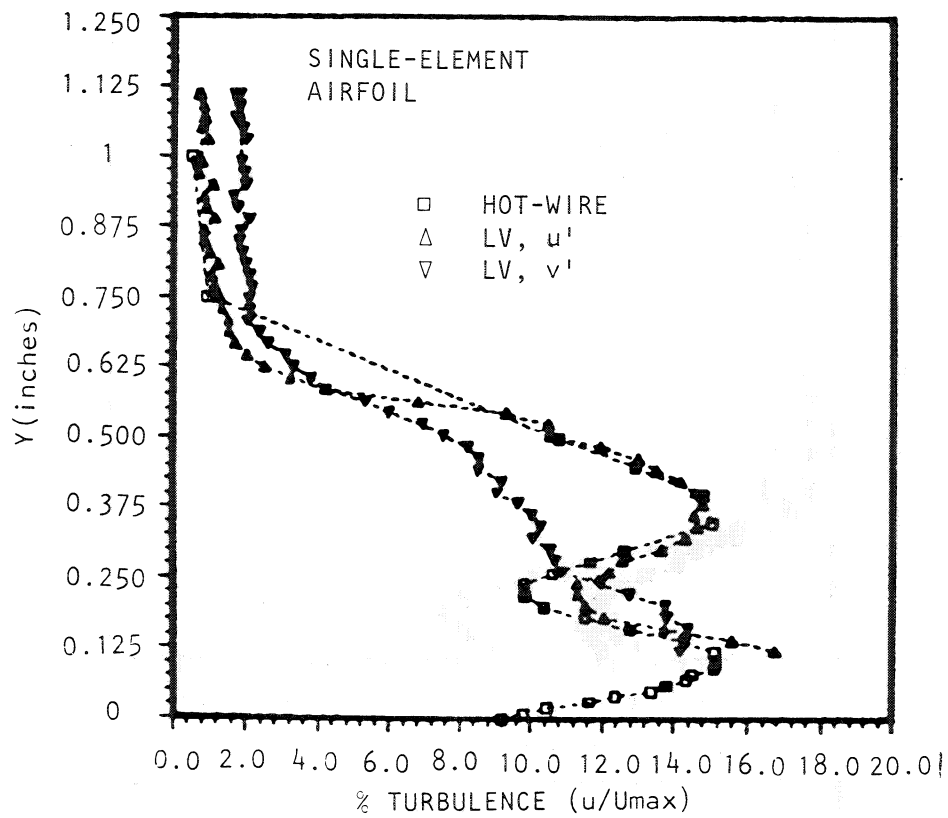


Figure 46(c) Comparison of LV and Hot-Wire Mean and Turbulence Profiles In Wake; $X/C = 1.10$, Wake

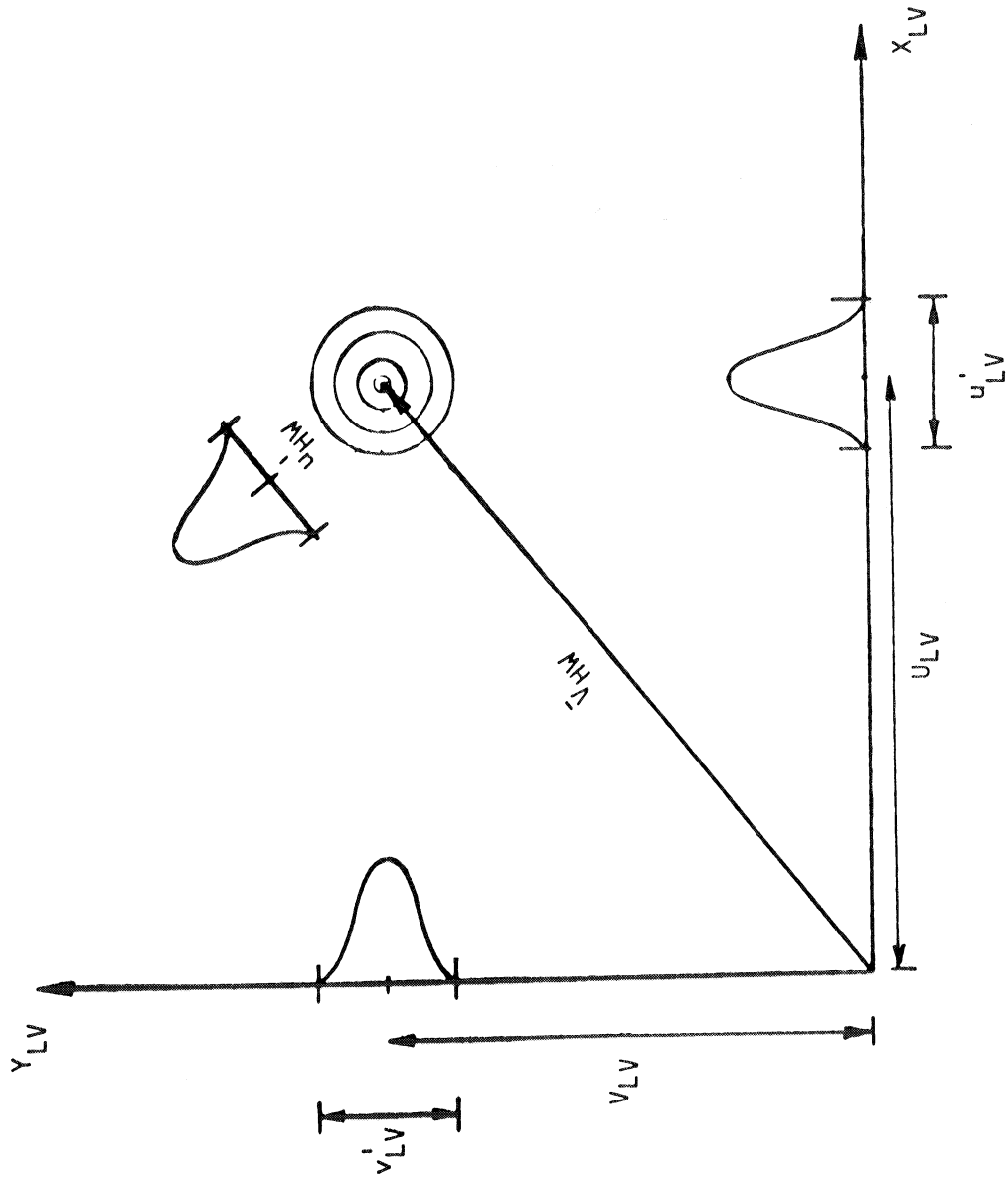


Figure 46(d) Histogram Comparison of LV- and Hot-Wire Measurement Techniques, for Large Mean Velocity with Isotropic Turbulence.

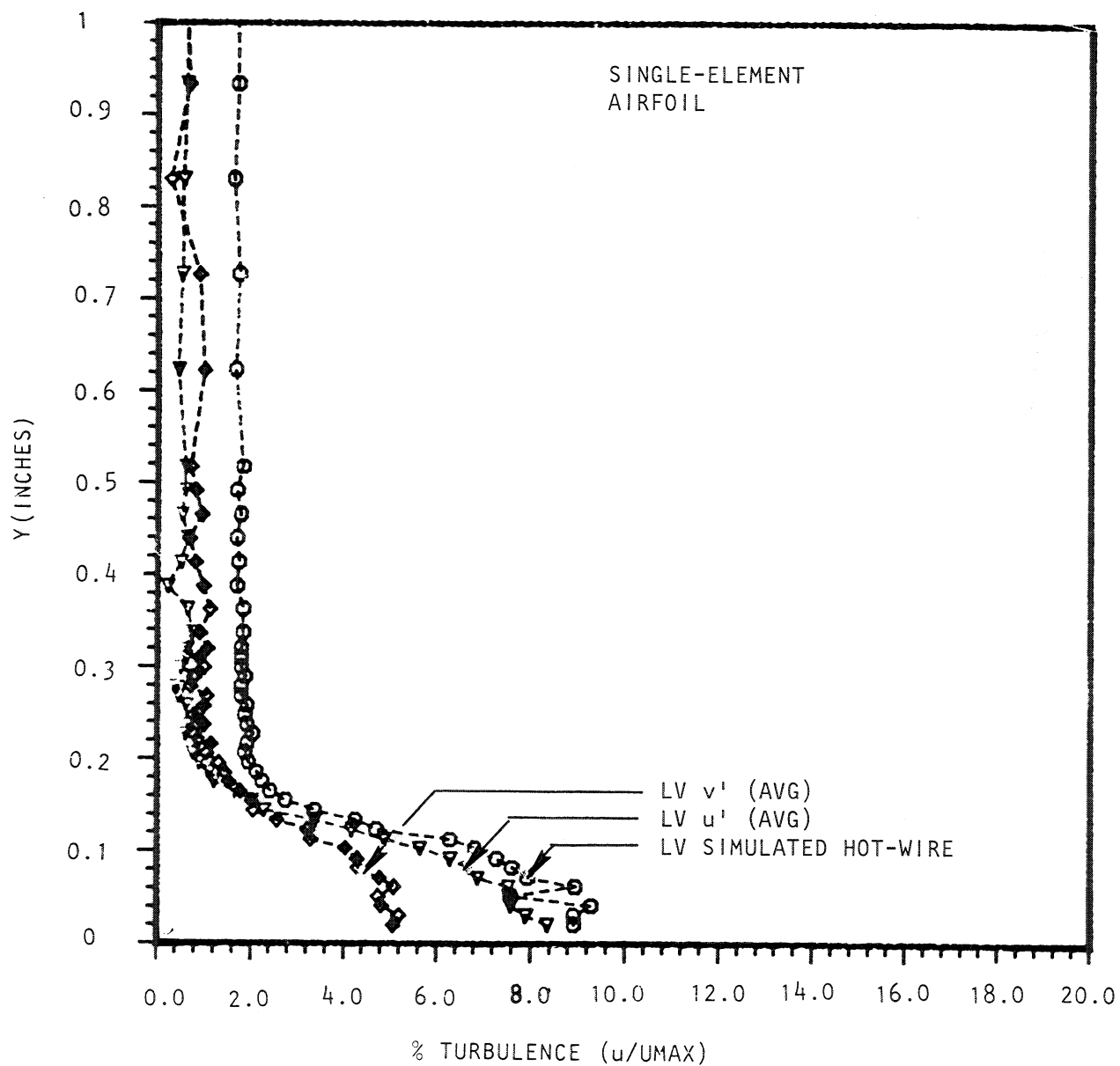


Figure 46(e). Effect of LV- u' and v' on Simulated Hot-Wire Signal, GAW-1, $X/C = 0.60$.

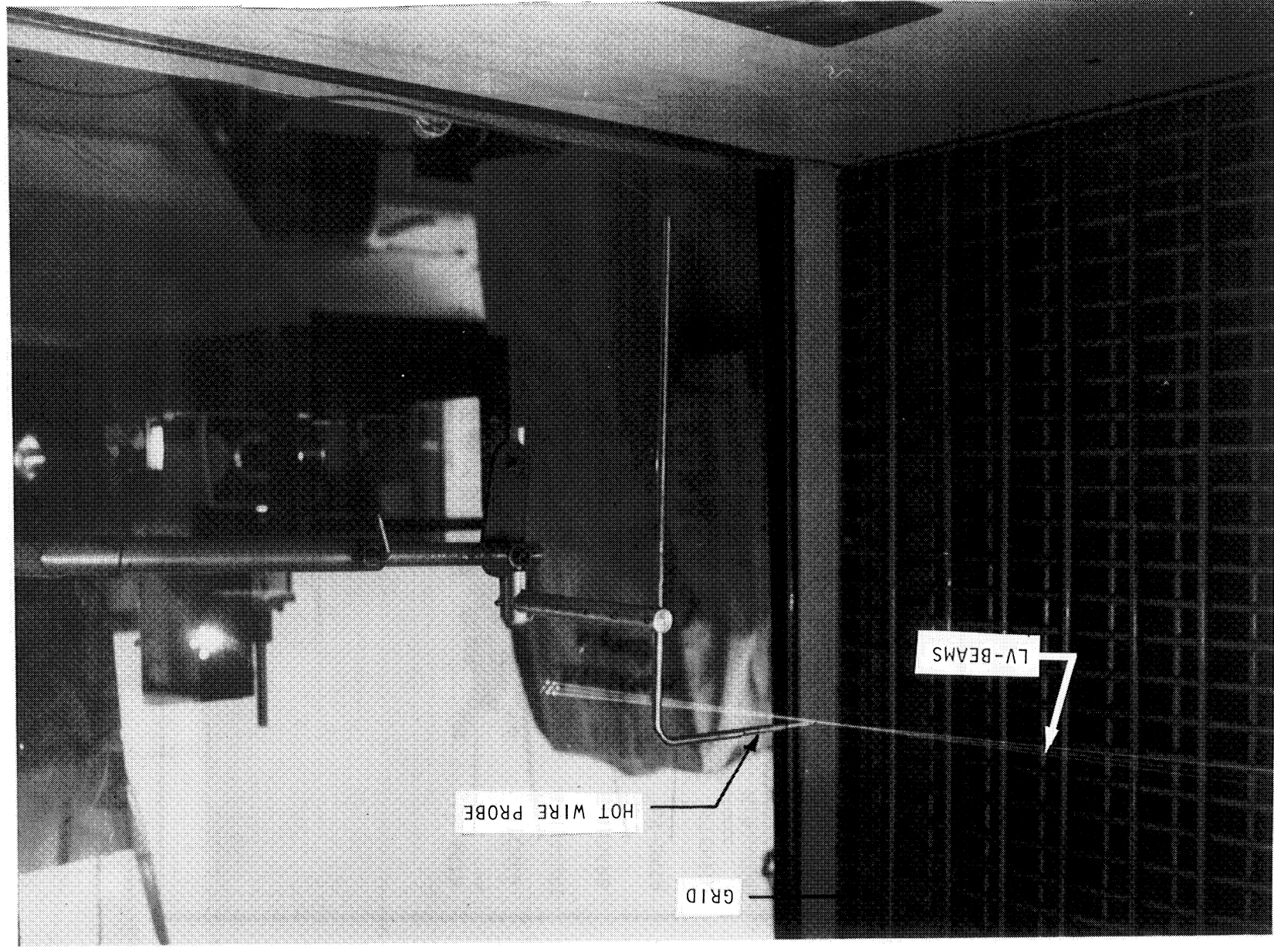


Figure 46(f). Uniform Grid Test Arrangement in ERF Wind-Tunnel

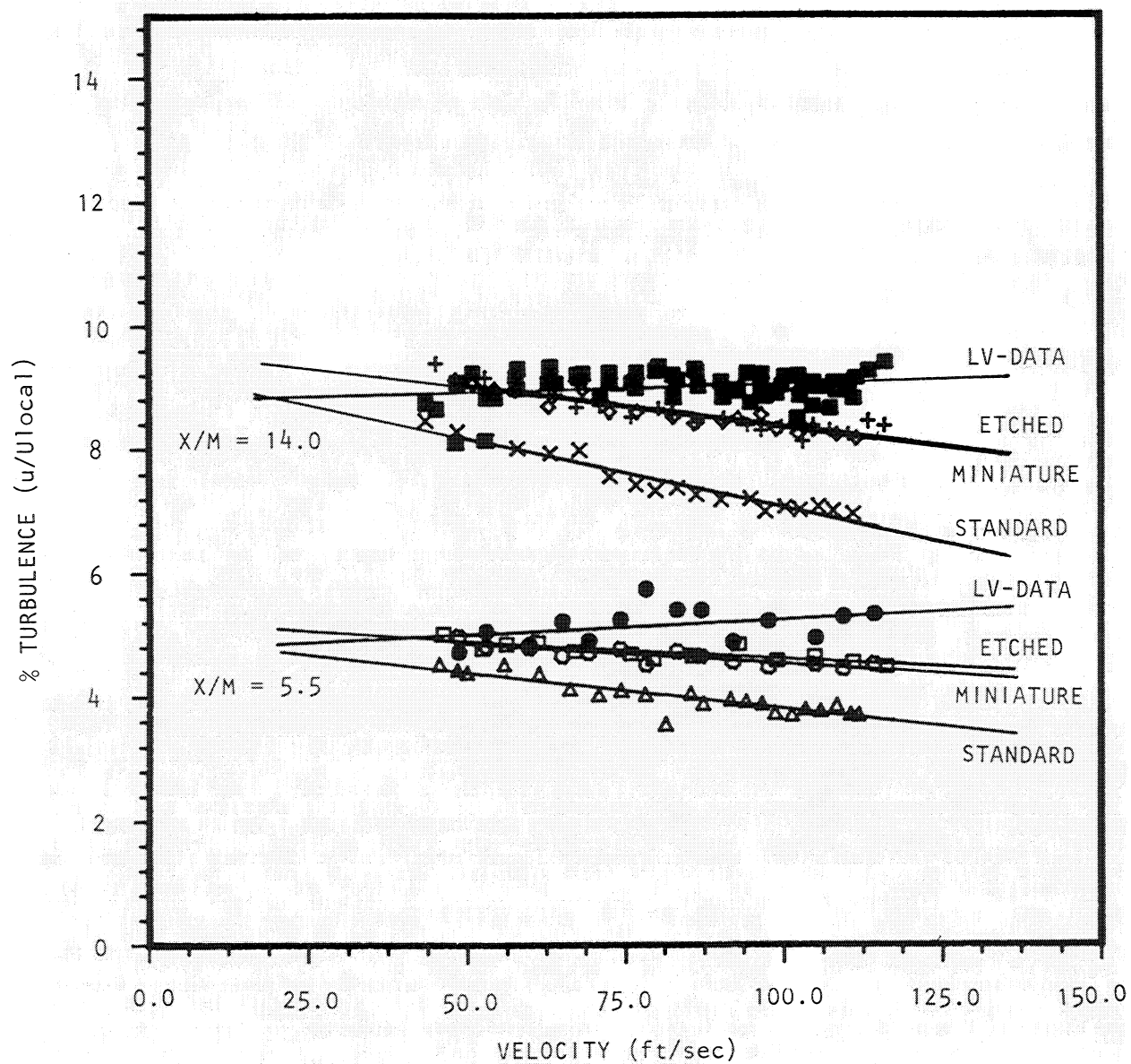


Figure 46(g) Effect of Spatial Resolution on Hot-Wire Measurement; Uniform Grid-Test.

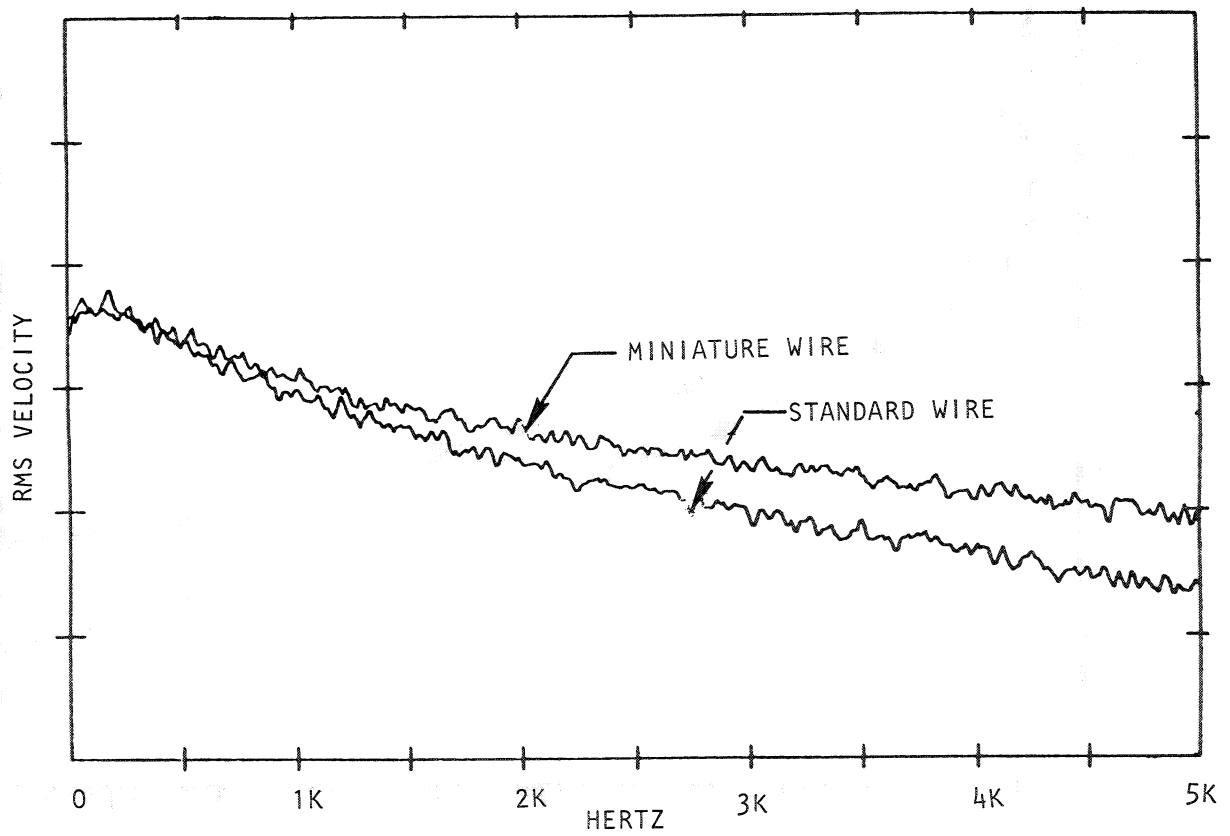


Figure 46(h). Log Linear Plot of RMS Spectra for Two Different Length Hot Wires @ $X/M = 14$ Behind Uniform Grid.

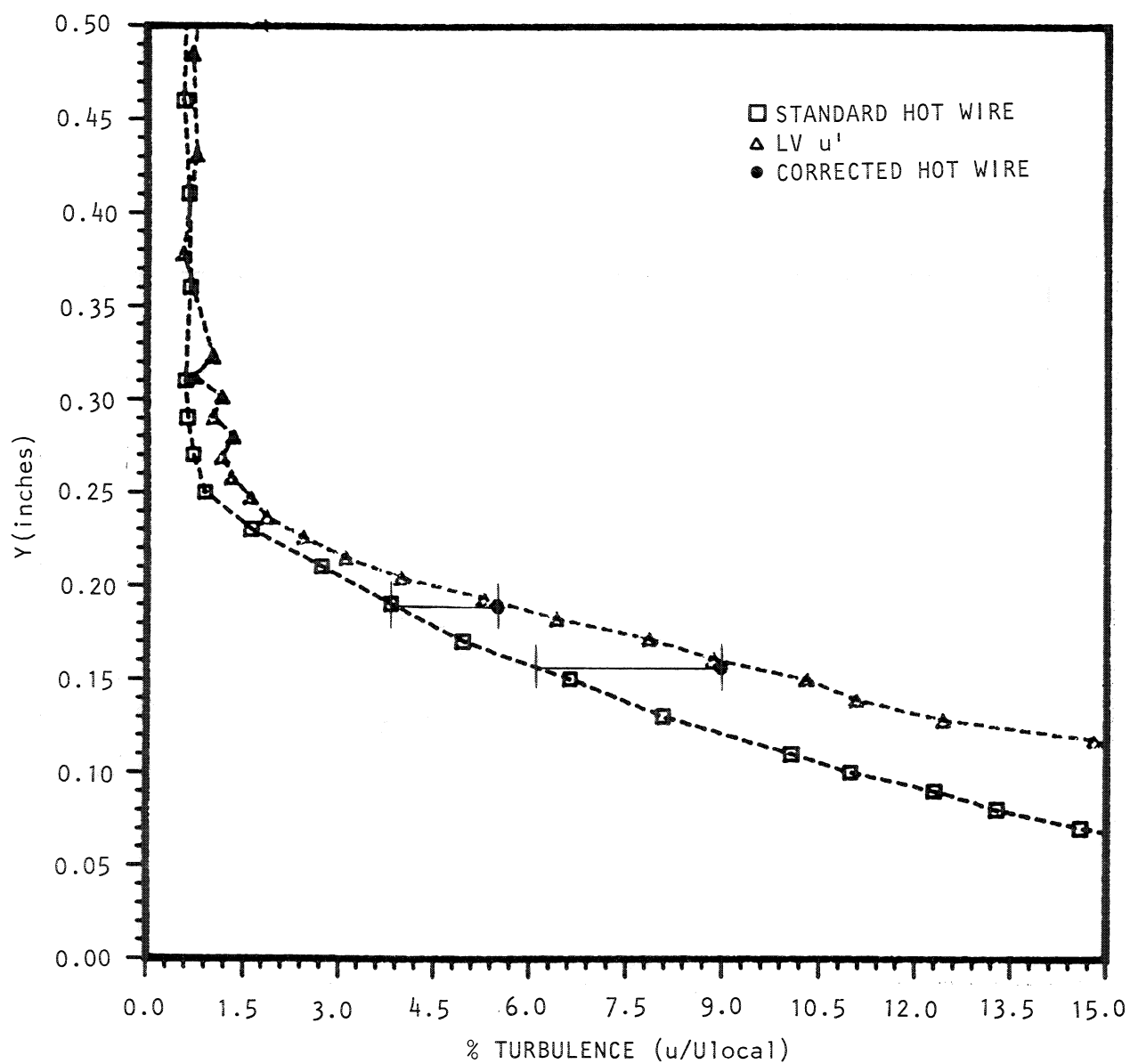


Figure 46(i). Effect of Spatial Resolution Corrections on GAW-1 Airfoil Turbulence Data.

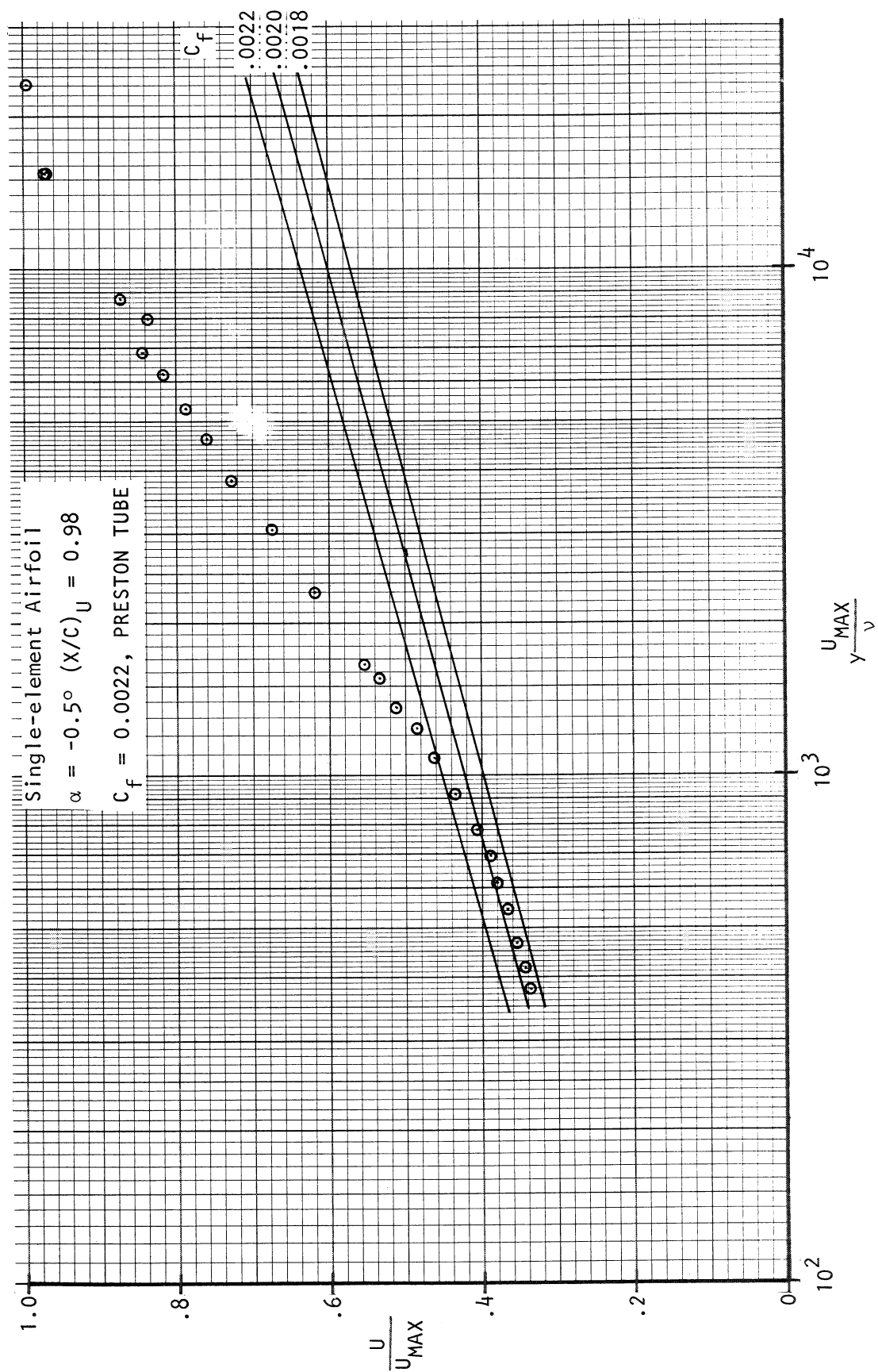
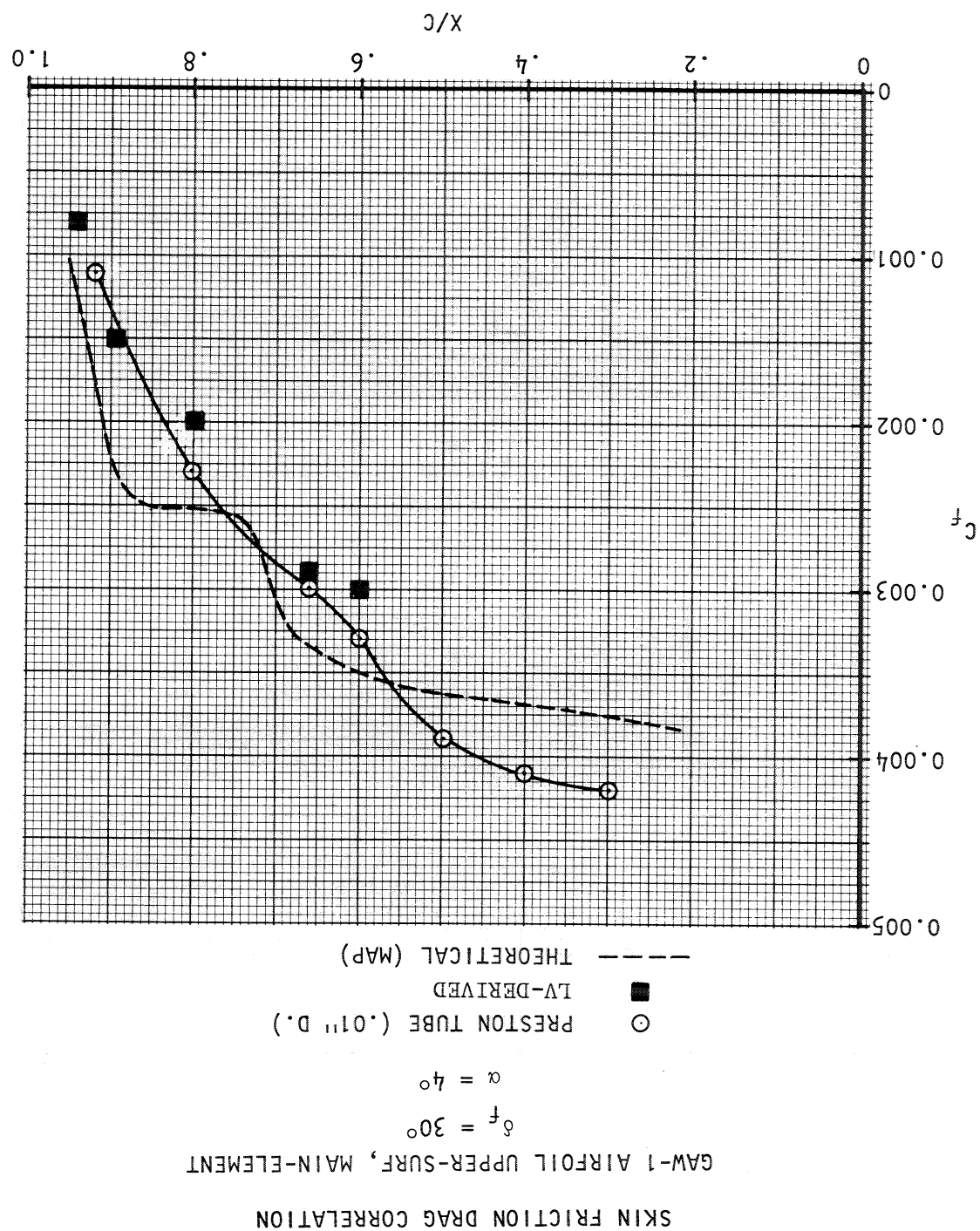


FIGURE 47. COMPARISON OF LV-DERIVED SKIN-FRICTION VALUE WITH PRESTON TUBE MEASUREMENT

FIGURE 48 SKIN-FRICTION EVALUATIONS ON CONFIGURATION B-1,
UPPER-SURFACES



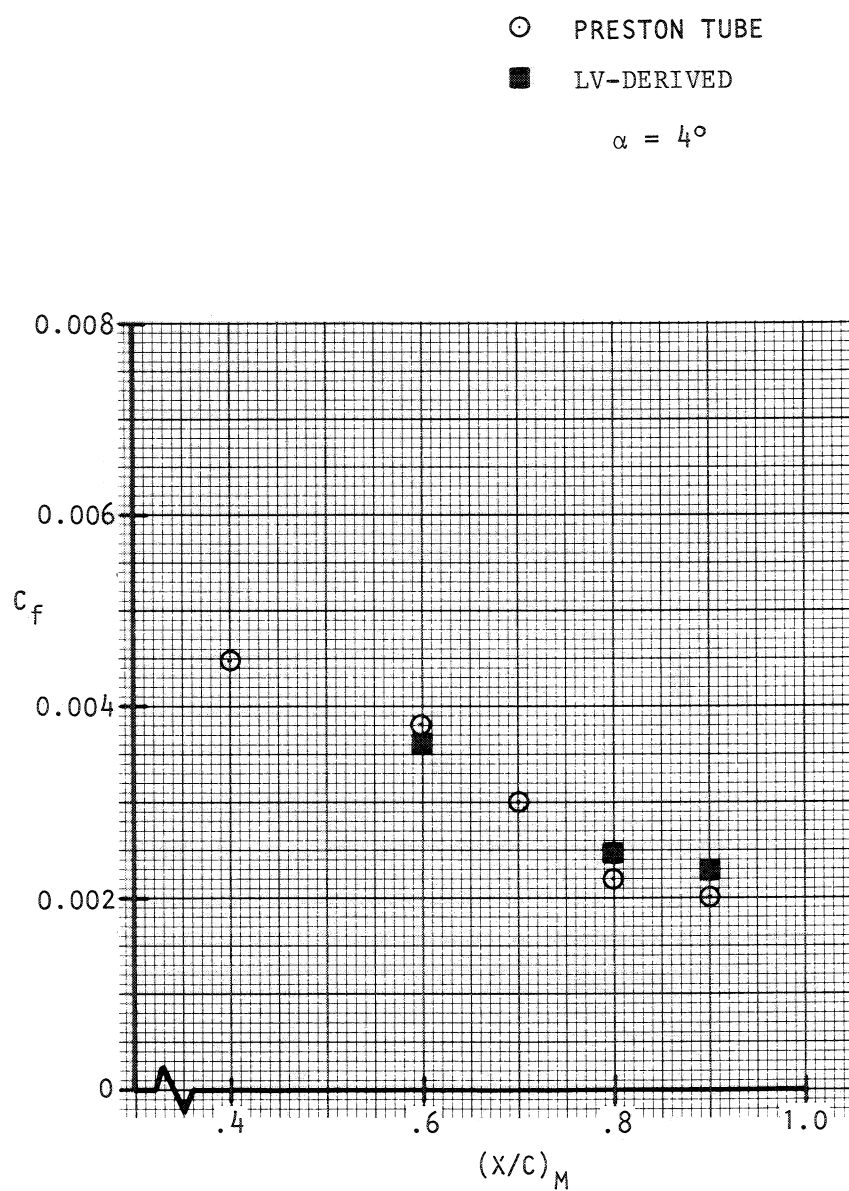


FIGURE 49.- SKIN-FRICTION MEASUREMENTS ON CONFIG. C-1,
UPPER-SURFACES

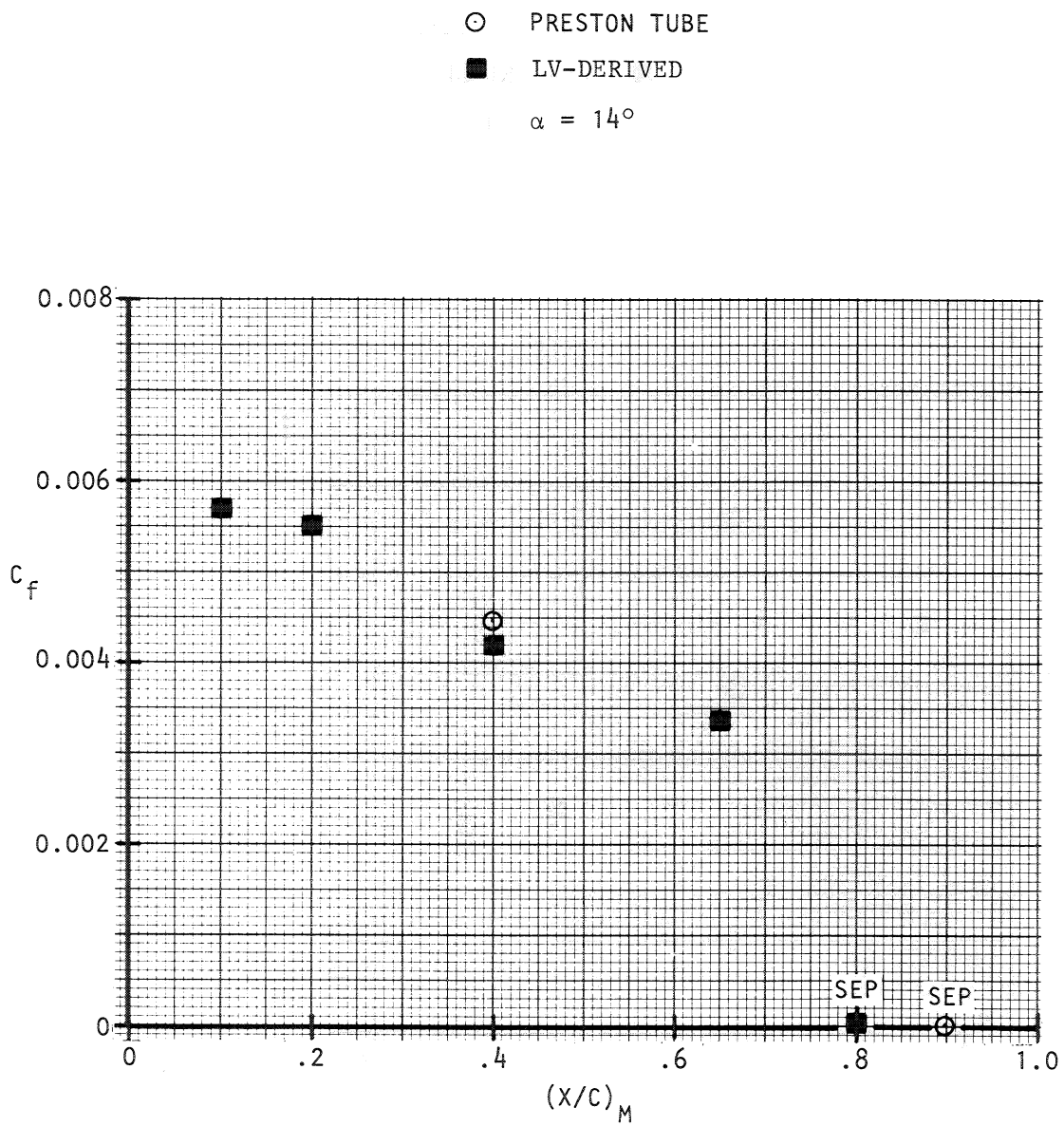


FIGURE 50.- SKIN-FRICTION EVALUATIONS ON CONFIG. F-3,
UPPER-SURFACES

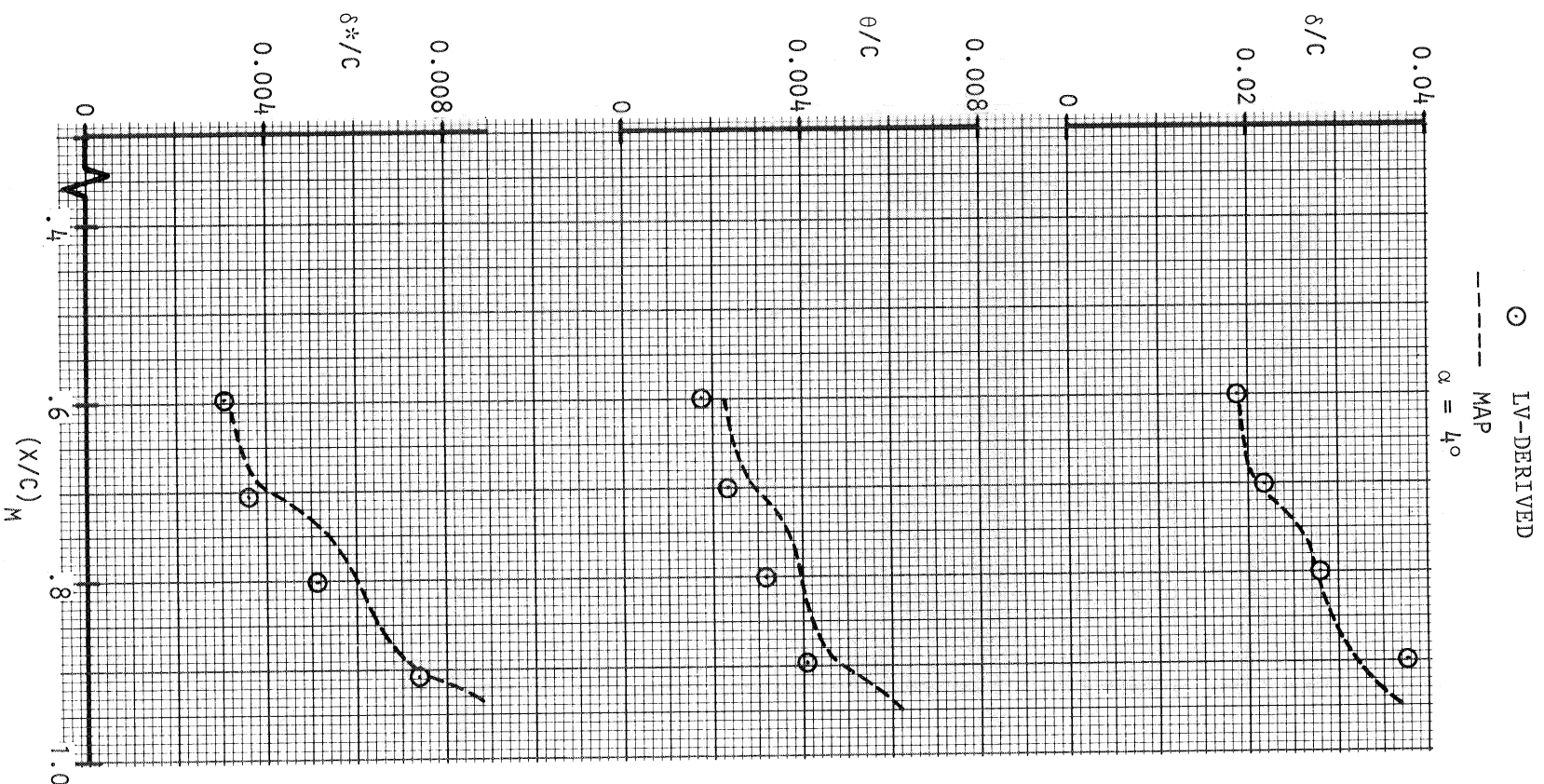


FIGURE 51 (a) COMPARISON OF LV-DERIVED ORDINARY BOUNDARY-LAYER PARAMETERS WITH CALCULATED; UPPER-SURFACE, CONFIG. B-4.

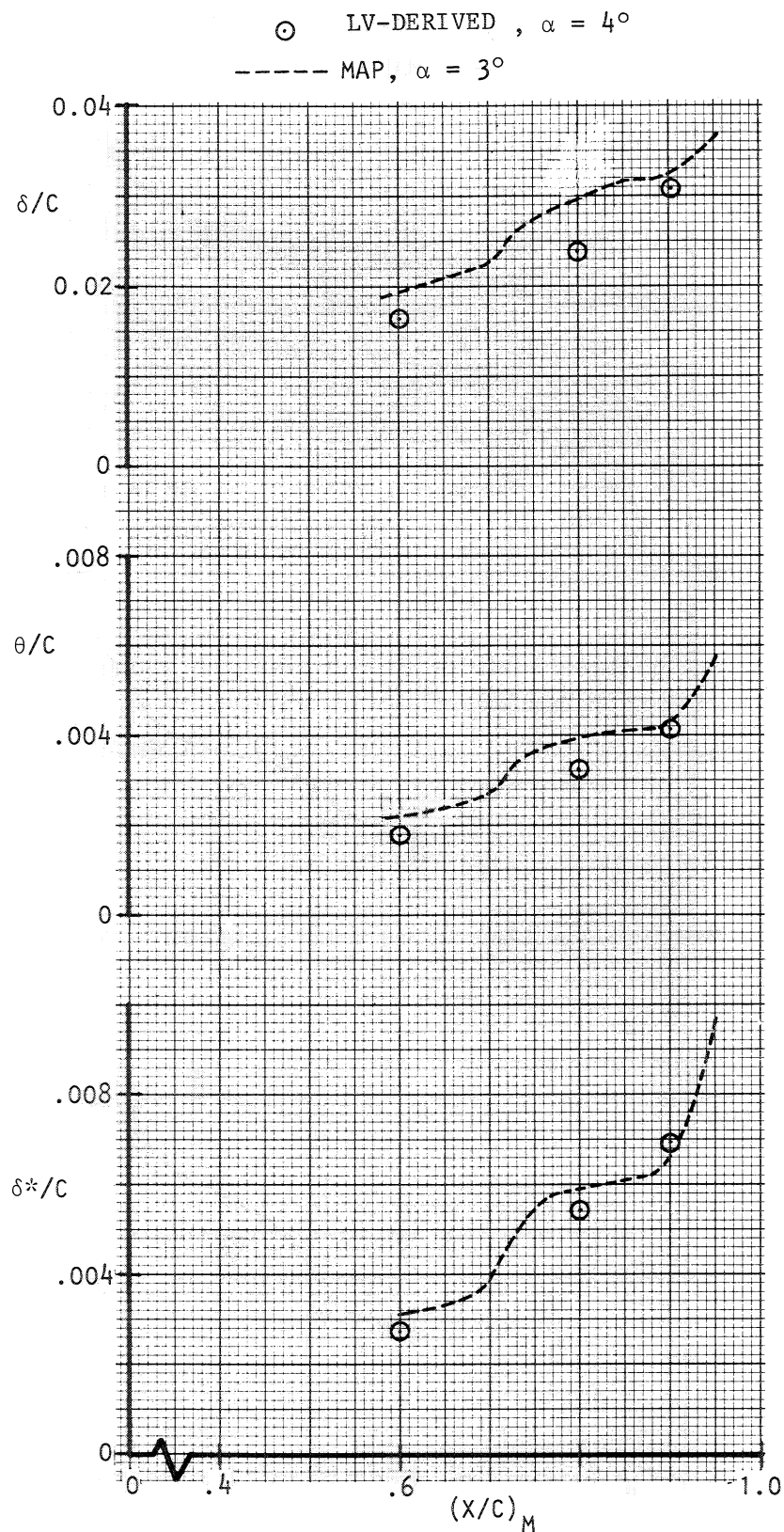
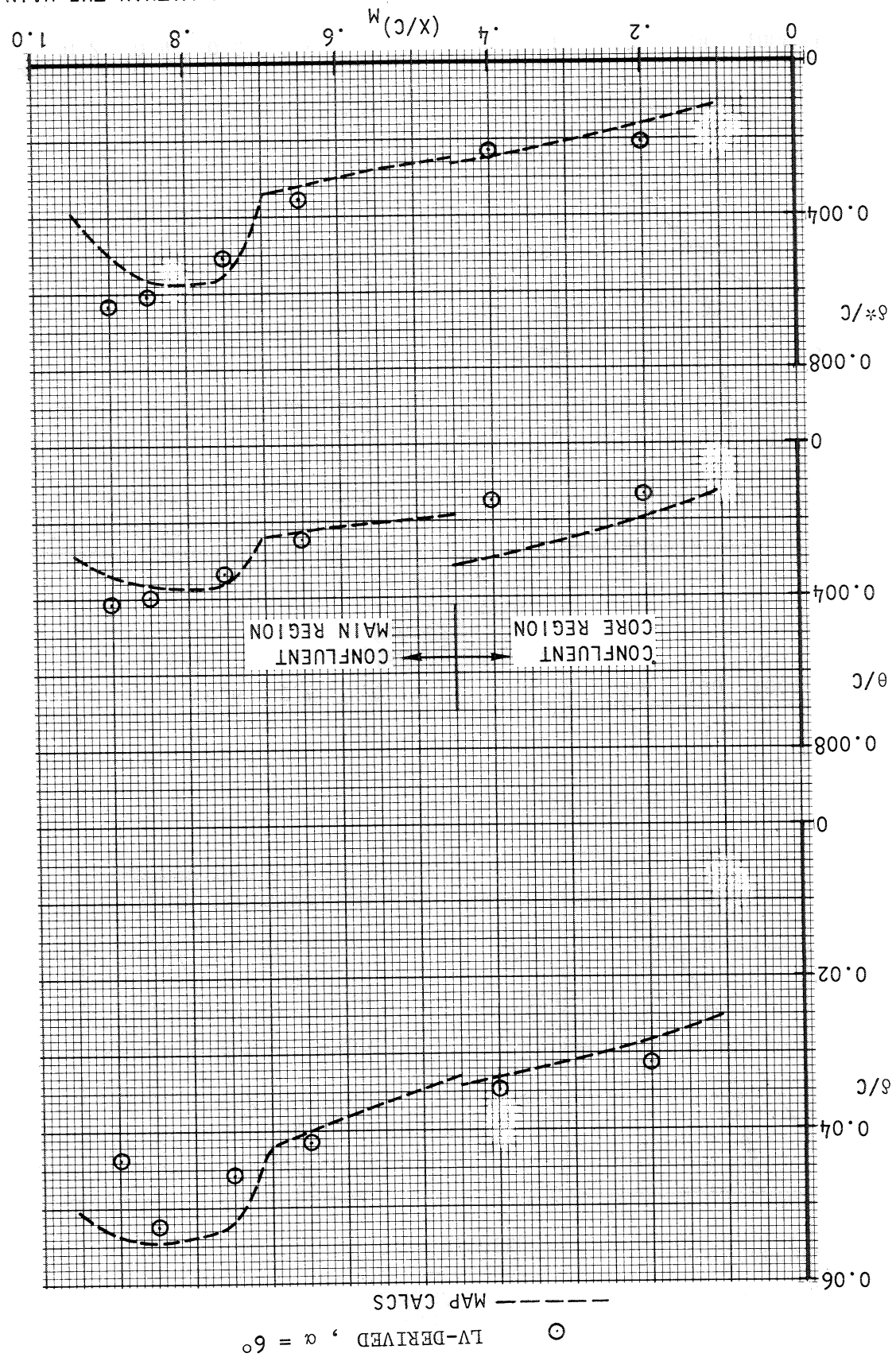


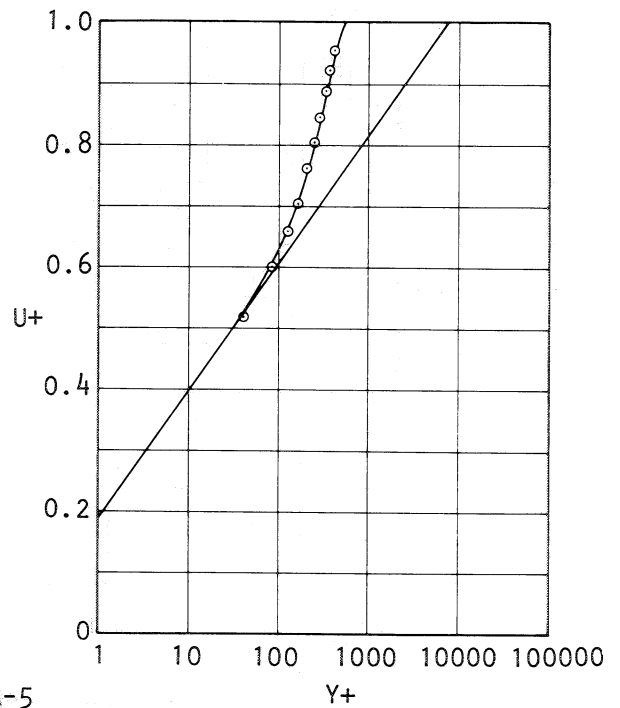
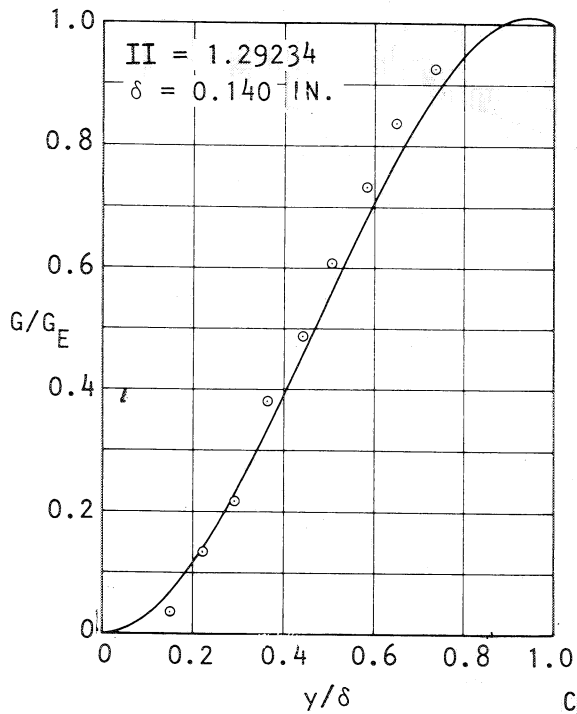
FIGURE 51(b) COMPARISON OF LV-DERIVED ORDINARY BOUNDARY-LAYER PARAMETERS WITH CALCULATED; UPPER-SURFACE, CONFIG. C-4.

FIGURE 51(c) COMPARISON OF BOUNDARY-LAYER PARAMETERS WITHIN THE MAIN-ELEMENT CONFLUENT REGION OF CONFIG. F-11



Config. A-4
Run 36
 $X/c = 0.5000$
 $C_f = 0.00280$

⊙ MEASURED
— CALCULATED



Config. A-5
Run 67
 $X/c = 0.5000$
 $C_f = 0.00110$

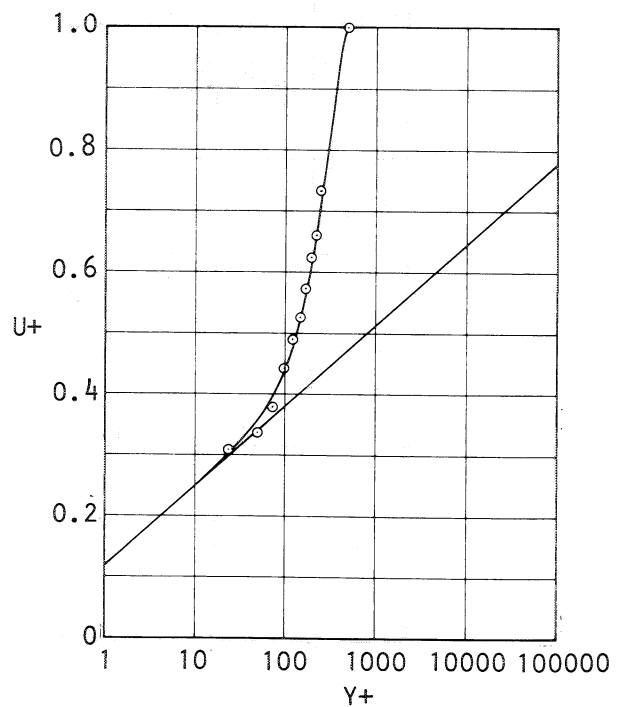
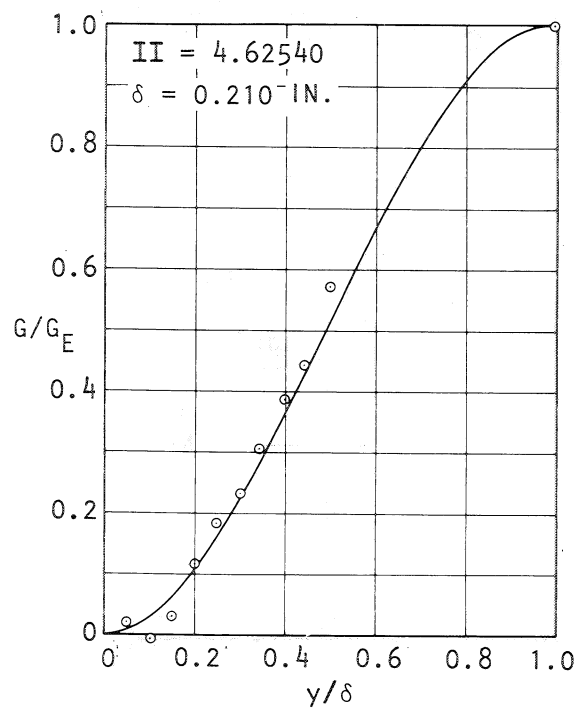
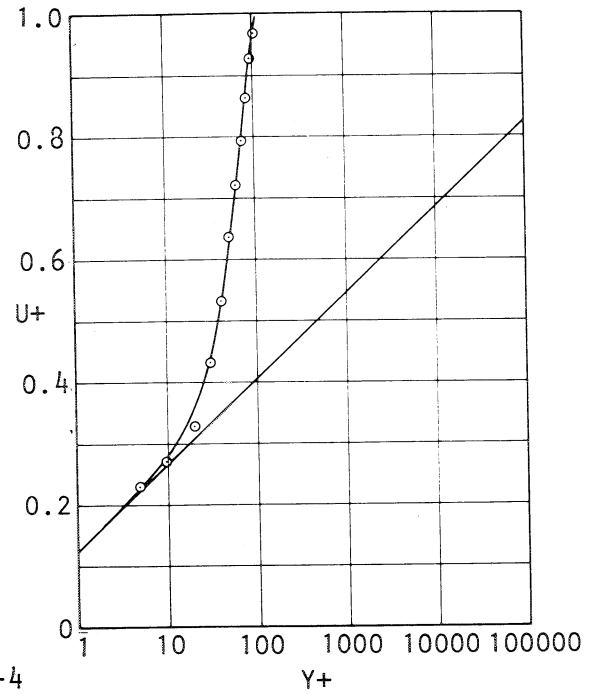
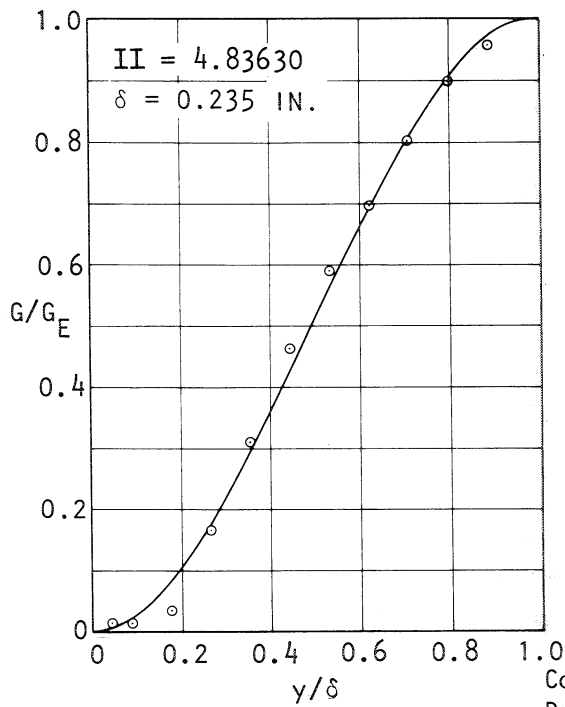


Figure 52(a). Comparison of "Law-of-The-Wake" Calculations with LV-Measured Velocity Profiles, GAW-1 Airfoil.

Config. C-3
Run 97
 $X/c = 0.6000$
 $C_f = 0.00124$

○ MEASURED
— CALCULATED



Config. B-4
Run 64
 $X/c = 0.8000$
 $C_f = 0.0024$

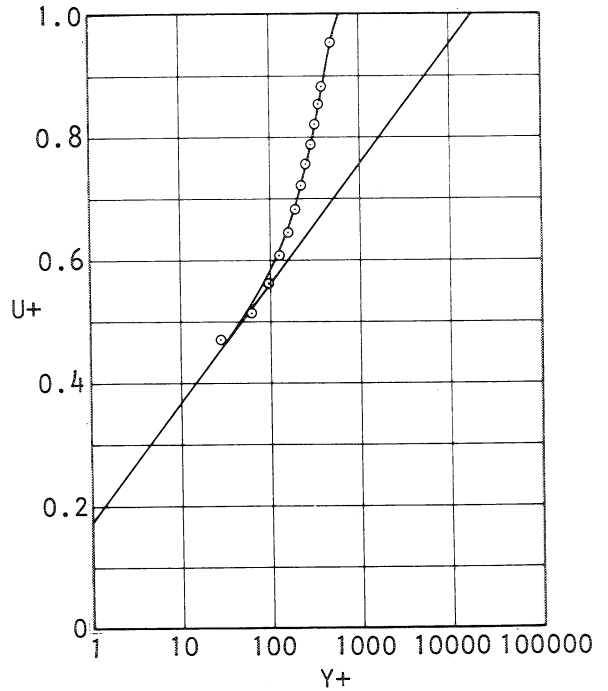
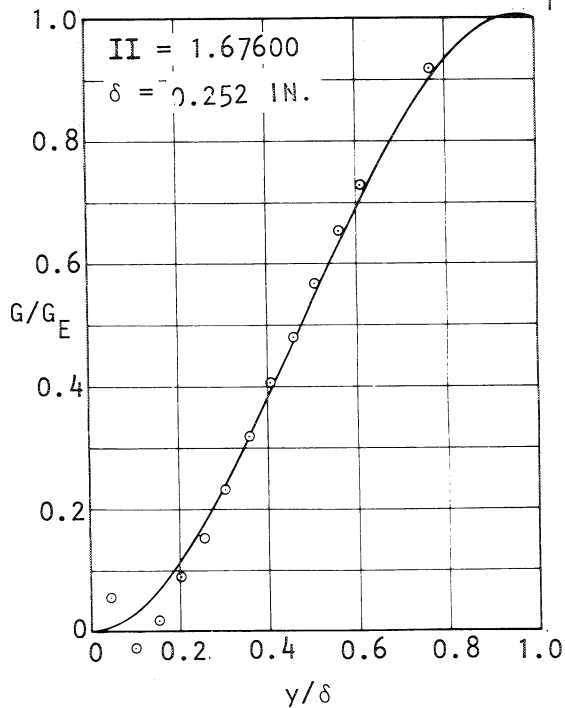


Figure 52(b). Comparison of "Law-of-The-Wake" Calculations With LV-Measured Velocity Profiles, GAW-1 Airfoil.

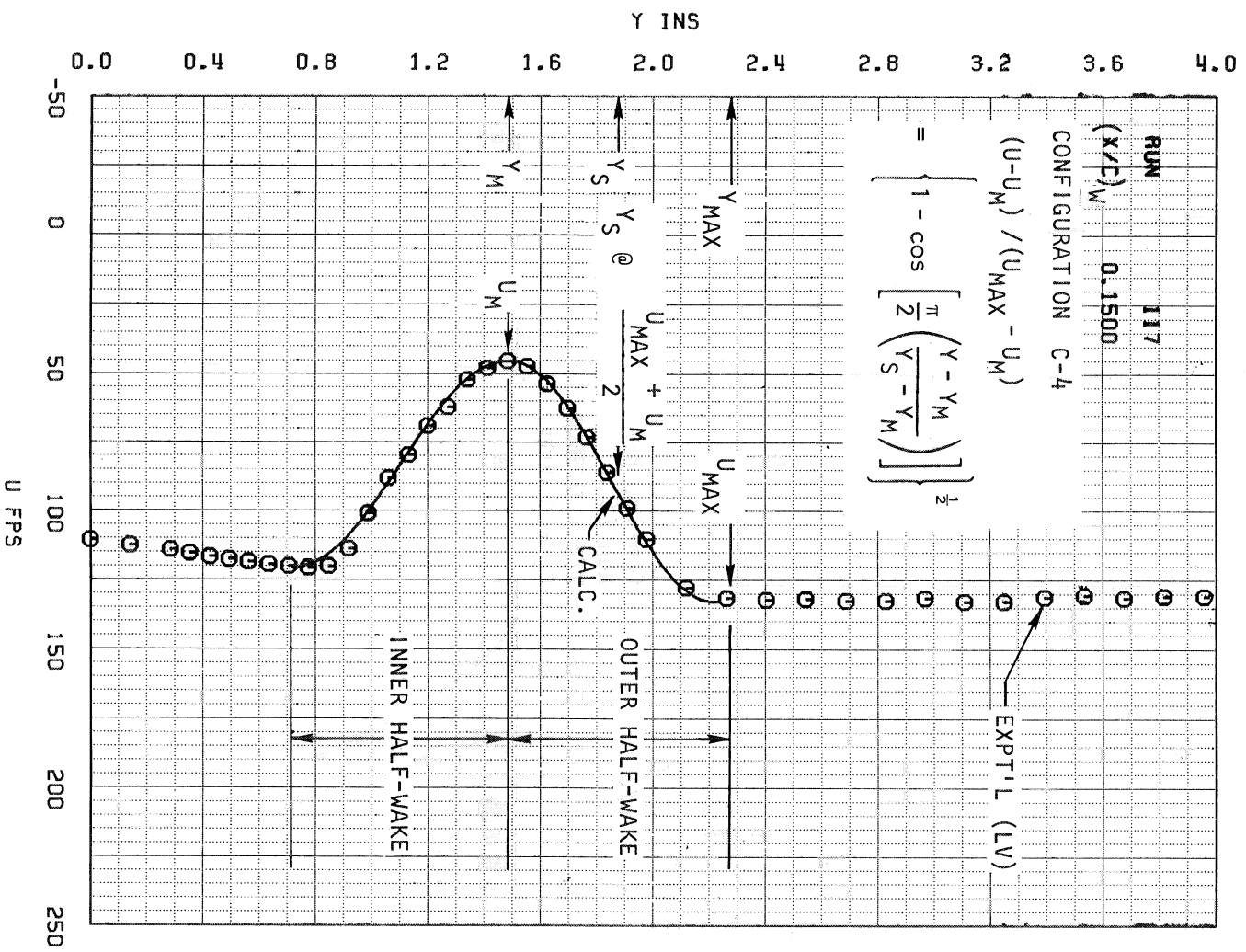


FIGURE 53 COMPARISON OF TYPICAL WAKE PROFILE TO VELOCITY DISTRIBUTION COMPUTATION

OUTER HALF-WAKE
LV-RUNS

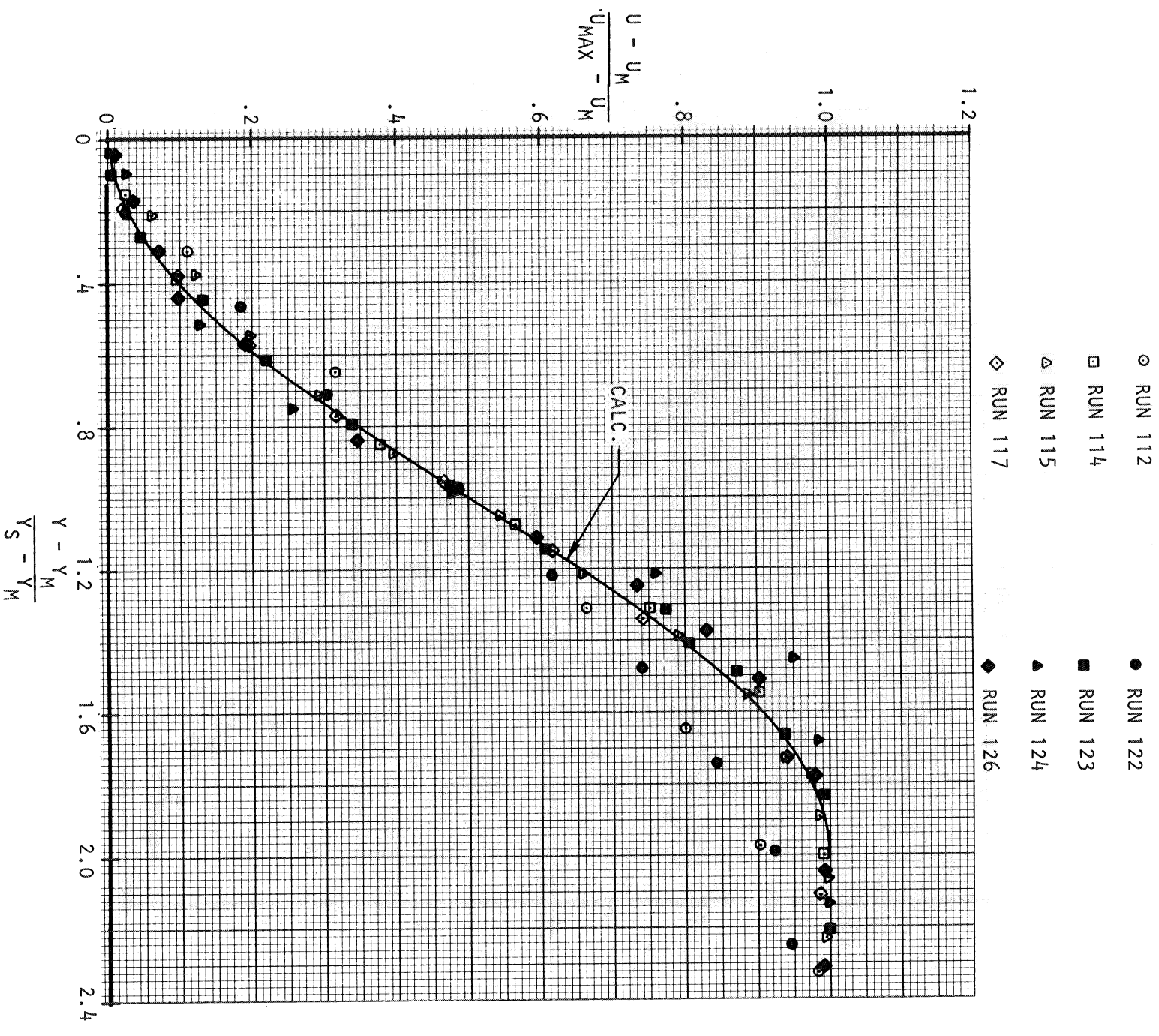
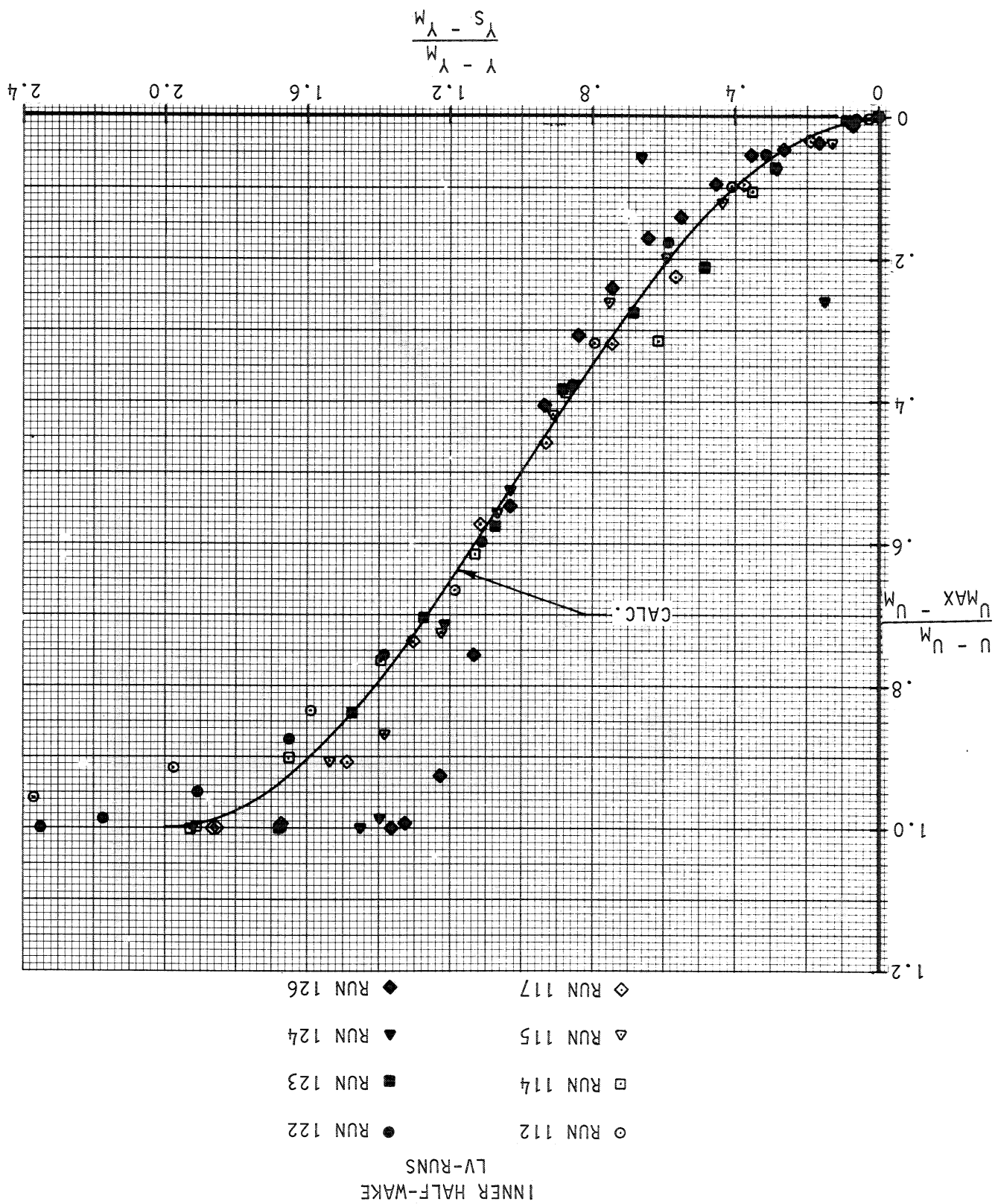


FIGURE 54(a) VELOCITY DISTRIBUTIONS IN THE WAKE, CONFIGURATIONS C-4 AND C-5

FIGURE 54(b) VELOCITY DISTRIBUTIONS IN THE WAKE, CONFIGURATIONS C-4 AND C-5



1. Report No. NASA CR-3655		2. Government Accession No.		3. Recipient's Catalog No.	
4. Title and Subtitle EXPERIMENTAL STUDIES OF THE SEPARATING CONFLUENT BOUNDARY-LAYER. VOLUME I - SUMMARY				5. Report Date June 1983	
				6. Performing Organization Code	
7. Author(s) J. A. Braden, R. R. Whipkey, G. S. Jones and D. E. Lilley				8. Performing Organization Report No. LG82ER0184	
				10. Work Unit No.	
9. Performing Organization Name and Address Lockheed-Georgia Co. 86 South Cobb Drive Marietta, GA 30063				11. Contract or Grant No. NAS1-16028	
				13. Type of Report and Period Covered Contractor Report	
12. Sponsoring Agency Name and Address National Aeronautics and Space Administration Washington, D.C. 20546				14. Sponsoring Agency Code	
15. Supplementary Notes Langley Technical Monitor: H. L. Morgan Final Report					
16. Abstract Test descriptions and results are documented from an experimental low-speed study of the separating confluent boundary-layer on a NASA GAW-1 (General Aviation) high-lift airfoil. The airfoil was tested in a variety of high-lift configurations comprised of leading-edge slat and trailing-edge flap combinations. The primary test instrumentation was a two-dimensional laser-velocimeter (LV) system operating in a "back-scatter" mode. Surface-pressures and corresponding LV-derived boundary-layer profiles are given in terms of velocity components, turbulence intensities and Reynolds shear stresses as characterizing confluent boundary-layer behavior up to and beyond stall. Comparisons are given between LV-derived profiles and associated boundary-layer parameters and those obtained from more conventional instrumentation such as pitot-static traverses, Preston-tube measurements and hot-wire surveys. The complete data set are presented in two separate volumes. The present document presents a descriptive summary of the experimental set-up along with limited test results. Pertinent comparisons of the results are made where possible with those from other sources. NASA Contractor Report 166018 and its supplements contain the bulk of the experimental measurements in tabulated and plotted forms. This work was performed under contract to NASA, Langley (NAS1-16028).					
17. Key Words (Suggested by Author(s)) Boundary-Layers Multi-Element Airfoils Laser-Velocimetry			18. Distribution Statement Unclassified - Unlimited Subject Category 02		
19. Security Classif. (of this report) Unclassified	20. Security Classif. (of this page) Unclassified	21. No. of Pages 164	22. Price A08		